2012

Geometrical and electronic structure of metal oxide nanoparticles on silica and alumina

Udaya Indike Rodrigo
Louisiana State University and Agricultural and Mechanical College

GEOMETRICAL AND ELECTRONIC STRUCTURE OF METAL OXIDE NANOPARTICLES ON SILICA AND ALUMINA

A Dissertation

Submitted to the Graduate Faculty of the
Louisiana State University and
Agricultural and Mechanical College
in partial fulfillment of the
requirements for the degree of
Doctor of Philosophy

in
The Department of Chemistry

by
Udaya Indike Rodrigo
B.S., University of Peradenya, 1999
M. Phil., University of Peradeniya, 2004
M.S., Bowling Green state University, 2006
August 2012

This thesis is dedicated to my late father

ACKNOWLEDGMENTS

I would like to express my sincere gratitude to my advisor, Dr. Erwin Poliakoff, for accepting me as a research student. I am grateful to him for his valuable guidance, advice, and time not only during research but also my entire period of graduate studies at Louisiana State University. Without his advice and close guidance, I would not have completed my graduate studies at LSU. Moreover, I would like to thank the other members of my graduate advisory committee, Dr. Robin L. McCarley, Dr. Les Butler and Dr. Bin Chen for being a part of my graduate committee, and for their valuable assistance and suggestions throughout the research and my entire graduate studies. Also, I would like to express my deepest appreciation to Dr. Amithava Roy, the beamline manager and Gregory Merchan, the beamline scientist at the Center for Advanced Microstructures and Devices (CAMD) for their assistance and guidance during my data collection and analysis.

Over the past six years, I have enjoyed an abundance of professional and social relationships at LSU. I am grateful to, the Department of Chemistry for providing me unrestricted facilities during my entire course of study. If I began to credit those who have assisted me and forget to mention someone's name, it would be an unforgivable and regrettable mistake. Therefore, I would like to express my most sincere and deepest appreciation to everybody in the Chemistry Department for their invaluable support for me to achieve my scientific endeavors.

I am taking this opportunity to thank my colleagues and friends, who shared good and bad moments with me during my research career at LSU. Finally, I owe a special debt of gratitude to my loving parents and wife for believing in me and encouraging me to pursue graduate studies. Without their support and love this entire degree would not have been possible.

TABLE OF CONTENTS

Dedication……. ii

Acknowledgments……... iii

List of Tables..……vii

List of Figures..……. viii

Abstract…….. xii

Chapter 1 - General Introduction…….. 1

1.1 Overall goal of the project…….... 1

1.2 Background…….. 2

1.3 Existing Methods for the Analysis of nanometer size particle...…….. 8

1.4 Structure and Morphology of Particles……. 9

1.5 X-ray absorption spectroscopy……... 12

1.5.1 X-ray Absorption Theory.……. 15

1.5.2 X-ray Absorption Coefficient…….. 17

1.5.3 X-ray Absorption Spectra……..... 18

1.5.4 X-ray Absorption Near Edge Structure……. 19

1.5.5 Extended X-ray Absorption Fine Structure……..... 19

1.5.6 EXAFS Equations…… 22

1.5.7 Advantages and Limitations of X-ray Absorption Spectroscopy……..... 23

1.5.8 X-ray Absorption Measurements…….. 23

1.5.9 Synchrotron Radiation Facilities……... 25

1.5.10 Beamline Setup……... 28

1.5.11 Monochromators and their Calibration……... 29

1.5.12 XAS Scan Parameters……..... 31

1.6 Detectors……... 33

1.6.1 Ionization Detectors……. 33

1.6.2 Fluorescence Detectors…….. 33

1.7 Data processing……..... 35

1.7.1 ATHENA …… 37

1.7.2 ARTEMIS……..... 39

1.8 References ……... 42

Chapter 2 - Experimental Section…… 47
2.1 Materials…… 47
2.2 Dendrimers…… 47
2.3 Preparation of Nanoparticles…… 49
2.3.1 Copper Oxide Nanoparticles…… 49
2.3.2 Bimetallic Nanoclusters…… 51
2.3.3 Metal oxide nanoparticles in the surface mediated reactions… …… 51
2.3.4 Temperature Control Dosing of Nanoparticles…… 52
2.4 Double Crystal Monochromator (DCM) Beamline…… 53
2.5 EXAFS and XANES Measurements…… 55
2.6 Data Reduction and Refinements…… 57
2.7 Electron Microscopic Images and Analysis…… 57
2.8 References…… 59

Chapter 3 - X-ray and TEM Studies of Dendrimerically Generated Copper Oxide Nanoparticles Tethered to Fumed Silica…… 60
3.1 Background…… 60
3.2 Motivations and Goal…… 61
3.3 Experimental Method…… 63
3.4 Results and Discussion…… 64
3.5 Conclusions…… 75
3.6 References…… 76

Chapter 4 - Effect of Substrate on Formation of CuO Particles: How Cu Oxide Forms on Alumina…… 79
4.1 Introduction…… 79
4.2 Background…… 80
4.3 Experimental Method…… 82
4.4 Results and Discussion…… 83
4.5 Conclusions…… 91
4.6 References…… 92

Chapter 5 - Cu/Ni Oxide Bimetallic Nanoparticles…… 95
5.1 Introduction……..... 95
5.2 Why Cu/Ni oxide bimetallic nanoparticles?…… 97
5.3 Sample Preparation…….. 98
5.4 Results and discussion…… 99
5.4.1 EXAFS Data……..…… 99
5.4.2 R Space Data for mixed metal oxide at their respective K-edges…… 102
5.4.3 XANES Data…… 106
5.5 Microscopic Data…… 109
5.6 Summary of findings…….……... 110
5.7 References……. 112

Chapter 6 - X-ray Studies of Copper Oxide Nanoparticles on a Silica Matrix Exposed to Different Types of Dioxin/Furan Precursors…… 114
6.1 Introduction……..…… 114
6.2 Background and Motivation…….. 115
6.3 Experimental Method……..... 118
6.4 Results and Discussion…….. 119
6.5 Conclusion and Future Directions……. 125
6.6 References……..……..….. 126

Chapter 7 - General Conclusions and Outlook……... 127
7.1 Conclusions……... 127
7.2 Outlook……. 132
7.3 References…… 133

Vita…… 134

LIST OF TABLES

Table 2.1 Mixing ratio of Ni^{+2} and Cu^{+2} ions…….…….. 51

Table 2.2 Monochromator Crystals and Acquired energy range……..… 54

Table 3.1 Scattering paths and corresponding distances of the x-ray photoelectron for CuO (cupric oxide) standard……... 70

LIST OF FIGURES

Figure 1.1 Nanoparticle formation/growth and mediation of pollutant-forming reactions in combustion systems…….…….. 3

Figure 1.2 Excitation of core electron from a Bohr model atom …….……..... 13

Figure 1.3 The energy level diagram for K-edge, L-edge and M-edge transitions..... 16

Figure 1.4 The X-ray absorption spectrum of NiO at the Ni K-edge in which the XANES region, EXAFS region, and white line noted in the figure……. 18

Figure 1.5 Nickel K-edge X-ray absorption spectrum of NiO to Illustration of the X-ray absorption process……..... 21

Figure 1.6 National Synchrotron Light Source II (NSLS-II) at the Brookhaven National Laboratory on Long Island, NY……. 25

Figure 1.7 Schematic diagram of a generation three synchrotron radiation facility…….. 26

Figure 1.8 DCM X ray Beamline – layout of optics and experimental stage…… 28

Figure 1.9 Bragg's law; theta is the angle of the incident radiation; d is the interplanar spacing of the crystal ; λ wavelength of the X-ray ……..…….. 30

Figure 1.10 Shows an example of incident (I_0), transmission (I), and fluorescence (I_f) measurement positions…… 31

Figure 1.11 Normal view of the ATHENA main window……... 38

Figure 1.12 ARTEMIS main window with its data view……. 40

Figure 2.1 Structure of DAB (poly(propylene imine) dendrimers …….. 48

Figure 2.2 Schematic diagram of dendrimeric preparation of CuO nanoparticles…… 50

Figure 2.3 Custom-made vacuum exposure system in Dr. Dellinger's lab……... 52

Figure 2.4 Flow diagram of the CAMD experimental floor……. 53

Figure 2.5 Schematic diagram of X-ray double crystal monochromator beamline at CAMD…….. 55

Figure 2.6 Schematic diagram of X-ray absorption spectroscopy set-up at CAMD…… 56

Figure 3.1 Sample preparation for XANES and EXAFS analysis…….. 64

Figure 3.2 XANES spectra for copper oxide nanoparticles prepared at fully doped (2 to 1)and severely underdoped (64 to 1) conditions with both copper oxide (CuO and Cu_2O) standards …….. 65

Figure 3.3 XANES spectra for copper oxide nanoparticles (a) Nanoparticles prepared at fully doped (2:1) to 1/16 doped condition (b) Nanoparticles prepared at severely under doped (64: 1 and 32:1) conditions, with both copper oxide (CuO and Cu_2O) standards …… 66

Figure 3.4 EXAFS spectra for copper oxide nanoparticles prepared at fully doped and severely under doped conditions with copper oxide standards(CuO and Cu_2O)……. 67

Figure 3.5 Radial distribution functions for copper oxide nanoparticles prepared at all the different concentration ratios between NH_2 groups of the dendrimer and Cu^{+2} ions with cupric oxide (CuO) standard…..……... 68

Figure 3.6 Radial distribution functions for copper oxide nanoparticles prepared at both fully doped and severely underdoped conditions with cupric oxide (CuO) standard (Note the differences in the spectra between 2-3 Å and 5-6Å)……..…….. 69

Figure 3.7 TEM images and histograms of nanoparticles prepared at different concentration ratios between NH_2 groups of the dendrimer and Cu^{+2} ions (2 to1 refers to nanoparticles prepared under fully doped conditions)……. 71

Figure 3.8 SEM image of the nanoparticles prepared at severely under doped conditions (64:1)……. 72

Figure 3.9 XANES spectra for the nanoparticles prepared at severely under doped condition (32:1) at different CuO coverage on fumed silica with copper oxide standards…….……..……. 73

Figure 3.10 Microscopic (a and b: High Angle Annular Dark Field TEM and c: High resolution TEM) imagers of nanoparticles prepared at severely under doped condition (32:1) at different CuO coverage on fumed silica (a) 1% (b) 3% (C) 5% ……. 74

Figure 4.1 XANES spectra for copper oxide particles supported on fumed alumina prepared at fully doped (2:1), half doped (4:1), quarter doped (8:1), 1/8 doped (16:1) and severely underdoped (64:1) conditions with both copper oxide (Cu_2O and CuO) standards at Cu K-edge…..……. 84

Figure 4.2 Radial distribution function for EXAFS data for copper oxide particles supported on fumed alumina prepared at fully doped (2:1), half doped (4:1), quarter doped (8:1), 1/8 doped (16:1) and severely underdoped (64:1) conditions with both copper oxide (Cu_2O and CuO) standards …….. 85

Figure 4.3 SEM image of CuO particles supported on fumed alumina prepared at fully doped conditions (molar ratio of NH_2-groups of the dendrimer (DAB-G4) to Cu^{+2} maintained at 2:1)……. 87

Figure 4.4 SEM image of CuO particles supported on fumed alumina prepared at severely under doped conditions (molar ratio of NH_2-groups of the dendrimer (DAB-G4) to Cu^{+2} maintained at 64:1)…….. 88

Figure 4.5 SEM image of CuO particles supported on fumed silica prepared at fully doped conditions (molar ratio of NH_2-groups of the dendrimer (DAB-G4) to Cu^{+2} maintained at 2:1)…….. 89

Figure 4.6 Radial distribution functions of copper oxide particles (prepared at fully doped conditions with the dendrimer) on different support substrate surfaces with CuO standard…….…….. 90

Figure 5.1 Different architectures of bimetallic nanoparticle (a) core shell (b) alloy (c) monometallic mixtures……. 96

Figure 5.2 Schematic diagram of dendrimeric (PAMAM) preparation bimetallic Nanoparticles …….. 98

Figure 5.3 K-space data (spectra) for bimetallic nanoclusters and NiO nanoclusters at Ni K-edge…… 99

Figure 5.4 K-space data for all the bimetallic nanoclusters and CuO nanoclusters at Cu K-edge…… 100

Figure 5.5 K-space data for highest amount of Ni containing bimetallic nanoclusters and CuO nanoclusters at Cu K-edge with CuO standard; Insert: Comparison of K-space data for NiO nanoclusters and NiO Standard …… 101

Figure 5.6 Radial distribution functions (R-space spectra) for bimetallic nanoclusters andCuO nanoclusters at Cu K-edge..……... 102

Figure 5.7 Radial distribution functions for Cu1Ni10 bimetallic nanoclusters at Cu K-edge with CuO and NiO nanoclusters……... 103

Figure 5.8 Radial distribution functions for bimetallic nanoclusters at the Ni K-edge.... 104

Figure 5.9 Suggested core - shell models..…… 105

Figure 5.10 XANES spectra CuO nanoclusters with Copper oxide standards……. 106

Figure 5.11 XANES spectra for bimetallic nanoclusters and CuO nanoclusters with copper oxide standards…….. 107

Figure 5.12 XANES spectra for bimetallic nanoclusters and NiO nanoclusters with nickel oxide standard……. 108

Figure 5.13 (a): High Angle Annular Dark Field TEM image of Cu1Ni1 mixed metal oxide nanoparticles…… 109

Figure 5.13 (b): Energy dispersive spectra (EDS) of Cu1:Ni1 mixed metal oxide sample at the selected nanoparticles (pt1 and pt2)…….. 110

Figure 6.1 Possible mechanisms for the adsorption of 2-chlorophenol and reduction of Cu (II) O on fumed silica support matrix. We were interested in pathway b, two 2-chlorophenols are chemisorbed at vicinal sites and result in formation of Cu (I) by a 1e- transfer reaction at each site…… 117

Figure 6.2 Formation of Chlorophenoxyl radical from the absorption of 2-Chlorophenol on surface hydroxyl of CuO…… 118

Figure 6.3 XANES spectra for the CuO nanoparticles (fully doped) exposed 2-Chlorophenol at different temperatures…… 120

Figure 6.4 XANES spectra for the CuO nanoparticles (fully doped) exposed to different types of dioxin precursors…… 121

Figure 6.5 Different size nanoparticles reacted with identical PCDD/F precursor (2-Chlorophenol) at 250^{o}C……. 122

Figure 6.6 Different size nanoparticles reacted with different PCDD/F precursors at 250^{o}C…….. 123

ABSTRACT

Recent studies demonstrated nanometer-scale combustion-generated nanoparticles cause demonstrable health effects. It is essential to understand the chemical characteristics of these nanoparticles. Since combustion-generated nanoparticles arise in complex mixtures, we employed a dendrimeric method to generate simpler, more reproducible nanoparticles, which were tethered to fumed silica and alumina to provide surrogates for fly ash. We collected XANES and EXAFS data, which are useful for characterizing disordered mixtures where the metal is a minor component.

The effect of particle size on structural properties was studied with copper oxide nanoparticles on fumed silica. XANES data demonstrated copper atoms in the nanoparticles are present in the +2 oxidation state. Spectral features in the near-edge region differ between nanoparticles prepared under fully doped and severely underdoped conditions. Severely underdoped reaction conditions cause agglomeration, consistent with the long-range order seen in the radial distribution functions.

Substrate effects on particle formation were studied by changing the support surface. Studies of CuO on fumed alumina suggested copper species existed with a +2 oxidation state and as CuO sites with an oxocation like structure. Similar studies for the TiO_2 supported CuO confirmed formation of CuO nanoparticles. These observations suggested dendrimeric formation of copper oxide nanoparticles on support surfaces depend highly upon the selected support substrate.

Mixed metal oxide nanoparticles of varied Ni and Cu concentrations were synthesized on fumed silica. X-ray studies found both ions were present with a +2 oxidation state. XANES spectra suggested copper species were slightly electropositive while nickel species were slightly

electronegative. Microscopic studies confirmed the EXAFS observation of small size nanoparticles and the presence of both metals inside one nanocluster mimicking mixed metal oxide nanoclusters.

The contribution of metal oxide nanoparticles in surface mediated reactions was studied by exposing size-selected nanoparticles to model polychlorinated dibenzofurans/dibenzo-p-dioxins (PCDF/PCDD) precursors. X-ray absorption data for the exposed nanoparticles were compared with the unexposed samples to characterize electronic structure and oxidation state during the process. XANES data for the temperature dependent reaction of 2-chlorophenol with CuO nanoparticles prepared at fully doped condition showed incomplete reduction at 375 ^{o}C and good agreement with the previously proposed mechanisms.

Chapter 1
General Introduction

1.1 Overall goal of the project

Artificially created or combustion generated heterogeneous ultrafine particles play an important role in the environment because of their unique properties [1-11]. They can undergo most unpredictable behaviors, hardly anticipated based on our current understanding, and impact the environment and mankind [9,11,12]. Therefore, it is essential to understand the internal structures and chemical characteristics of these nanometer size particles which are likely to cause hazardous environment and health effects [1-11,12]. There have been few systematic studies of their formation, chemical reactivity and composition. The recent discovery of the importance of environmental nanoparticle formation and the contribution to other processes have drawn the attention of many environmental scientists towards this arena [9,13,14]. The goal of my project was to ascertain the structure and oxidation state information for the metals present in oxidized mono and bimetallic nanoparticles; such metal oxide nanoparticles are of interest because they are likely to be present in the emissions from combustion sources.

It is clear from reviewing the relevant literature, the size and the dispersity of the nanoclusters can be manipulated by choosing different generations (sizes) of amine-terminated diaminobutane (DAB) core dendrimers, as well as by adjusting the stoichiometry of the complexed metal ions to the selected dendrimer [15-18, 20]. The results showed a trend of decreasing nano-structure size with increasing dendrimer generation. It is also possible to manipulate the nanocluster size, typically by varying the ratio of the dendrimer to the metal ion. Other studies have shown that metal ions like Cu, Ni, Fe strongly complex with DAB dendrimers [19,20]. Since naturally occurring nanoparticles comprise a complex mixture, a dendrimeric method was used

to generate metal oxide nanoparticles to provide a means of controlling the size distribution of nanoparticles in a systematic manner.

It is well established among the combustion research community that surface mediated reactions are responsible for the formation of toxic air pollutants, such as polychlorinated dibenzo-p-dioxins and polychlorinated dibenzofurans (PCDD/Fs). Combustion related processes and transition metal species present in fly ash play major roles in the formation of PCDD/Fs [13,20,21]. Since adsorption can produce both particle growth and surface-mediated pollutants, it is important to understand how molecules are adsorbed onto the nanometallic surfaces. Here, I have investigated the capability and the contribution of size controlled metal oxide nanoparticles in surface mediated reactions.

For my project nanoparticles were tethered to different substrates like fumed silica, alumina and titania. I have focused on metal oxide nanoclusters based on Cu, Fe and Ni metals. These provide useful surrogates for fly-ash mixtures. Since the prepared nanoparticles were highly disordered, and the metal of interest was typically a minor component in a complex mixture, it was extremely useful to use synchrotron radiation to perform these experiments. X-ray spectroscopies are useful in generating information on noncrystalline, complex systems. X-ray absorption spectroscopic experiments were carried out at the double crystal monochromatic (DCM) X-ray beamline of the Center for Advanced Microstructures and Devices (CAMD) at the respective K edges of the nanoparticles of interest.

1.2 Background

Over the last few decades, studies have been carried out to address the health and environmental effects due to combustion generated airborne fine particles[1-3]. Epidemiological observations in highly urbanized and industrialized cities have consistently found that concentrations of post combustion generated airborne ultrafine particles can cause detrimental

health effects[3]. It has been revealed that most of these demonstrable health impacts are due to fine particles in the nanometer size regime[4-6]. Due to their small size, these combustion generated nanoparticles are transported over longer distances in the atmosphere and able to penetrate deep into the respiratory system, enhancing the potential of hazardous health impacts, such as lung cancer, asthma and so on[7]. These findings have motivated regulatory efforts of international organizations (EPA & WHO) and local authorities of most countries to strive towards a better understanding of the role of these ultrafine particles on human health and the environment [8].

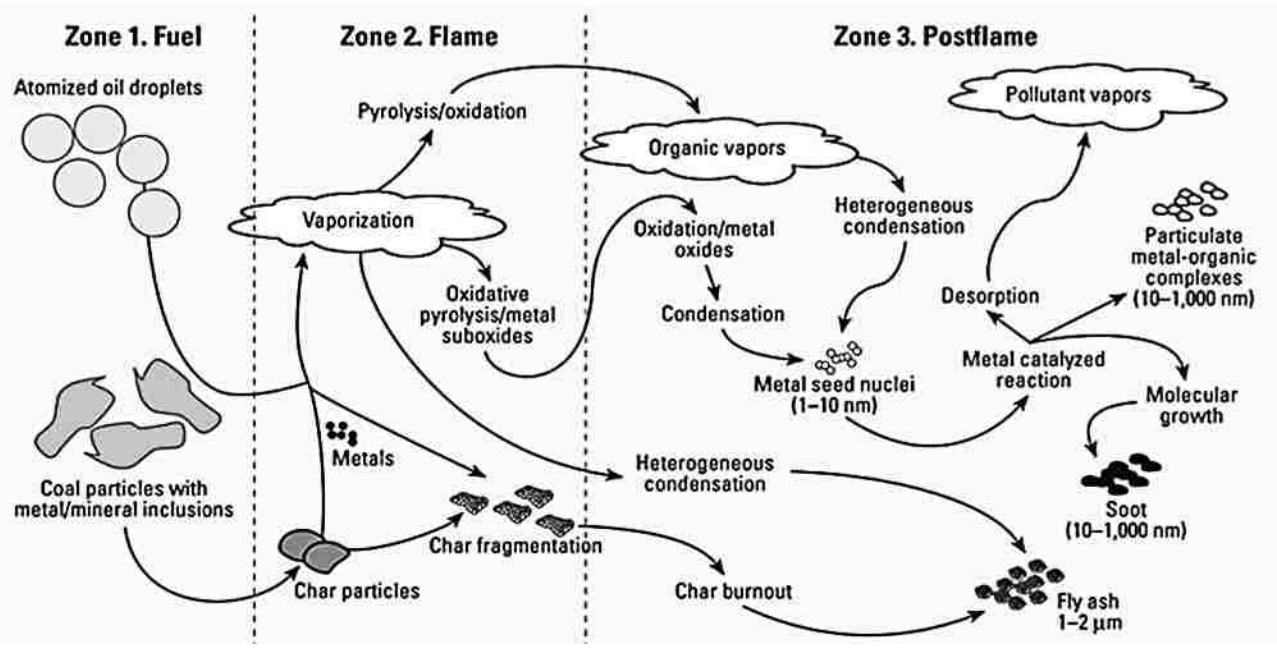

Figure 1.1 Nanoparticle formation/growth and mediation of pollutant-forming reactions in combustion systems [22]

Post combustion generated fine particles (or particulate matter) are a complex mixture of different types and much of these are unlikely to have drastic effects on humans [9, 10]. However, there are a few types of particles which can cause adverse effects on both humans and the environment [9, 10]. Many hypotheses have been introduced to address these drastic effects on humans and the environment, but information on toxicological mechanisms for how these fine particles effect humans (and animals) are very limited.

Complex and detailed analysis of the North American and European epidemiological data indicate there is a wide variability in morbidity and mortality rates associated with exposure to ultrafine particles [1-9]. It has also been found that the period of exposure, number density (concentration) and surface areas of the particles are more important parameters to be considered for health effects than chemical composition [1,9,11].

Airborne fine particles are typically classified by their size and they can be categorized into three major modes [11]:

- Nuclei Mode
- Accumulation Mode
- Coarse Mode

Combustion generated fine particles, which result from high temperature, low vapor pressure processes, rapidly nucleate into fine particles with diameters less than 10 nm. Solid particles, which are formed during chemical reactions and mass growth in flames, can achieve particle growth by coagulation and condensation of vapor. Then these particles enter into accumulation mode. Particles which grow from nuclei tend to accumulate in this size range, but they do not grow really quickly into larger sizes. The growth rate of particles in accumulation mode is controlled by increased particle mass due to the reduction of the surface area and the collision rate. The coarse particle mode is generally raised from wind action on soil, mechanical abrasion or combustion of solid fuels. The composition, as well as the morphology, of the coarse mode particles is considerably different from nuclear or accumulation mode particles.

The physical characteristics of aerosol particles are simply described by their size distribution, but they could even be represented in terms of number, surface area or volume/mass distribution[1, 9, 23]. Most of these fine and ultrafine particles, which have drawn the highest

concern and attention by the public health agencies, are commonly derived from combustion related activities by humans or/and natural sources such as volcanoes and uncontrolled burning (forest fires). Even though vehicular traffic has increased drastically over the last few decades, researchers have found the mass concentration of all the pollutants has decreased significantly with the reduction of coal combustion for power generation and residential heating [11]. On the other hand, scientists have observed a dramatic increase in the number concentration of ultrafine particles (size between 10-30 nm) that are associated with vehicle emission[11].

These fine and ultrafine particles can be named as combustion generated nanoparticles. Nanoparticles are defined as primary particles with at least one dimension < 100nm and ultrafine particles are defined as particles with all dimensions below 100nm. Combustion generated nanoparticles (CGNP's) belong to a very broad group of particles, which merely depend upon their origin in the combustion process and their demonstrated toxicities in various models. These CGNP's are commonly categorized in terms of their physicochemical properties, composition and size, as well as their role in adverse effects on humans or molecular toxicity. Because of these characteristics, CGNP's have received variable and gradual interest in many areas of research over the last few decades [9].

These nanoparticles or ultrafine particles with a diameter less than 100 nanometers have different properties compared to micrometer size particles of the same chemical composition[8]. With a reduction in particle size, properties can change dramatically with respect to hardness, active surface area, electrical conductivity, magnetic characteristics, chemical and biological activity and so on. Such properties may be impressive in the perspectives of material science but may be unwanted from other perspectives because of their possible toxic effects on humans and the environment [9,10].

At present, nanoparticles are manufactured and used in hundreds of commercial products such as sunscreens, cosmetics, clothes, tires, and electronics. Also, there is an increasing tendency to use nanoparticles for medicinal purposes such as imaging and drug delivery [9,10]. Since the manufacturing and use of nanoparticles are becoming increasingly popular, humans are more likely to be exposed to these fine particles via occupation, consumer products or the environment.

Since there is no toxicity data available for most manufactured nanoparticles, it is critical to investigate the toxicity of different nanoparticles [10,11]. Most of the epidemiological, atmospheric, environmental and statistical analyses are really useful in estimating the potential impact on public health; however, these studies do not offer insight into a general mechanism for the effect of fine particles on human health [9,11].

A fundamental understanding of the interaction of particles with living organisms requires the collective contribution of researchers in the fields of toxicology, epidemiology, as well as combustion and aerosol chemistry [24-28]. Here one needs to consider the full life-cycle of fine particles, how they undergo atmospheric transport and transformation, and how they can deposit in lungs and other organs to possibly inhibit biological responses [28]. Motor vehicle engines and stationary combustion systems, such as power generation plants and waste incinerators, are the most significant sources of ultrafine aerosol particles [13,28,29]. Elemental carbon, inorganic sulfates and nitrate compounds are significant components in combustion generated ultrafine particles [28,29]. Samples from urban environments have been found to consist of trace amount of metal ions, and in many cases they tend to be associated with carbon in a single particle [9,11,12].

Combustion generated fly ash, mainly from coal and residual oils, contains a wide variety of toxic metals that are well known to leach out from fly ash and cause health effects to mankind[21]. Solubility of biological media, or bioavailability, of the metals is the primary factor determining the health effects of exposure to fly ash [30, 31].

According to recent literature, a significant fraction of combustion generated fine particles is formed via post combustion condensation of relatively non-volatile particles [9,12,22]. These airborne fine particles are mainly composed of carbon based compounds and minute concentrations (percent to ppm) of transition, alkali, and other toxic metals [12,32]. In terms of health effects, transition metals play an important role [9,11]. Along with the most abundant iron, zinc, copper, nickel, lead, manganese and few other metal ions are potentially present in the aerosol depending upon the source. Primarily, metal ions enter into the combustion system via fuel or lubrication oil, but metal ions can also be generated by wear and tear of the engine components [11,26].

There are several studies that have compared the potential toxicities of transition metals or metal oxide nanoparticles [33-35] with others such as Ag and Al_2O_3 nanoparticles [36]. Jeng et al. compared the cytotoxic effects and mitochondrial dysfunction after exposure to several metal oxide nanoparticles. In this study, ZnO particles were found to be the most potent candidate[35].

Among the discussed mechanisms about the health effects caused by the ambient particles, one of the most intensely covered is the ability of these particles to cause oxidative stress [37, 38]. This mechanism may be very important and needs further attention for the toxicities of the manufactured nanoparticles since there is a link between ambient particles with DNA damage, mutation and cancer [9,33]. Further, there is strong evidence that the particles that have a potential to cause DNA damage can be regarded as more likely to have an effect on cancer

development. However, there are a very limited number of studies which have focused on the investigation and comparison of the effect of different nanoparticles on DNA damage or on oxidative stress. Iron and iron oxide are the most common types of nanoparticles scientists initiate their studies with, but it was found that the particles present in the public transport systems such as subways contain other metal particles such as copper and zinc which have a higher genotoxic potential [39,40].

Recently (2008) Karlsson at al. investigated and compared the ability of different types of nanoparticles and carbon nanotubes to cause DNA damage and oxidative stress as well as cytotoxicity [33]. The study was focused on nanoparticles of different transition metal oxides such as CuO, TiO_2, ZnO, $CuZnFe_2O_4$, Fe_2O_3 and Fe_2O_4, and the toxicities were compared with carbon nanoparticles and multiwall carbon nanotubes. Results indicated there is a huge variation in the ability to cause toxic effects among different nanoparticles. Regarding DNA damage and cytotoxicity, CuO nanoparticles have the highest potential among the above mentioned particles even though all these metal oxide nanoparticles contribute to DNA damage [33].

1.3 Existing Methods for the Analysis of nanometer size particles

As reported in recent literature, several methods have been used for the detection and analysis of nanoparticles on different surfaces. Among those techniques, scanning electron microscopy (SEM) [41,42], atomic force microscopy (AFM) [43] and transmission electron microscopy (TEM) [44] are the commonly used techniques for particle structure and morphology related studies. Incident beam scattering techniques like small angle X-ray scattering (SAXS) [45-47], small angle neutron scattering (SANS) [48,49] and light absorption (extinction) experiments [50] are used to obtain information about particle size distribution, mean particle diameter, number density, volume fraction, pore sizes and surface to volume ratio [45-47]. Mass

spectrometry [51,52] and differential mobility analysis (DMA) [53,54] are the other widely used techniques for characterization and quantitative analysis of nanoparticles. X-ray absorption spectroscopy, TEM and SEM have been extensively used during my study, and these experimental techniques are discussed in detail.

1.4 Structure and Morphology of Particles

SEM and TEM are popular techniques used to study the particle structure and the morphology of the samples [41,43,44,55] particularly at the nanometer regime. SEM uses a focused high-energy electron beam to scan the surface of a solid sample that generates a variety of signals. The signals correspond to the interactions between the sample and the electron beam and can be used to reveal information about the morphology (texture), chemical composition, crystalline structure of the sample, and orientation of the materials contained in the sample. In most applications, data were collected over a selected area of the sample surface, and a two dimensional (2-D) image was generated by using the secondary electrons. Areas of the sample ranged from 1 cm to 5 microns in width. The conventional SEM scanning mode can be used to preform imaging and to determine the topology of the nanoparticle samples. Most modern SEM instruments are equipped with an EDS (Energy-Dispersive X-Ray Spectroscopy) system. Since SEM is capable of performing analyses of selected point locations on the sample, combining the approach of SEM and EDS is especially useful in determining chemical compositions (qualitatively/semi-quantitatively) of the nanoparticle in the respective samples [56,57].

AFM is another surface scanning technique that is capable of preforming surface analysis on particles deposited on an atomically flat substrate. AFM can produce a 3D topological map of the selected sample with angstrom resolution in height and nanometer resolution in the plane parallel to the surface [43]. Transmission electron microscopy (TEM) can be used to investigate the

arrangement of molecules in both the inside and outside of the sample with high image resolution. TEM and STEM are related techniques which use an electron beam directed onto the selected area to produce an image of the ultra-thin sample. The image resolution of the technique is on the order of 1-2 Angstroms (Å).This technique is also capable of additional analytical measurements which require more significant sample preparation [58].

Common applications of both these techniques are in the areas of process development and defect analysis on nanometer scale structures (eg: identification of nanometer size defects on integrated circuits), determination of crystallographic phases as a function of distance from an interface and nanoparticle characterization (eg: core/shell investigations, agglomeration and effects of annealing). Also, this technique can be used as a device to investigate layer thickness, sidewall angle, catalyst support coverage, ultra small area elemental maps and so on.

TEM has three main modes of operation to analyze the structures of fine particles. In the bright field transmission electron microscopy (BFTEM) mode the images are formed by the direct incident or the transmitted electron beams. In the dark field transmission electron microscopy (DFTEM) mode the transmitted beams are excluded and the diffracted beams (from the atomic layers) are used to form the image. In the high resolution transmission electron microscopy (HRTEM) mode, also known as phase contrast microscopy, a combination of both bright and dark field TEMs is used.

The BFTEM images mainly reveal information about the size, shape, such as the aggregate structure of particles, and particle opacity (transparency). DFTEM images are required to obtain information about the internal structure of the particle (eg: soot). These images carry information about the crystallinity of the sample of interest (surrogates for soot), in our case, the internal arrangement of metal oxide nanoparticles in different substrate surfaces. The diffraction

of incident beams increases with the increasing crystallinity of the sample, which in turn increases the brightness of DFTEM images. When performing high resolution transmission electron microscopy (HRTEM) the diffracted beam is combined with the transmitted beam to reconstruct particle structures. These images can show the composition of the particles, how these primary particles link together to form aggregates, and also, can provide information about the shapes of the primary particles and their crystallinity [58,59].

The differential mobility analyzer (DMA) is a one of the widely used instruments to quantify the size distribution of airborne fine particles in the size range of 1–100 nm [53,54,60]. The size distribution is determined by counting these particles using a condensation particle counter [61]. Here, sampled fine particles are diluted and cooled to avoid any further chemical or physical processes taking place. Then the particles are charged and separated using an electrostatic classifier based on their mobility. But the DMC is not a feasible technique to analyze particles embedded onto a substrate surface, as in our case.

Atomic force microscopy (AFM) is one of the other techniques that can used to determine the size distribution of particles by collecting them onto a preferable surface (AFM grid or mica surface) [60]. AFM is also known as scanning force microscopy (SFM) and is a type of scanning probe microscopy with the achievable resolution on the order of fractions of a nanometer. Therefore AFM has become one of the preeminent tools for imaging, measuring, and manipulating matter at the nanoscale level [43,60,62]. Here the information is gathered by "feeling" the surface with a mechanical probe that preforms accurate and precise movements on the surface enabling very precise scanning. The resolution of AFM is mainly depending upon the instrument used during the study. During our study some AFM experiments were performed by

drop coating nanoparticle samples on a silicon wafer; however, we could not find adequate resolution to support our study.

Incident beam scattering experiments using X-ray (SAXS) or neutron beams (SANS) can also be used to obtain information about size distributions of particles present in the combustion flames, including mean particle diameter, number density, volume fraction, pore sizes and surface to volume ratio [45-47]. Resonance enhanced multi-photon ionization (REMPI) followed by time-of-flight mass spectrometry (TOF-MS) is a popular technique to measure the composition and characteristics of nanometer scale particles of soot and soot precursors (nanoparticles) generated in flames [51,52,60].

1.5 X-ray absorption spectroscopy

X-ray absorption spectroscopy (XAS) was the main technique used during this project. XAS has been extensively used to investigate both the bulk and the local structure of a variety of solid-state materials. This technique is particularly useful for studying metal species when the metal of interest is a minor component in a complex sample. The dendrimerically prepared transition metal oxide nanoparticles are highly disordered, and the metal of interest is typically a minor component. Therefore, XAS is a useful technique for the characterization of substrate supported nanoparticle mixtures.

XAS has been applied to various problems in many different areas of science, such as solid state chemistry, soil science, mineralogy, geochemistry and so on. XAS was developed in the 1970s and is commonly used in experiments performed in synchrotron radiation facilities, which are capable of producing intense and tunable X-ray energies [63,64].

As selected by the X-ray energy, the XAS signal comes from all the atoms of a single element regardless of the complexity of that particular sample. High quality XAS spectra can be

collected on homo or heterogeneous mixtures of any physical state: gas, liquid or solid, with little or no pretreatments to the original samples [65,66].

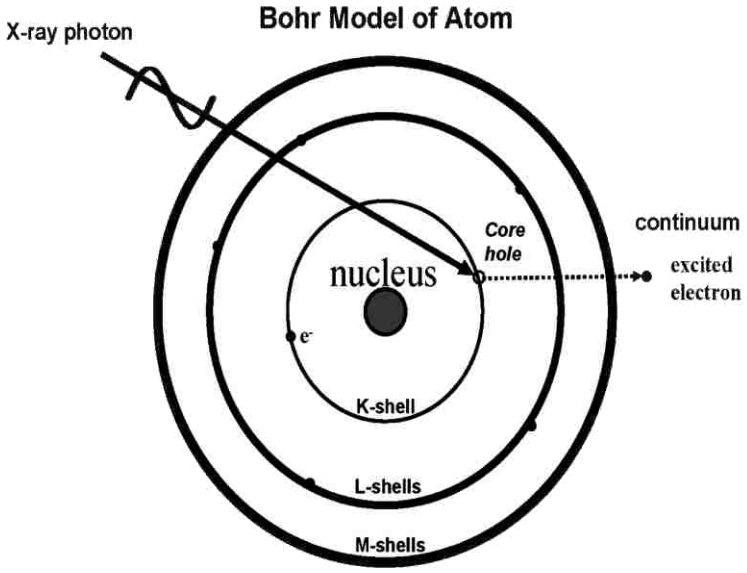

Figure 1.2 Excitation of core electron from a Bohr model atom[65]

This property makes XAS ideally suited for many complex systems and a wide variety of applications. XAS is useful for obtaining structural information, as well as, identifying the chemical speciation of elements, including minerals, noncrystalline solids, adsorbed phases and so on [65].

XAS data are obtained by tuning the photon energy, commonly by using a crystalline monochromator, to an energy range from which core electrons can be excited. Basically, photon energies ranging from 0.1-100 keV can be produced. The "name" of the edge depends upon where the core electron is ejecting from and the edges are named as K-, L-I or L-II and so on. This technique can be improved with the addition of X-ray focusing, which makes it possible to study the differences in the atomic environment of an element within (or between) individual particles and grain boundaries [65,66]. Even though it has its difficulties in experimental application on various other samples (eg: biological samples), L-edge spectroscopy is generally more

sensitive to the structural, electronic, and spin state changes of the metal cluster compared to K-edge spectroscopy [66].

X-ray Absorption spectroscopy considers both X-ray absorption near edge structure (XANES) and extended X-ray absorption fine structure (EXAFS) spectroscopies. It is a measurement of the transitions of an electron from the core electronic states of the metal to the excited electronic states (LUMO) and to the continuum. These two methods (both XANES and EXAFS) give interrelated or complementary structural information. The XANES spectra report electronic structure, valence state and coordination geometry of the metal site, and EXAFS can be used to determine the local molecular structure of a particular element within a sample and to report numbers, types, and distances to ligands and neighboring atoms from the absorbing element.

Application of several different experimental techniques is the best way to reveal the complex nature of a sample, with each individual measurement providing both unique and complementary information. X-ray absorption spectroscopy probes the immediate environment of the selected element, within about 6 Å, and its theoretical interpretation does not rely on any assumption of symmetry or periodicity. Unlike in XAS, X-ray diffraction (XRD) is applicable to more crystalline samples which have long range ordering of atomic planes at approximately 50 Å or more (in length scale) [65,66]. Both XRD and XAS can be used to determine distances between atoms but the information derived from two techniques are from very different X-ray interactions with the sample.

X-ray fluorescence (XRF) is another complementary technique to both XAS and XRD. XRF spectrum can be used to determine the elemental distribution within a sample, since each element fluoresces at a specific (or unique) energy [65]. The results are useful for interpreting

EXAFS and XANES data by identifying the elements that are associated with and/or coordinated to the element of interest. A combination of micro-XRF and micro-XAS has been used in the areas of geochemistry and soil science to characterize geochemical matrices, to study mineral formation and transformation processes in complex matrices as well as the association of minerals with plant roots [65].

1.5.1 X-ray Absorption Theory

X-ray absorption occurs when an electron in a core shell orbital of an atom excites into the higher energy unoccupied orbitals or into the continuum (electron is no longer associated with the atom) by acquiring all the energy from an X-ray. Since the absorbed X-rays belong to a class of particles termed photons, the excited electron is termed as a photoelectron. The excitation of core electrons creates core holes and the relaxation process occurs as an electron transitions from a higher-energy electron orbital to fill the core hole with the release of energy. Electronic transitions due to X-ray absorption are restricted by the dipole selection rule where angular momentum is conserved. This rule states that the electron transitions can occur only between energy states that differ in the azimuthal quantum number (l) by ± 1.

The electron which has been promoted into a higher energy state by absorption of an X-ray photon is very short lived and within a period of femtoseconds (10^{-15} s) the core hole is filled by the transition of an electron from a higher energy orbital. The energy released could be either in the form of fluorescence radiation, Auger electron production or a secondary electron. X-ray fluorescence occurs when an electron from a higher energy orbital fills the core hole by releasing an X-ray.

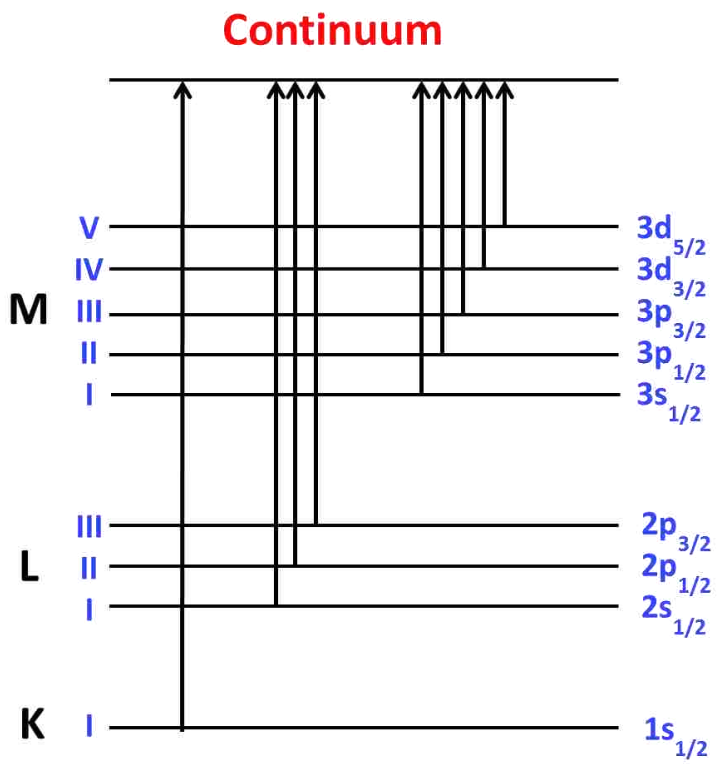

Figure 1.3 The energy level diagram for K-edge, L-edge and M--edge transitions [66]

The energy of the fluorescent X-ray is equal to the difference in the energy of the two orbitals. The emitted fluorescence X-ray energies for a given electronic transition are unique for the particular element because the electron orbital energies are unique to each element. Auger decay occurs when an electron from a higher-energy orbital fills a core hole, losing its energy by the emission of another electron from the same or a different atomic shell. Secondary electron, or photon production, is the other common relaxation process which occurs with X-ray absorption. These processes result from multiple steps of electrons cascading downward in energy as corresponding core holes are filled and from one of these multistep processes emitting an electron or photon.

1.5.2 X-ray Absorption Coefficient

The number of X-rays transmitted through a sample (I_t) is given by the intensity of X-rays impinging on the sample (I_0) decreased exponentially by the thickness of the sample (x) and the absorption coefficient of the sample (μ)

$$I_t = I_0 e^{-\mu x} \quad \ldots\ldots\ldots\ldots \quad \textbf{(a)}$$

The absorption of X-rays by a material can be designated as the percentage decrease in the incident X-ray intensity (I_0) or the energy-dependent absorption length of the material (exponential factor, μx). This effect is exponential and an increase in the thickness of the sample by one absorption length decreases the transmitted X-ray intensity by ~63% [100%× $(1 - e^{-1})$]. The X-ray absorption coefficient (μ) is the probability for an X-ray to be absorbed by a sample, and it is considered as a property of all elements within the sample. X-ray absorption spectroscopy involves measuring the absorption coefficient as a function of X-ray energy.

In a typical experimental setup for XAS, X-rays go through an ionization chamber to measure the number of incident X-rays (I_0) then through the sample, and next through another ionization chamber to measure the number of transmitted X-rays (I_t). The X-ray absorption coefficient is determined by rearranging equation (a) above.

$$\mu = [1/x] \ln (I_0 / I_t) \quad \ldots\ldots\ldots \textbf{(b)}$$

Since core-hole production and the subsequent relaxation processes are proportional to absorption, the absorption coefficient can be derived from the number of fluorescence as in equation (c).

$$\mu x \propto (I_f / I_0) \quad \ldots\ldots\ldots \quad \textbf{(c)}$$

The absorption coefficient (**μ**) is a function of the incident X-ray energy. The probability for absorption increases sharply at the position where the incident X-ray energy equals the energy required to excite an electron to an unoccupied electron orbital. This step in the absorption is termed as an absorption edge. Each element has its own specific set of absorption edges according with the corresponding binding energies of its electrons.

1.5.3 X-ray Absorption Spectra

To record a full scale X-ray absorption spectrum, typically data was collected from 200 eV below the edge to approximately 1000 eV above the absorption edge of the metal (element) of interest depending upon the composition of the sample. A typical X-ray absorption spectrum is shown in Figure 1.4.

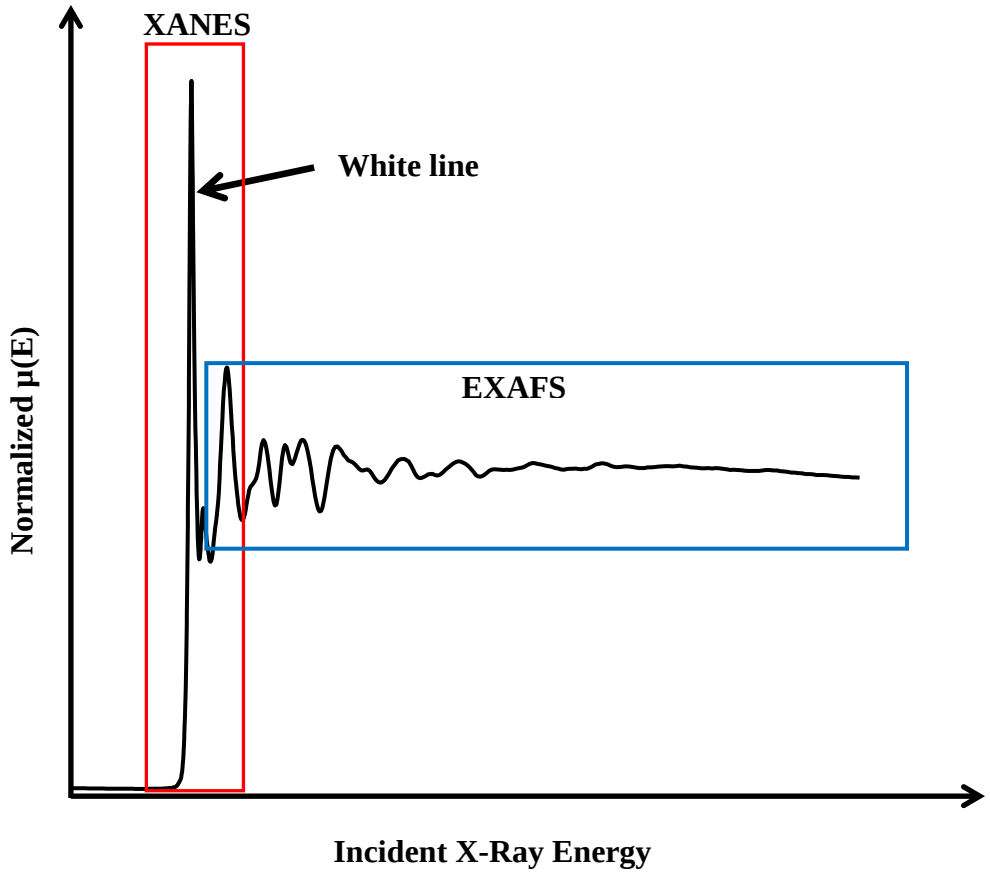

Figure 1.4 The X-ray absorption spectrum of NiO at the Ni K-edge in which the XANES region, EXAFS region, and white line noted in the figure.

1.5.4 X-ray Absorption Near Edge Structure

The X-ray absorption near edge structure (XANES) is the part of the absorption spectrum near the absorption edge, ranging approximately from −50 to +100 eV relative to the edge energy. XANES spectra provide detailed information about the oxidation state and coordination environment (or binding geometry) of the element of interest. The shape of the absorption edge corresponds to the density of states available for photoelectron excitation. In general, K-edge absorption edge energy increases with increasing oxidation state and the rising edge position shifts when changing the effective number of positive charges (or the oxidation state) resulting from 1*s* core-hole shielding effects [67]. If a metal has a higher oxidation state, overall, the positive charge of the atom is high and relatively higher X-ray energy is required to excite an electron from a core orbital. However, if the metal has more negative charge, the XANES spectrum shifts to a lower energy.

The contribution to the K-edge XANES spectrum mainly comes from quantum mechanically allowed (transition with $\Delta l = 1$) and typically intense $1s \rightarrow (n)p$ transitions, where $(n)p$ is the lowest unoccupied *p* orbital of the absorbing atom. However, transition metals with partially occupied *d* orbitals, can generate a pre-edge feature that result from *1s* to $(n-1)\,d$ transitions. These transitions are formally forbidden or dipole-forbidden ($\Delta l = 2$) and are relatively weak in intensity. These pre-edge peaks appear at energies slightly less than that of the main absorption edge. But the intensity of these pre-edge peaks can increase when the ligand environment is perturbed from octahedral symmetry [65].

1.5.5 Extended X-ray Absorption Fine Structure

The extended X-ray absorption fine structure (EXAFS) part of the spectrum is the normalized oscillatory part of the absorption coefficient up to approximately 1000 eV above the absorption edge (Fig.5A). The EXAFS spectral region is used to determine the local

environments of elements in experimental samples. The spectrum contains information on the numbers and types of atoms in coordination with absorber atoms and their interatomic distances. It can also give us some idea about the degree of local disorder. The absorption of an X-ray provides sufficient energy to the absorbing atom to promote an electron (ionize) to a higher electronic energy level. Any excess energy provided to the ejecting electron is carried off as translational kinetic energy, and it is alternatively reflected as the wavelength associated with the photoelectron. The kinetic energy of the photoelectron is given by the following relation:

$$KE = h\upsilon - E_0 \text{ ----------[d]}$$

Where (KE) is the kinetic energy of the photoelectron, ($h\upsilon$) is the incident X-ray energy and (E_0) is the electron binding energy of the photoelectron.

During X-ray absorption process, these X-ray generated photoelectrons can be approximated as spherical waves propagating from the absorber atoms, and then the photoelectron waves are scattered from the atoms surrounding the absorber. The probability for X-ray absorption by the absorber atom is affected by the relative phase of the outgoing photoelectron wave and the incoming scattered wave from the neighboring atoms. The relative phase of the photoelectron is determined by the photoelectron wavelength and the interatomic distances between the absorber and scattering atoms.

The modulation of the absorption coefficient due to backscattered waves from neighboring atoms is the basis of EXAFS. When the outgoing and incoming waves are out of phase (destructive interference), absorption occurs at a minimum, and there is a resultant drop in the absorption coefficient at the oscillatory part (Figure 1.5 b). When the incident X-ray energy is above the edge the KE of the photoelectron increases accordingly and the photoelectron wavelength becomes shorter. Since the average distance between the absorber and the

neighboring atoms remains unchanged, the waves will progressively become in phase (constructive interference), resulting in a maximum in the oscillatory part of the absorption coefficient (Figure1.5 c).

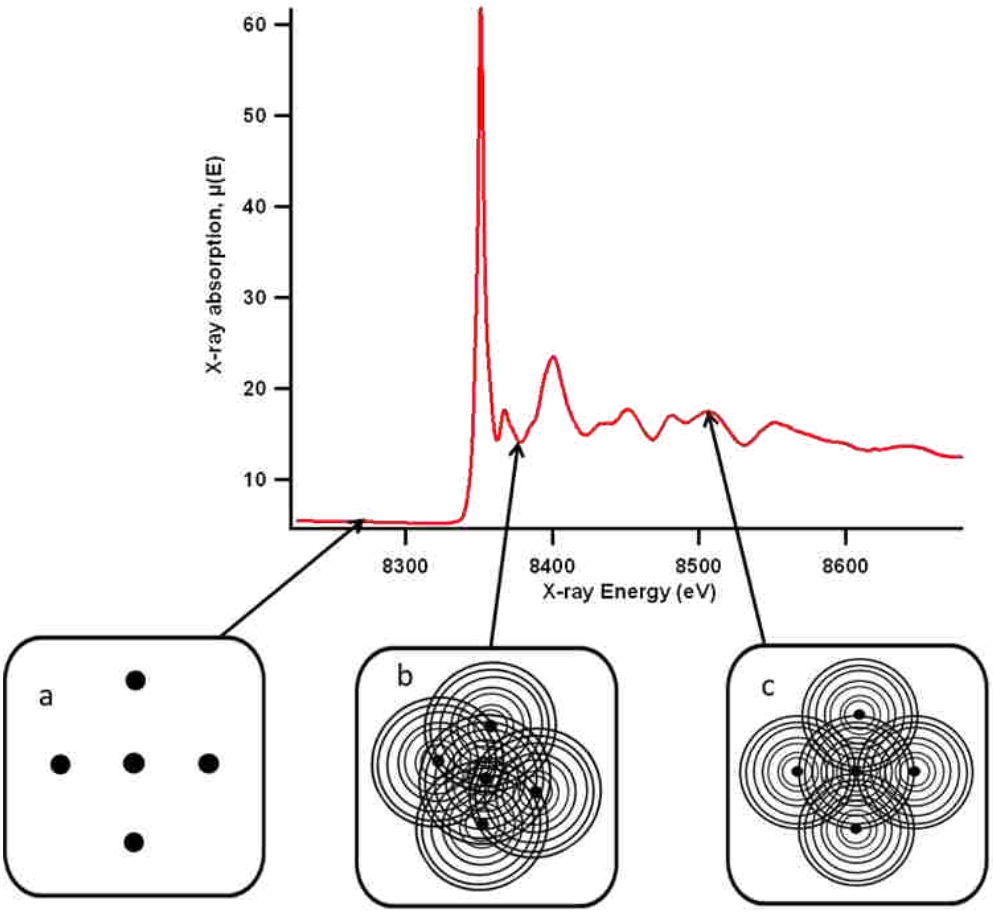

Figure 1.5 Nickel K-edge X-ray absorption spectrum of NiO to illustration of the X-ray absorption process [65]

All photoelectron scattering configurations, which start at the absorber atom, go to one or more neighboring atoms and then return to the absorber atom, contribute to the EXAFS signal. During the EXAFS experiments, the incident X-ray energy is incrementally increased over a wide range of energies and as a consequence the relative photoelectron wavelength progressively decreases over the energy range. These configurations are called scattering paths. The contribution from atoms that are at the same radial distance from the absorber contribute to the

same component of the EXAFS signal, and those atoms are known as a shell (single-scattering paths are from one shell of atoms). The degeneracy of a single-scattering path is known as the coordination number of that shell.

1.5.6 EXAFS Equations [65,66,68]

$$\chi(k) = \sum_i \chi_i(k)$$

$$\chi_i(k) \equiv \frac{\left(N_i S_0^2\right) F_{\mathrm{eff}_i}(k)}{kR_i^2} \sin\left[2kR_i + \varphi_i(k)\right] e^{-2\sigma_i^2 k^2} e^{\frac{-2R_i}{\lambda(k)}}$$

$$R_i = R_{0i} + \Delta R_i$$

$$k^2 = \frac{2m_e\left(E - E_0 + \Delta E_0\right)}{\hbar}$$

Where

$F_{effi}(k)$ = Effective scattering amplitude of the photoelectron

$\varphi_i(k)$ = Phase shift of the photoelectron

$\lambda(k)$ = Mean free path of the photoelectron

σ_i = Root-mean-square deviation

R_i = Half path length of the photoelectron

R_{0i} = Half path length used in the theoretical calculation

ΔR_i = *Half* path length variables

k = Excess kinetic energy of the photoelectron in wavenumber

m_e = Mass of the electron

$\hbar$ = Plank's constant

The EXAFS equation can be used to understand the EXAFS spectrum and the equation can be written as sum of the contribution from all scattering paths of the photoelectron [65,68]. Fourier transform (FT) of the EXAFS data provides information about the distance vector(s)

between the absorbing atom and atoms which it is bounded to, typically within a range of 4 to 5 Å.

1.5.7 Advantages and Limitations of X-ray Absorption Spectroscopy

According to the Eisenberger and Brown, the advantages and limitations of the XAS method can be summarized as follows [66,69].

Advantages

1. XAS is an element specific technique; it can be used to focus on one element without interference from other elements present in the samples of interest.
2. Unlike in EPR or optical spectroscopic methods, the metal of interest is never 'silent or inactive' with X-ray absorption spectroscopy.
3. This technique is not limited by the state of the sample since X-ray absorption spectroscopy (XAS) is sensitive only to the local metal environment.
4. XAS experiments can be performed on biological samples since XAS requires a lower X-ray dose, and damages to biological samples can be precisely monitored and controlled during the experiment.

Limitations

1. A synchrotron X-ray source is required to perform XAS experiments.
2. EXAFS is unable to distinguish between scattering atoms with little difference in atomic number (Eg: C, N, O or S, Cl, or Mn, Fe).
3. It is possible to obtain equally good fits using backscattering atoms which are very different in Z (e.g., Mn or Cl).
4. There are limitations in the resolving distances between 0.1 and 0.2 Å at the presence of the K-edge of another metal.
5. There are difficulties in determining coordination numbers or number of backscatters that are filled with a specified element.

1.5.8 X-ray Absorption Measurements

The general approach of an X-ray absorption experiment usually begins with an element(s) with a particular local atomic configuration that is affecting the macroscopic behavior of the system. Key factors to be considered in a XAS experiment are the identification of the absorber atom(s), their concentration, the absorption edge, the data collection method,

and the data analysis method. There are two different approaches for X-ray absorption analysis. The first method is based on comparing unknown spectra with well-characterized, physical standards. Another method involves comparing or modeling the spectrum for an unknown sample with theoretically calculated spectra. Common practice is to combine both of the above mentioned techniques for EXAFS analysis. On the other hand XANES analysis heavily relies on comparisons with standards. For EXAFS analyses, spectra of physical standards are generally used to compare and to, optimize the theoretical models

Often samples for XAS come from many different projects that involve either single or multiple elements. Analyzing two or more elements is particularly useful when suspected elements are coordinated to each other. For example, consider a project that involves two metal ions in the synthesis of bimetallic nanoclusters.

The concentration of the absorber atom can control the data collection ability of the XAS experiment, and sometimes the concentration can limit data to the XANES part of the absorption spectrum. EXAFS experiments require approximately 100 to 1000 times greater concentration of the absorber element than for XANES. Hence, the feasibility of an X-ray absorption experiment is determined by the number of absorber atoms per unit volume. For an example, if the concentration of an element present in a particular sample is < 0.01 mol%, the K-edge measurement of that particular element becomes more difficult and it requires long measurement times to obtain the required statistics [65,66]. However, X-ray absorption spectra can be collected at more than one edge of one particular element. Edges at low X-ray energies are typically separated by several hundred electron volts (eV) or less, but hard X-ray energy edges are well separated by at least 1000 eV or more, which is essential for EXAFS spectroscopy. Standards for XAS projects usually include well-characterized minerals, adsorbed phases, or

aqueous species that contain the element of interest in chemical forms that are considered relevant to the system of interest. The ideal XAS standards should exactly match all aspects of the chemical species in the sample. However, it is impossible to synthesize or purchase standards that match all aspects of the experimental samples like minerals or noncrystalline solids. Therefore, it is reasonable to use a chemically meaningful standard or theoretical model of an existing standard to mimic the unknown sample.

1.5.9 Synchrotron Radiation Facilities

Figure 1.6 National Synchrotron Light Source II (NSLS-II) at the Brookhaven National Laboratory on Long Island, NY [70]

Synchrotron radiation facilities are the major requirement to perform X-ray absorption spectroscopy since this technique needs a tunable X-ray source. As of today, there are approximately 70 synchrotron radiation facilities in operation around the world[71]. Synchrotron X-ray facilities are classified in terms of generations (currently first to third) based on the capabilities of the range technologies that result from a particular facility. In the United States,

there are about eighteen different second- or third-generation synchrotron user facilities, including DOE-funded third-generation facilities at Argonne National Laboratory (APS), Brookhaven National Laboratory (NSLS) and Berkeley Laboratory (ALS) [71]. Also, there are a few second generation facilities like the Center for Advanced Microstructures and Devices (CAMD at LSU) that are owned and governed by universities with the support of outside users.

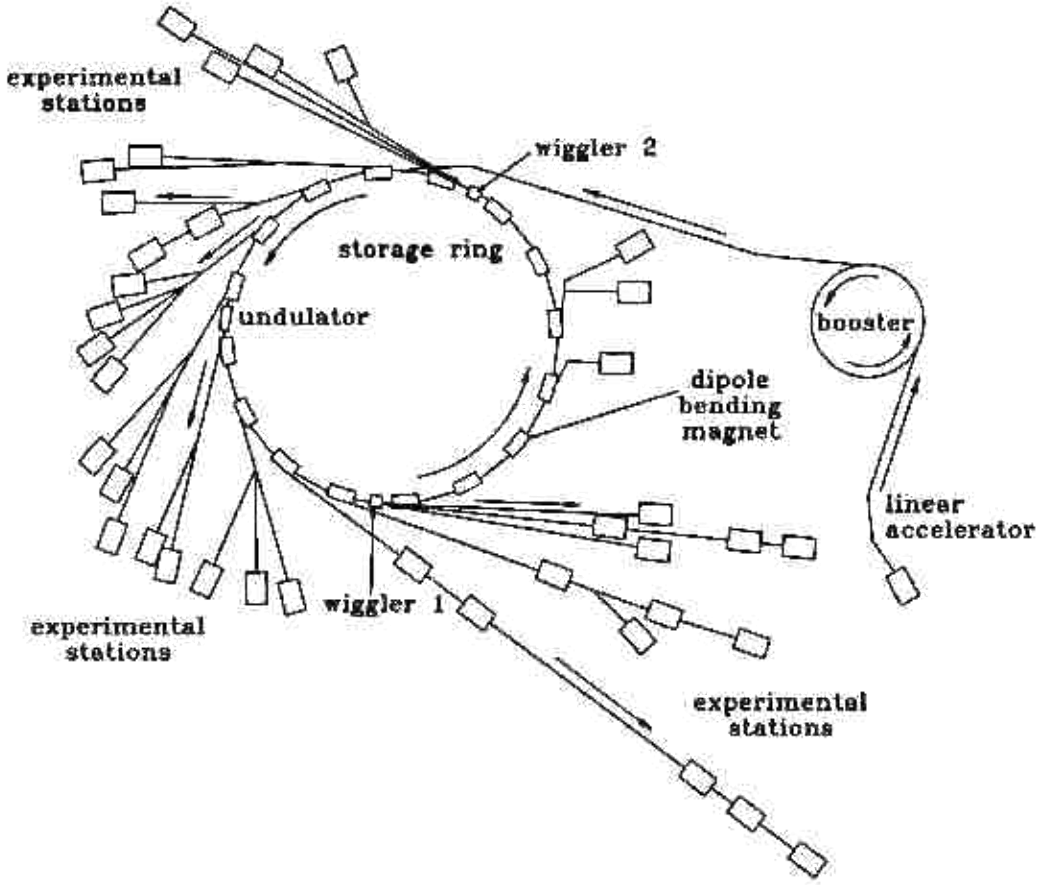

Figure 1.7 Schematic diagram of a generation three synchrotron radiation facility [72]

A schematic diagram of beamlines at a third generation synchrotron facility (ALS) is depicted in Figure 1.7 above. These higher generation synchrotrons generally consist of three major components, a linear accelerator (LINAC), a booster ring and a storage ring. Initially, bunches of charged particles (typically electrons) are accelerated in a linear accelerator (LINAC), after achieving certain velocity they are transferred to a booster ring for further

acceleration and then the particles, which are traveling near the speed of light, are injected into a storage ring. A synchrotron storage ring is an N-sided polygon, where N is the number of bends in which the particles circulate, producing synchrotron radiation, but without gaining further energy.

The particles within the storage ring are accelerated toward the center of the ring, and radiation is projected at a tangent to the electron storage ring. This generates radiation with a broad spectrum of energies (white light). The trajectory of this particle inside the storage ring is bent by magnets, typically known as bending magnets. Wigglers and undulators (integral part of third-generation facilities) are two types of specialized insertion devices widely used at synchrotron radiation facilities that are placed in the straight sections of the storage ring to produce forward directed, quasi-monochromatic, high brilliance synchrotron radiation. Typically, insertion devices consist of arrays of magnets which are used to generate a spatially periodic magnetic field at the electron beam path. These devices are not essential components of the storage ring for its operation, and their only function is to improve generated synchrotron radiation.

Wigglers consist of a series of closely spaced bending magnets that increase the intensity of the X-ray pulse. The strength and the period of the magnetic field in a wiggler are not tuned to the frequency of radiation produced by the electrons. Therefore, every electron in the electron bunch radiates independently to produce a broad radiation spectrum. The radiation intensity of a wiggler scales with the number of magnetic poles in the wiggler.

Undulators consist of a carefully spaced periodic structure of dipole magnets, and this result in a static magnetic field which is alternating along the length of the undulator. Electrons or charged particles which travel through this periodic magnet structure are forced to undergo

oscillations and, thus, radiate energy. In XAS, interference between dipoles affects the emitted X-ray spectrum and this interference is additive at particular wavelengths. Intense X-ray beams at a particular wavelength can be generated by varying the gap between the poles of the magnets.

1.5.10 Beamline Setup

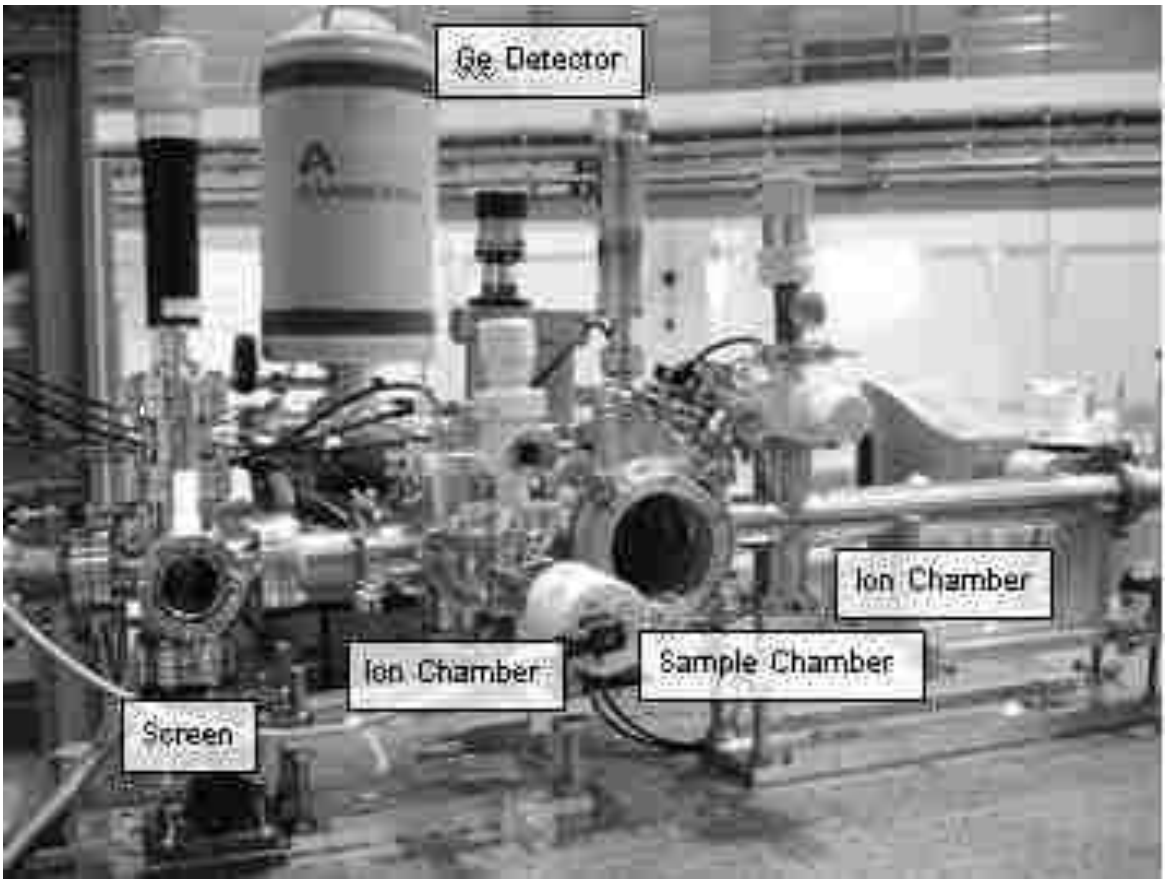

Figure 1.8 DCM X ray Beamline – layout of optics and experimental stage [73]

Beamlines at synchrotron radiation facilities are placed tangential to the storage ring to use the radiation emitted by the bent charged particles (electrons). Bending-magnet and wiggler beamlines are more suitable for XAS measurements because the span of X-ray energies required by the XAS experiment is typically around 1000 eV.

Typical XAS beamlines contain a number of slits (to define the X-ray profile), a monochromator (to choose the X-ray energy), a harmonic rejection mirror (to reduce the harmonic content of the X-ray beam), a sample positioning stage, a few ionization chambers and a detector (to measure the X-ray intensity).

The absorption of X-rays by air can be a significant factor for measurements made at the X-ray energies below 10 keV. Generally, to minimize the loss of X-ray intensity, flight paths (or He-filled enclosures) are placed in the beam path. Often X-ray beamlines are divided into several enclosures to accommodate the ability of the user to access the sample while keeping a constant heat load on the monochromator from the X-ray beam. The monochromator is often contained in the first optical enclosure and the sample and detectors as the second enclosure. Mirrors, slits, and flight paths are usually found in both enclosures.

1.5.11 Monochromators and their Calibration

The monochromators are used in X-ray beamlines to select the incident X-ray energy on the sample. Typically, the monochromator is stepped through the XAS scanning range or it can be run continuously (known as quick-scanning of the monochromator). These X-ray monochromators usually consist of either a single crystal with a slot cut in it (channel-cut monochromator) or two parallel crystals (double-crystal monochromator).

Typical monochromator crystals are made of germanium or silicon. They are cut along a specific crystal plane which is parallel to the surface of the crystal (crystal planes are generally described by the (hkl) indices) and the surface is polished to generate optics for monochromators. Si(111), Si(311), and Ge(111) are the most common types of crystals used as monochromators for X- ray beamlines. The X-ray energies by the crystals are controlled by rotating the crystals in the white beam and only the energies that satisfy the Bragg's Law

requirements are diffracted by the crystal. The energy of the X-ray is determined by the angle of the incident X-ray beam relative to the monochromator crystal through Bragg's Law. The angle of the crystal and crystal position has to be changed depending upon the element of interest. Typically, the monochromator energy is calibrated at a particular edge of the corresponding element at the beginning of the data collection and monitored throughout the experiment.

Bragg's Law is: $\boldsymbol{n\lambda = 2d \sin(\theta)}$

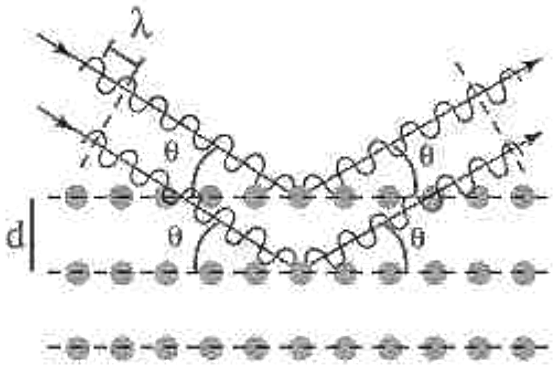

Figure 1.9 Bragg's law; theta is the angle of the incident radiation; **d** is the interplanar spacing of the crystal ; **λ** wavelength of the X-ray [74]

Where

d = Spacing between atomic planes of the crystal parallel to its surface
θ = Angle of the crystal with respect to the impinging white beam,
λ = Wavelength of the diffracted X-ray
n = Integer
(Note: n = 1 corresponds to the fundamental X-ray energy and n > 1correspond to X-rays of higher harmonic energies)

Monochromator angles are controlled by mechanical step motors, and they can slip occasionally causing the X-ray energy to be miscalibrated. Also, crystal spacing can be affected by the temperature of the monochromator [65]. Therefore, the energy of the X-rays is determined from the absorption edge of a reference standard. These reference standards are usually collected in transmission mode (by letting X-rays pass through the sample). However, it is a good practice to monitor the monochromator X-ray energy by simultaneously collecting the absorption spectrum of a reference standard after each XAS scan of the samples. The

comparison of edge energy shifts of XANES spectra can be determined accurately by aligning the reference spectra collected with each sample spectrum. Relative changes in the absorption edge energy occur from different chemical species.

After the other beamline optics are positioned, alignment of the beam with chambers and slits is done by using a fixed-position laser and/or light-sensitive "burn" paper placed across a detector window. Also it is a very good practice to recheck the alignment of the detector(s).

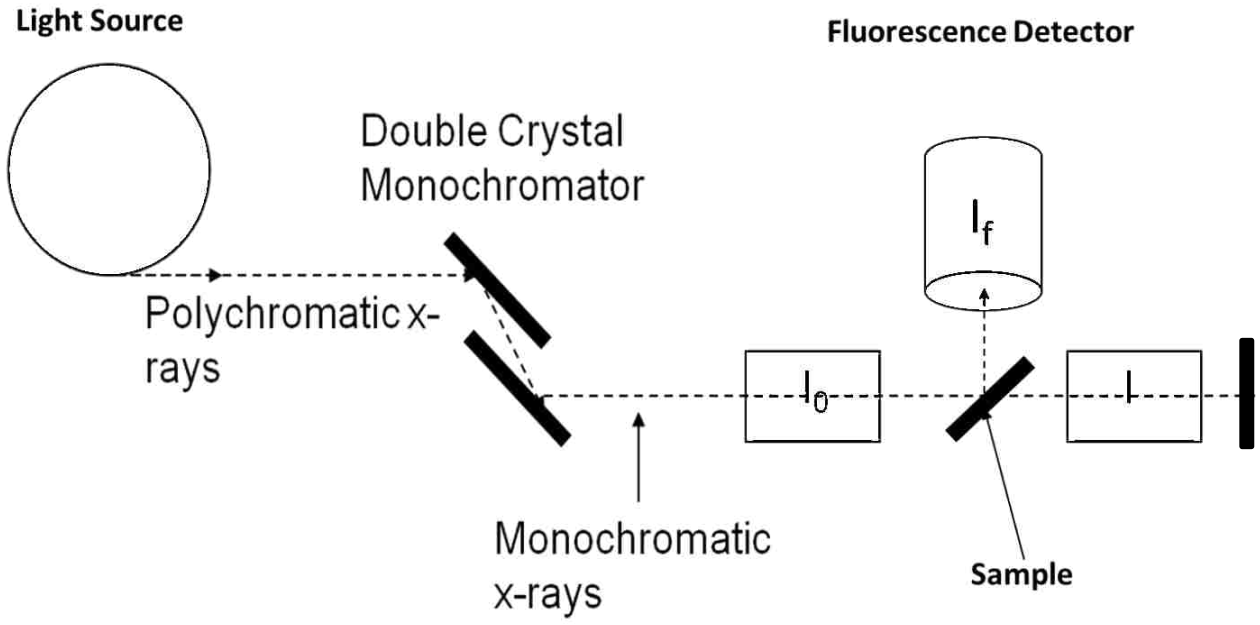

Figure 1.10 Shows an example of incident (I_0), transmission (I), and fluorescence (I_f) measurement positions

1.5.12 XAS Scan Parameters

The energy range, energy step size, or counting time and monochromator settling time are the important scanning parameters that have to be considered during x-ray absorption spectroscopic experiments. The selection of the energy range is done according to the element of interest and at which edge (K or L) the experiment will be conducted. The energy step size determines the narrowest feature which can be probed within a scan, and its lower limit is given

by the energy resolution of the monochromator. The integration time is the duration of the detector signal measured at each energy point. The monochromator settling time is the wait time after each monochromator movement during individual data points (usually 0.2–0.5 s before collecting the next detector signal). The duration of an XAS scan depends upon the type of experiment (XANES or EXAFS) and beam time allocation. Scan duration can also increase with decreasing step size and increasing integration or settling time. The data collection efficiency can be increased by dividing the spectrum into regions that have different energy resolution requirements or regions on which one needs more information. However, commonly divided spectral regions in XAS are (i) the pre-edge region, (ii) the edge region, and (iii) the post-edge region. Large steps of 5 to 10 eV are taken in pre-edge or baseline region while smaller step (0.05 - 0.5 eV) are used to resolve the rapidly changing features in the edge region [65].

Since oscillations broaden with increasing energy at the EXAFS part of the spectrum, smaller step sizes are needed to resolve EXAFS oscillations at lower energies than at higher energies. Because most EXAFS spectra contain information from atoms 5 to 10 Å away from the absorber atom, a typical data point spacing of 0.05 $Å^{-1}$ is more than adequate. Data point spacing of 0.05 $Å^{-1}$ is sufficient to detect signals from atoms about 31 Å away from the absorbing atom [57]. With longer times used to measure the weaker EXAFS oscillations at high k values, detector counting times at each step typically vary from 2 to 4s. Rather than collecting fewer, long (>1 h) scans, it is a good practice to collect multiple scans on one sample (using parameters that yield collection times between 25 - 45 minutes and averaging the data). It is generally recommended to use the same data-collection parameters for all the samples and

standards within a set at a given absorption edge, but the number of scans collected depends on the signal from each sample.

1.6 Detectors

1.6.1 Ionization Detectors

Ionization detectors are gas-filled devices typically used to measure incident X-ray ($\boldsymbol{I_0}$) or transmission ($\boldsymbol{I_t}$), or as a third chamber. Ionization detectors contain two parallel plates separated by a gas-filled space. A voltage bias is applied to the parallel plates separated by the gas. When X-rays travel through the plates some of the gas particles are ionized and create a current across the plates. Here, the applied voltage should give a linear detector response for a given change in the incident X-ray intensity. The ionization detectors are filled with one or two inert gases, like He, N_2, Ar or Kr, to optimize the X-ray absorption at a given edge energy. Absorption increases with increasing detector length and atomic number of the gas. In general, suitable attenuation for $\boldsymbol{I_0}$ detector is 10% - 20% of the X-ray intensity and 70% - 90% for the $\boldsymbol{I_t}$ and $\boldsymbol{I_{ref}}$ detectors. Typically, the ionization detectors are purged with the appropriate gas mixtures, and measurements are made either with the gas mixture is sealed within an air tight detector or while the gas is slowly flowed through the detector (at a rate of 50 –100 mL min^{-1}). The software program Hephaestus contains a calculator for determining the optimum gas mixture, and also, it contains a utility for calculating the number of X-rays per second for required calculation during data analysis.

1.6.2 Fluorescence Detectors

Fluorescence X-rays are typically measured at a 90° angle relative to the incident beam direction, and samples are placed in between at a 45° angle (Figure 1.10). The greatest signal to background ratio is obtained at a 90° angle between the incident beam and the detector, because

this geometry minimizes the scattered radiation. Stern-Heald-Lytle detectors [75], solid-state detectors, like germanium multi-element (Canberra) detector arrays, and Si-drift (Vortex 4-element or single-element) detectors are the most commonly used Fluorescence detectors in X-ray beamlines.

The Stern-Heald-Lytle detectors are basically comprised of solar slits, an X-ray filter, a sample chamber and an ionization detector with a large-window. All these components are connected for automatic alignment of the solar slits. Proper alignment of the solar slits is critical for Stern–Heald detectors and these detectors are useful for samples with low to moderate absorber concentrations in the sample matrix (should have low background signal). The fluorescence ionization chamber in the Stern–Heald detector does not discriminate X-rays on the basis of their energy. The fluorescence X-ray filter is used to preferentially absorb scattered X-rays from the sample, and the filter for the transition metals usually consists of the element of one atomic number lower than the absorber element (called as "Z – 1 filter"). The reason for this is to keep the absorption edge of the filter to an energy between the energies of the incident X-rays and the fluorescence X-rays.

In solid-state detectors, a semiconducting material is used as a sensor for fluorescence X-rays. Although germanium detectors are the most common solid-state X-ray detectors due to their high sensitivity, silicon drift detectors are becoming increasingly popular among users because of their lower cost. The solid-state germanium detectors are operated at liquid nitrogen temperature, and usually the sensor on the detector surface is protected from the external environment by a thin beryllium window. Multi-element detectors have multiple detectors within the sensing unit; it could be 13 to 30 elements on the detector probe. The fluorescence signal from the sample is collected by each element in the detector during each scan. The signal

can be varied between elements because the area of the X-ray transparent window for each element has a different solid angle relative to the position of the incident beam on the sample.

The electronics associated with the solid-state detector allow only X-rays within a specified energy range to be recorded. A major drawback of the multi-element detector is that the electronics on the detector elements can get overloaded by too much signal, creating "dead time" where the detector is spending time processing signal rather than collecting signal. It is recommended to keep the count rate as high as possible and the dead time very low (maximum acceptable dead time is usually 10%) [65]. Common approaches to minimize the dead time of a multi-element detector are to reduce the incident X-ray intensity or increase the distance between the sample and detector.

Electron yield detectors are another type of detector used in XAS. They are commonly used for data collection at the soft X-ray region and are particularly useful on concentrated standards, where Auger electron production is greater than fluorescence. Electron-yield detection is a surface sensitive technique, and it shouldn't suffer from self-absorption effects, which is a common problem associated with data collection in fluorescence mode. Also, this technique can be used to simultaneously collect electron-yield spectra with fluorescence spectra, which in turn helps to compare surface and bulk structures, respectively.

1.7 Data processing

X-ray absorption spectroscopy (XAS) is a technique with broad applicability to many scientific disciplines. Therefore, beamline users as well as researchers and practitioners require a software package that has a broad range of capabilities to achieve their analytical, programmatic and social goals. Among many program packages that were developed to address these goals, B. Ravel and M. Newville have developed a multi-platform, open-source XAS data

analysis software package [76] that provide a rich graphical interface with extensive analytical and numerical capabilities. This set of programs is popular as IFEFFIT library [77] and consist of four major programs namely ATHENA, ARTEMIS, HEPHAESTUS and ATOMS.

The main features of these four programs are [76-78]

1. ATHENA - XAS data processing
2. ARTEMIS - Analysis of EXAFS data (using theoretical standards computed by FEFF program)
3. HEPHAESTUS - Collection of beamline utilities based on tables of atomic absorption data
4. ATOMS - Provide crystallographic functionality for the X-ray absorption spectroscopy. Its primary function is to generate input files for FEFF, the popular XAFS theory code, from crystallographic data.

All the above programs are written in the Perl programming language and their user interface is written by using the Perl/Tk graphical toolkit [76,79]. The PGPLOT (Pearson, 1997) package is used for plotting data. The Perl/Tk toolkit provides a full featured forms-based environment for data interaction and processing [79]. ATHENA and ARTEMIS programs are interfaced and have complete access to all the features of IFEFFIT. Both these programs are quite easy programs to begin the XAS data analysis with and one can quickly become familiar with the many features these programs offer. They also provide sophisticated capabilities for the users, allowing them to access all the information contained in their measured data. HEPHAESTUS and ATHENA compliment most of the data-acquisition software found at XAS beamlines [76,78]. The program HEPHAESTUS provides utilities which are useful for pre-planning and executing XAS experiments. Since ATHENA can read almost any raw data format, it provides a flexible powerful tool for data-processing right at the beamline. All these programs can run on all major computer platforms and are available under the free software

license. Because software is free of charge, a high-quality XAS analysis program is available to most scientists and students all over the world.

1.7.1 ATHENA

ATHENA is an interactive graphical tool for processing X-ray absorption data and can handle most of the common data handling tasks at the beamline or for preparing data for analysis [76,78]. Athena can be used for all the main steps in data processing which includes multiple steps of conversion of raw data to μ (E) spectra such as background subtraction, Fourier transforming and plotting. This program is designed with a highly usable interface to provide high quality data analysis. The normal view of the ATHENA window is shown in Figure 1.11 below.

Main features of Athena program [76,78];

- Convert raw data to μ(E)
- File import plugins for reading arbitrary data files
- Simultaneously process and plot multiple data files
- Merge data in different space (energy, k-, R-, or back-transform k-space)
- Deglitch μ(E) data
- Background removal (using AUTOBK algorithm)
- Normalization of XANES data (to Cromer-Liberman / CLnorm calculations)
- Fourier transforms K- space data (both forward and backward)
- Fit linear combinations of standards to XANES or EXAFS data
- Fit peak functions to XANES data
- Energy calibration
- Align data scans with/without a reference channel
- Self-absorption corrections (for fluorescence spectra)
- Compute difference spectra
- Log-ratio/phase-difference analysis
- Save data as μ(E), normalized μ(E), χ(k), χ(R), or back-transformed χ (k)
- Save project files (allowing people to return to their analysis later)

A powerful feature of ATHENA is displaying many data sets simultaneously for a single data set while processing. In the above figure, buttons labeled with the letters E, k, R, and q are

for plotting single sets of data in energy, k-space, R-space (back-transformed k-space), respectively. The next (lower) row of buttons is to plot multiple sets of data. In this manner, it

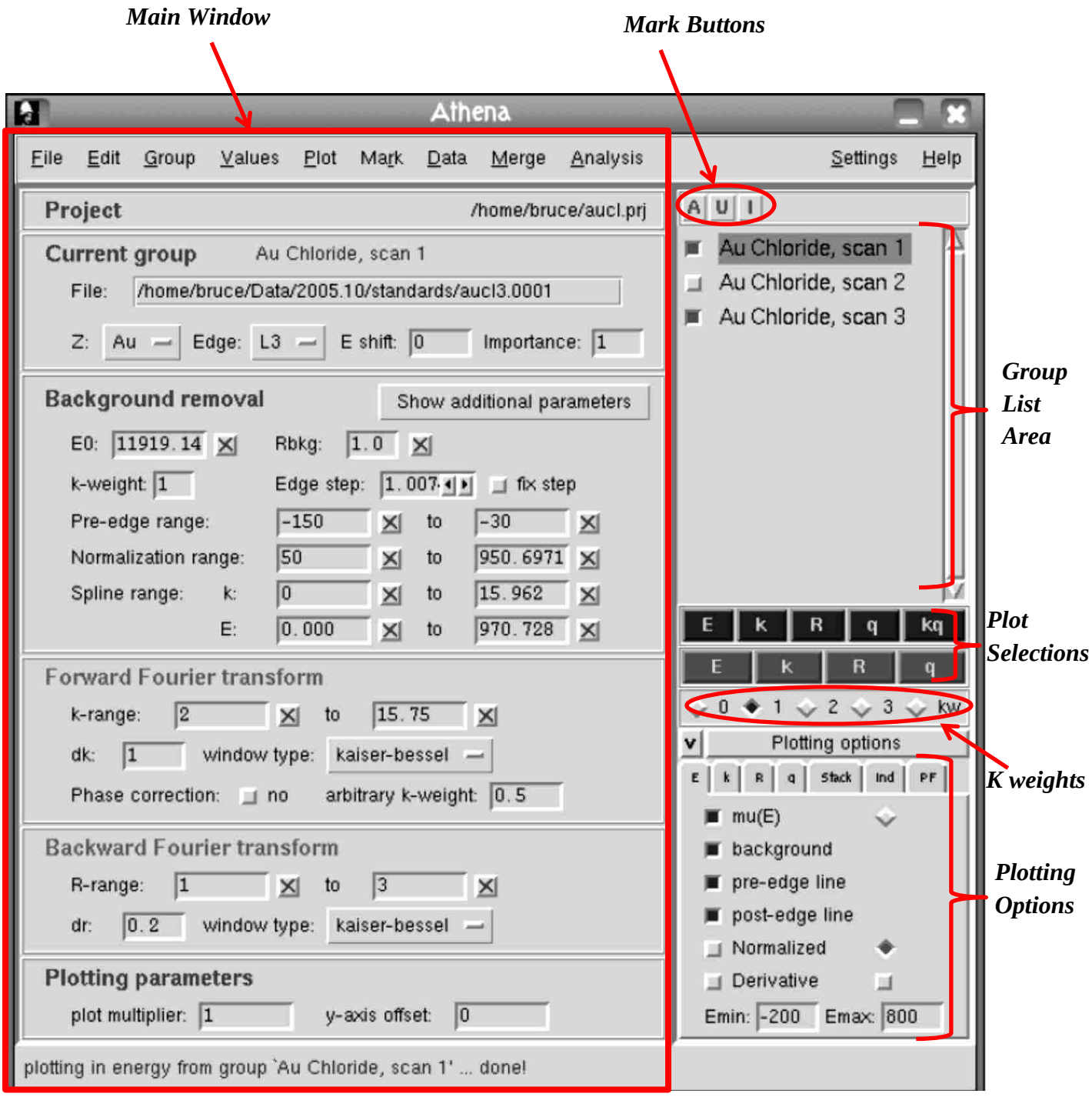

Figure 1.11 Normal view of the ATHENA main window [76,78]

makes it easier to select any subset of imported data for plotting and comparison. Also, the program keeps track of all changes made to the parameters of any set of data and can automatically perform the background removal and Fourier transforms as needed. Parameters for background removal and Fourier transforms can be adjusted individually or constrained in a flexible manner for each data set as required. ATHENA comes with extensive documentation accessible within the program and apart from the above mentioned main features, principle component analysis, self-absorption corrections for fluorescence data and dead-time corrections for data measured with solid-state detectors are the additional features included in ATHENA (they were taken into consideration while planning and implementing the program).

1.7.2 ARTEMIS

ARTEMIS can be described as a graphical and interactive program which works within the framework of multiple-scattering path expansion calculated by FEFF [78-81]. FEFF is an automated program for *ab initio* multiple scattering calculations of XAFS, XANES and several other spectra for clusters of atoms [76-78]. ARTEMIS can help to organize all aspects of a fitting project that includes running the FEFF calculation, parameterizing the paths from the FEFF calculation, setting the parameters for the Fourier transform and fitting of the data, running the fit with selected paths and plotting the overall results with/without the contributing paths [78]. ARTEMIS uses $\chi(k)$ data files as its input and does not handle any data processing tasks such as converting raw data to $\mu(E)$ or background removal. (ATHENA is the sister program of ARTEMIS and does the data processing during any analysis). ARTEMIS includes interfaces to ATOMS and FEFF programs, where ATOMS generates input files, feff.inp, for crystalline materials, and FEFF can yield scattering amplitudes and phases used in many modern XAFS analysis codes [76,78].

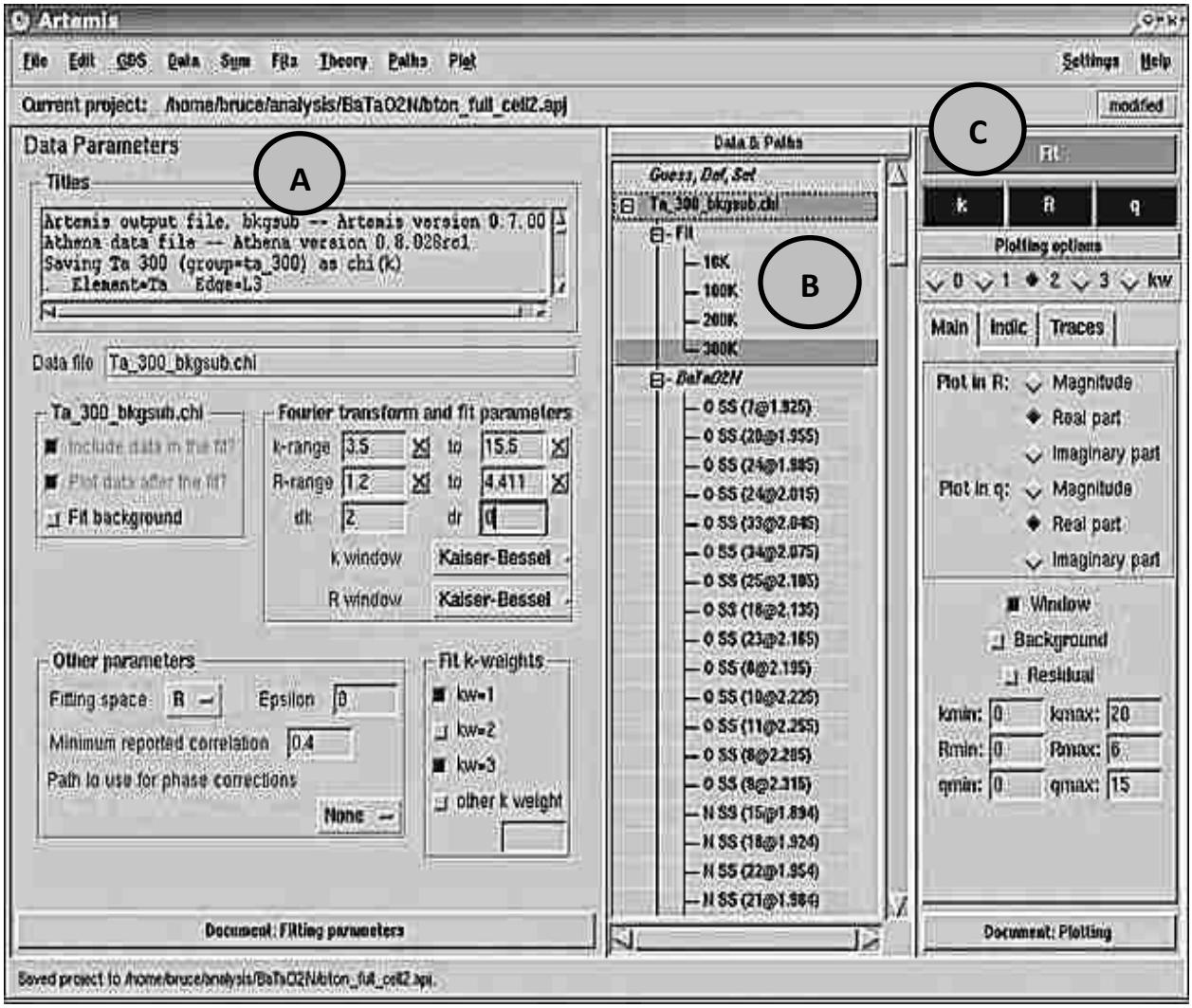

Figure 1.12 ARTEMIS main window with its data view [76,78]

The main ARTEMIS window includes three main sections. Left most section (A) consists of all the data processing parameters, including the range of the Fourier transform from k-space and the fitting range in R-space. The far right panel (C) is used to control how plots are displayed. The middle panel (B) display list of all imported data of interest, FEFF calculations and paths used in the fit. ARTEMIS includes access to the ATOMS [78,80] program, which converts crystallographic data into a suitable format for FEFF. This interface can read crystallographic data either in the form of an ATOMS input file (INP) [78,80]or crystallographic

information file (CIF) [82] and convert them into a FEFF input file. For materials that are not crystalline or do not have a crystalline analogue, one has to prepare FEFF input files in some other way and directly import the files into ARTEMIS. The FEFF interface included in ARTEMIS program is simple and quite adequate for the needs of most EXAFS data analysis. After the FEFF run, ARTEMIS displays a page containing the interpretation of the selected paths computed by FEFF that includes path distances, degeneracy, and atomic species in the path. Also, information is provided on whether the selected path is a single- or multiple-scattering path, and an estimate of the importance of the path. ARTEMIS has capable tools for organizing and plotting the results including the individual contributions of each path in both k- and R-space.

ARTEMIS provides convenient plotting of data in k-, R- or back-transformed k-space, the fit and the number of selected individual paths used in the fit [76,78]. A number of tools are included within ARTEMIS to check the consistency and sensibility of the parameters used in the fit and to evaluate the results of the fit. After a completion of a fit, ARTEMIS displays a log file that includes a statistical analysis of the fit. The parametric terms of the EXAFS equation are evaluated for each path used in the fit. This information along with an easy graphical display of the paths can be used to evaluate the importance of each path to the fitting result. ARTEMIS is certainly well suited to simple first-shell analysis of a single data set and a very powerful tool applicable to the most challenging fitting models [76,78].

1.8 References

(1) Sgro, L. A.; Basile, G.; Barone, A. C.; D'Anna, A.; Minutolo, P.; Borghese, A.; D'Alessio, A. *Chemosphere* **2003**, *51*, 1079.

(2) D'Alessio, A.; Barone, A. C.; Cau, R.; D'Anna, A.; Minutolo, P. *Proceedings of the Combustion Institute* **2005**, *30*, 2595.

(3) D'Anna, A.; Rolando, A.; Allouis, C.; Minutolo, P.; D'Alessio, A. *Proceedings of the Combustion Institute* **2005,** *30*, 1449.

(4) Agudo, A.; Ahrens, W.; Benhamou, E.; Benhamou, S.; Boffetta, P.; Darby, S. C.; Forastiere, F.; Fortes, C.; Gaborieau, V.; Gonzalez, C. A.; Jockel, K. H.; Kreuzer, M.; Merletti, F.; Pohlabeln, H.; Richiardi, L.; Whitley, E.; Wichmann, H. E.; Zambon, P.; Simonato, L. *Int J Cancer* **2000**, *88*, 820.

(5) Wichmann, H. E.; Peters, A., *Philos T Roy Soc A* **2000**, *358*, 2751.

(6) MacNee, W.; Li, X. Y.; Gilmour, P.; Donaldson, K. *Inhal Toxicol* **2000**, *12*, 233.

(7) Dockery, D. W.; Pope, C. A., *Annu Rev Publ Health* **1994**, *15*, 107.

(8) Ibald-Mulli, A.; Wichmann, H.E.; Kreyling, W.; Peters, A., *J Aerosol Med* **2002**, *15*,189.

(9) Donaldson, K.; Tran, L.; Jimenez, L.A.; Duffin, R; Newby, D.E.; Mills, N.; MacNee, W.; Stone, V., *Part Fibre Toxicol*. **2005**, 2,10 .

(10) Avakian, M. D.; Dellinger ,B.; Fiedler, H.; Gullet, B.; Koshland, C.; Marklund, S.; Oberdorster, G.; Safe, S.; Sarofim, A.; Smith, K.R.; Schwartz, D.; Suk, W.A. *Environmental Health Perspectives* **2002**, *110*,1155-1162.

(11) Kennedy, I.M. *Proceedings of the Combustion Institute* **2007,** *31*, 2757.

(12) Oanh, N. T. K.; Reutergardh, L. B.; Dung, N. T. *Environmental Science & Technolgy* **1999**, *33*, 2703

(13) Costa, D.L.; Dreher, K.L. *Environmental Health Perspectives* **1997**, *105*,1053.

(14) Biswas, P.; Wu, C. Y., *Journal of the Air & Waste Management Association* **2005** *55*, 708.

(15) D'Anna, A., *Proceedings of the Combustion Institute* **2009**, *32*, 593.

(16) Larsen, G.; Lotero, E.; Marquez, M., *Journal of Physical Chemistry B*, **2000**, *104*, 4840.

(17) Mitran, E.; Dellinger, B.; McCarley, R. L., *Chem. Mater.* **2010**, *22*, 6555.

(18) Larsen, G.; Noriega, S., *Applied Catalysis a-General* **2004**, *278*, 73.

(19) Velarde-Ortiz, R.; Larsen, G., *Chemistry of Materials* **2002**, *14*, 858.

(20) Floriano, P. N.; Noble, C. O.; Schoonmaker, J. M.; Poliakoff, E. D.; McCarley, R. L., *Journal of the American Chemical Society* **2001**, *123*, 10545.

(21) Alves, D.; Santos, C. G.; Paixao, M. W.; Soares, L. C.; de Souza, D.; Rodrigues, O. E. D.; Braga, A. L., *Tetrahedron Letters* **2009**, *50*, 6635.

(22) Cormier, S.A.; Lomnicki, S.; Backes, W.; Dellinger, B.; *Environmental Health Perspectives* **2006**, *114*,810.

(23) Zhang, J.J.; Morawska, L. *Chemosphere* **2002**, *49*,1059.

(24) Oberdorster, G.; Oberdorster, E.; Oberdorster, J. *Environmental Health Perspectives* **2005**, *113*, 823.

(25) Nel, A.; Xia, T.; Madler, L. ; Li, N. , *Science* **2006**, *311*,622.

(26) Karlsson, H. L.; Cronholm, P.; Gustafsson, J.; Moller, L. *Chemical Research in Toxicology* **2008**, *21*, 1726.

(27) Borm, P. J.; Robbins, D.; Haubold, S.; Kuhlbusch, T.; Fissan, H.; Donaldson, K.; Schins, R.; Stone, V. *Part Fibre Toxicol* **2006**, *3*,11.

(28) Kittelson, D.B. *Journal of Aerosol Science* **1998**, *29*, 575.

(29) Bein, K.J.; Zhao, Y.; Pekney, N.J.; Davidson, C.I.; Johnston, M.V.; Wexler, A.S. *Atmos Environ* **2006**, *40*, S424.

(30) Smith, K.R.; Veranth, J.M.; Lighty, J.S.;. Aust, A.E. *Chemical Research in Toxicology* **1998**, *11*, 1494

(31) Ball, B. R.; Smith, K. R.; Veranth, J. M.; Aust ,A. E, *Inhal Toxicol* **2000**,*12*, 209.

(32) Donaldson, K.; Li, X. Y.; MacNee, W., *Journal of Aerosol Science* **1998**, *29*, 553.

(33) Karlsson, H. L.; Cronholm, P.; Gustafsson, J.; Möller, L. *Chemical Research in Toxicology*, **2008**, *21*, 1726.

(34) Cheng, M. D. *J Environ Sci Heal A* **2004**, *39*, 2691.

(35) Jeng, H. A.; Swanson, J. *J Environ Sci Heal A* **2006**, *41*, 2699.

(36) Park, S.; Lee, Y. K.; Jung, M.; Kim, K. H.; Chung, N.; Ahn, E.-K.; Lim, Y.; Lee, K.-H., *Inhal Toxicol* **2007**, *19*, 59

(37) Donaldson, K.; Stone, V.; Seaton, A.; MacNee, W. *Environmental Health Perspectives* **2001**, *109*, 523.

(38) Li, N.; Hao, M.; Phalen, R. F.; Hinds, W. C.; Nel, A. E., *Clinical Immunology* **2003**, *109*, 250.

(39) Karlsson, H. L.; Nilsson, L.; Möller, L., *Chemical Research in Toxicology* **2004**, *18*, 19.

(40) Karlsson, H. L.; Ljungman, A. G.; Lindbom, J.; Möller, L. *Toxicol Lett* **2006**, *165*, 203.

(41) Muhlfeld, C.; Rothen-Rutishauser, B.; Vanhecke, D.; Blank, F.; Gehr, P.; Ochs, M., *Part Fibre Toxicol* **2007**, *4*, 11.

(42) Che, S.; Lund, K.; Tatsumi, T.; Iijima, S.; Joo, S. H.; Ryoo, R.; Terasaki, O. *Angewandte Chemie International Edition* **2003**, *42*, 2182.

(43) West, P.; Starostina, N. *Adv Mater Process* **2004**, *162*, 35.

(44) Buhr, E.; Senftleben, N.; Klein, T.; Bergmann, D.; Gnieser, D.; Frase, C. G.; Bosse, H. *Meas Sci Technol* **2009**, *20*.

(45) Que, R. H.; Shao, M. W.; Chen, T.; Xu, H. Y.; Wang, S. D.; Lee, S. T. *J Appl Phys* **2011**, *110*.

(46) Tsao, C. S.; Chen, C. Y. *Physica B-Condensed Matter* **2004**, *353*, 217.

(47) Hessler, J. P.; Seifert, S.; Winans, R. E.; Fletcher, T. H. *Faraday Discussions* **2002**, *119*, 395.

(48) Johnson, J. A.; Saboungi, M.-L.; Thiyagarajan, P.; Csencsits, R.; Meisel, D. *The Journal of Physical Chemistry B* **1998**, *103*, 59.

(49) Wang, H.; Zhao, B.; Wyslouzil, B.; Streletzky, K. *Proceedings of the Combustion Institute* **2002**, *29*, 2749.

(50) D'Alessio, A.; D'Anna, A.; D'Orsi, A.; Minutolo, P.; Barbella, R.; Ciajolo, A. *Symposium (International) on Combustion* **1992**, *24*, 973.

(51) Ochiai, N.; Ieda, T.; Sasamoto, K.; Fushimi, A.; Hasegawa, S.; Tanabe, K.; Kobayashi, S. *Journal of Chromatography A* **2007**, 1150, 13.

(52) Bouby, M.; Geckeis, H.; Geyer, F. *Analytical and Bioanalytical Chemistry* **2008**, 392, 1447.

(53) Sgro, L. A.; De Filippo, A.; Lanzuolo, G.; D'Alessio, A. *Proceedings of the Combustion Institute* **2007**, 31, 631.

(54) D'Alessio, A.; Barone, A. C.; Cau, R.; D'Anna, A.; Minutolo, P. *Proceedings of the Combustion Institute* **2005**, 30, 2595.

(55) Muhlfeld, C.; Rothen-Rutishauser, B.; Vanhecke, D.; Blank, F.; Gehr, P.; Ochs, M. *Part Fibre Toxicol* **2007**, 4, 11.

(56) Wilkinson, K.; Lundkvist, J.; Seisenbaeva, G.; Kessler, V. *Environmental Pollution* **2011**, 159, 311.

(57) Groundwater, H.; Twardowski, M. S.; Dierssen, H. M.; Sciandra, A.; Freeman, S. A. *Journal of Atmospheric and Oceanic Technology* **2011**, *29*, 433.

(58) Pérez-Arantegui, J.; Mulvey, T. In *Encyclopedia of Analytical Science (Second Edition)*; Editors-in-Chief: Paul, W., Alan, T., Colin, P., Eds.; Elsevier: Oxford, 2005, p 114.

(59) Vander Wal, R. L.; Yezerets, A.; Currier, N. W.; Kim, D. H.; Wang, C. M. *Carbon* **2007**, 45, 70.

(60) D'Anna, A. *Proceedings of the Combustion Institute* **2009**, 32, 593.

(61) Abid, A. D.; Heinz, N.; Tolmachoff, E. D.; Phares, D. J.; Campbell, C. S.; Wang, H. *Combust Flame* **2008**, 154, 775.

(62) Barone, A. C.; D'Alessio, A.; D'Anna, A. *Combust Flame* **2003**, 132, 181.

(63) Sayers, D. E.; Stern, E. A.; Lytle, F. W. *Phys Rev Lett* **1971**, *27*, 1204.

(64) Eisenberger, P.; Kincaid, B. M. *Science* **1978**, *200*, 1441.

(65) Kelly, S. D.; Hesterberg, D.; Ravel, B. In Methods of soil analysis, Part 5: Mineralogical methods; Ulery, A. L.; Drees, L. R., Eds.; Soil Science Society of America: Madison, WI, 2008, p 367− 463.

(66) University of California, Davis, XAS: Application. http://chemwiki.ucdavis.edu/@api/deki/pages/1918/pdf (accessed April 16,2012)

(67) Shulman, R. G.; Yafet, Y.; Eisenberger, P.; Blumberg, W. E. *P Natl Acad Sci USA* **1976**, *73*, 1384.

(68) Stern, E. A. *Contemp Phys* **1978**, *19*, 289.

(69) Eisenberger, P.; Brown, G. S. *Solid State Commun* **1979**, *29*, 481.

(70) National Synchrotron Light Source II (NSLS-II), Brookhaven National Laboratory, Long Island, NY. http://www.bnl.gov/nsls2/2010BeamlineProposals.asp (accessed April 17,2012)

(71) Light Source Facility Information. http://www.lightsources.org /cms/?pid=1000098& printable=1(accessed April 17,2012)

(72) Hessenbruch, A.; A short history of x-rays: sources and detectors. http://authors.library.caltech.edu/5456/1/hrst.mit.edu/hrs/materials/public/Xrays/sources_detectors.htm (accessed April 17,2012)

(73) Synchrotron Light Research Institute. Photographs of XAS station http://www.slri.or.th/en/index.php?option=com_content&view=article&id=44&Itemid=93 (accessed April 17,2012)

(74) McSwiggen & Associate. Principles of X-ray Diffraction http://www.mcswiggen.com/FAQs/FAQ_graphics/X-ray_Diffraction.gif (accessed April 17,2012)

(75) Stern, E. A.; Heald, S. M. *Review of Scientific Instruments* **1979**, *50*, 1579.

(76) Ravel, B.; Newville, M. *Journal of Synchrotron Radiation* **2005**, *12*, 537.

(77) Newville, M. *Journal of Synchrotron Radiation* **2001**, *8*, 96.

(78) Ravel, B.; Newville, M. *Physica Scripta* **2005**, *T115*, 1007.

(79) Newville, M. *Journal of Synchrotron Radiation* **2001**, *8*, 322.

(80) Zabinsky, S. I.; Rehr, J. J.; Ankudinov, A.; Albers, R. C.; Eller, M. J. *Phys Rev B* **1995**, *52*, 2995.

(81) Rehr, J. J.; Albers, R. C. *Phys Rev B* **1990**, *41*, 8139.

(82) Hall, S. R.; Allen, F. H.; Brown, I. D. *Acta Crystallogr A* **1991**, *47*, 655.

Chapter 2
Experimental Section

Naturally occurring nanoparticles comprise a very complex mixture, thus a dendrimeric method was used to generate metal oxide nanoparticles [1-4]. The proposed method provides a means of "tuning" the size distribution of the nanoparticles. The nanoparticles were prepared by using a family of diaminobutane (DAB) core poly (propylene imine) dendrimers coordinated to a transition metal ion (i.e. Cu and Ni).

2.1 Materials

$Cu(NO_3)_2 \cdot 2.5H_2O$ (Copper (II) nitrate) and $Ni(NO_3)_2 \cdot XH_2O$ (Nickle (II) nitrate) were used as received (Aldrich, CAS# 19004-19-4). 99.99% metal base anhydrous Cu_2O powder, CuO and NiO purchased from Aldrich were used as standards. Both generation three and four diaminobutane (DAB) core, amine-terminated poly (propylene imine) dendrimer (DAB-Am_{16} and DAB-Am_{32} respectively) were purchased from SyMO-CHEM (CAS# 163611-04-9). Cab-O-Sil high purity fumed silica (SiO_2) powder (>99.8%) with high surface area (380 m^2/g, EH-5) and high purity SpectrAl^{TM}100 (95 m^2/g, Cationic) fumed alumina (Al_2O_3) powder were purchased from CABOT Corporation. High purity anatase grade titanium dioxide (TiO_2/ titania) powder (9.5 m^2/g) was purchased from Aldrich. These inert oxides were used as the supporting matrix for the metal oxide nanoclusters.

2.2 Dendrimers

The first successful synthesis of highly symmetrical cascade polymers, commonly known as dendrimers, was reported in 1985 [5,6]. However, the earliest dendrimer synthesis approach was reported in the 1970's [7]. Over the years, these types of dendritic molecules have received attention for properties such as high solubility, high reactivity and high miscibility, as well as,

their wide range of applications. Due to their extensive branching and predominantly higher surface functionality, dendrimers can be easy separated from other classic linear and cross-linked polymers. The placement of a functional group at the end of the polymer chain or in a well-defined segment can be used to control or determine the ultimate properties of such polymers. Three-dimensional (3-D) synthetic polymers, such as dendrimers, can be functionalized to encapsulate reactive sites to provide the researchers with highly controlled surfaces and interfaces [8]**.** Therefore, these 3-D symmetrical polymers are not only capable of acting as contrasting agents in magnetic resonance imaging and medicine (drug delivery systems) but also have significantly contributed to many other areas, including molecular recognition, catalysis and environmental studies.

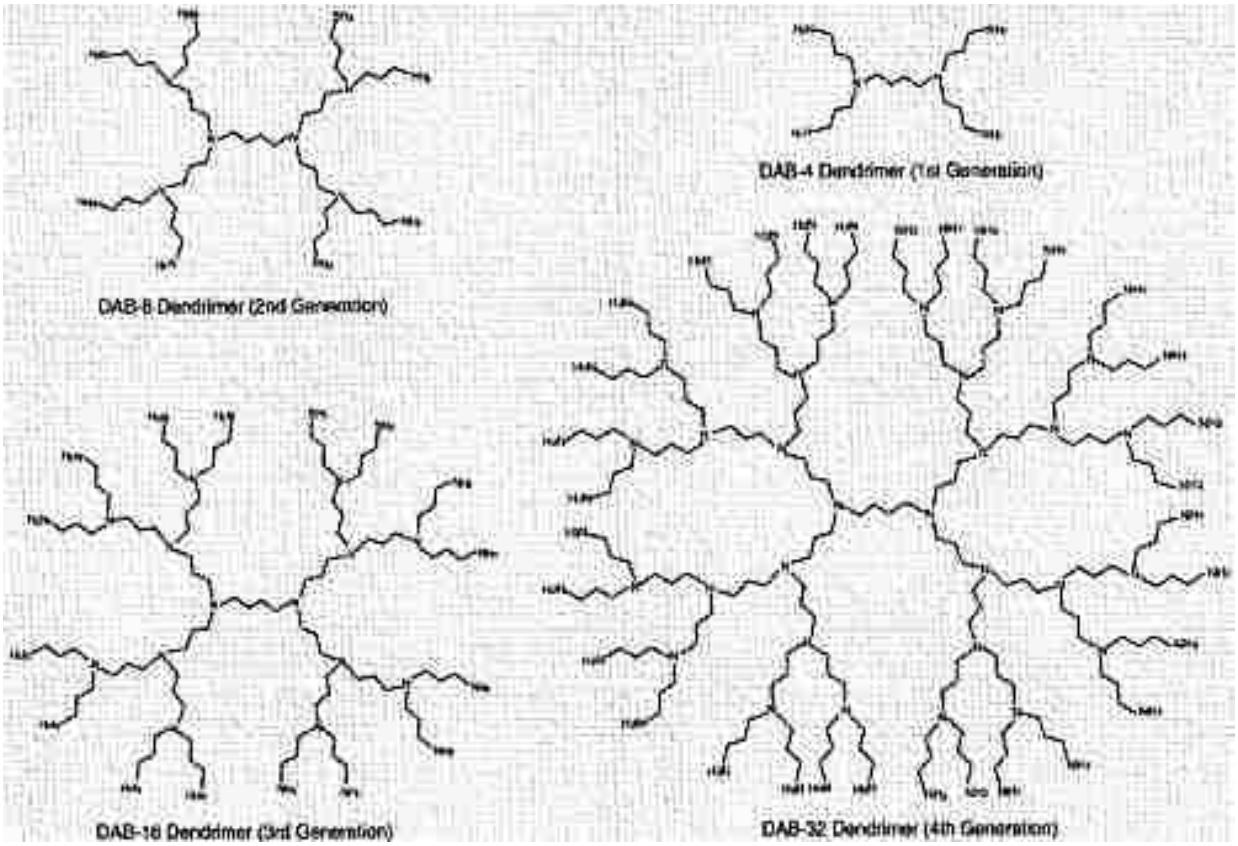

Figure 2.1 Structure of DAB (poly (propylene imine)) dendrimers [9].

Although over the years various other novel dendrimers have been synthesized and designed, PAMAM (poly (amidoamine)) and DAB (poly (propylene imine)) dendrimers [5,10] have remained popular because of their commercial availability. DAB dendrimers were first synthesized by de Brabander-van den Berg and Meijer in 1993; since then, many different studies, such as molecular recognition, physical encapsulation and self-assembly, have been reported on DAB dendrimers and their derivatives [9].

The diaminobutane core poly (propylene imine) dendrimers (DAB-(Am)*n*) have stronger capability of forming stoichiometric complexes with metal ions such as Cu, Ni, Zn and Co. Such metal-ion-dendrimer species can be used to produce metal/ metal oxide nanoparticles upon reduction [1-3]. During my studies, I was using the capability of these dendrimeric molecules (DAB-(Am)*n*) in the formation of dendrimer–metal ion complexes as precursors to form metal oxide nanoparticles [11].

2.3 Preparation of Nanoparticles

2.3.1 Copper Oxide Nanoparticles

A series of CuO nanoclusters were prepared by varying the concentration ratio of the NH_2 groups present in the dendrimer to Cu (II) [(DAB-Am_{32}) : $Cu(II)_N$ (N=0.5,1.0, 2.0, 4.0, 8.0, 16.0)] in methanol. Then, the metal-dendrimer complex, or precursor, was adsorbed (assembled) onto the desired substrate keeping the percentage of the metal oxide at 5 % (w/w) with respect the support substrate (either fumed silica, fumed alumina or titania). The mixture was allowed to settle for about 20 minutes with occasional swelling. Next, the solvent was removed by using a rotary vacuum evaporator. Then, the dendrimer template of the metal oxide nanoparticle complex is removed by thermal oxidation in a furnace (calcined) at 450 ^{0}C for three hours.

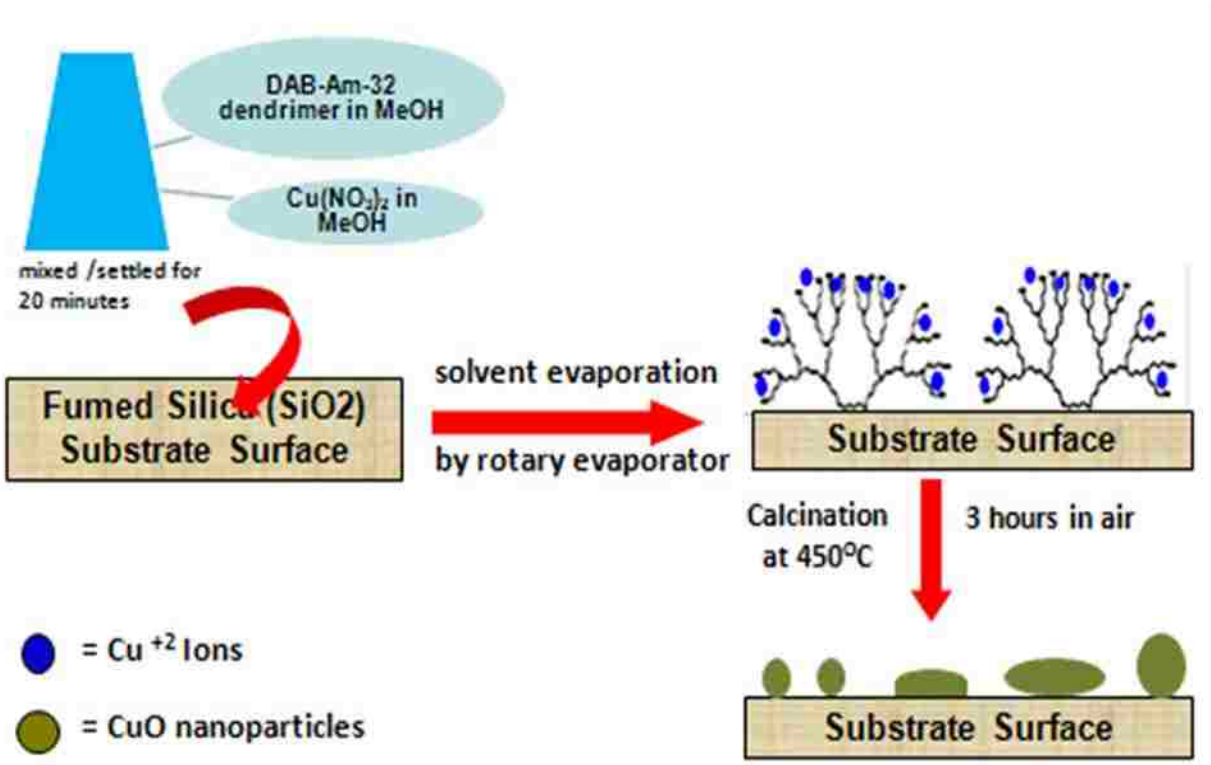

Figure 2.2 Schematic diagram of dendrimeric preparation of CuO nanoparticles.

Notation

$DAB\text{-}Am_{32} : Cu(II)_N$ where **N= 0.5,1.0, 2.0, 4.0, 8.0, 16.0**

N=16, **$DAB\text{-}Am_{32} : Cu(II)_{16}$** , fully doped condition and denoted as **2:1**

N=8, **$DAB\text{-}Am_{32} : Cu(II)_8$** , half doped condition and denoted as **4:1**

N=4, **$DAB\text{-}Am_{32} : Cu(II)_4$** , quarter doped condition and denoted as **8:1**

N=2, **$DAB\text{-}Am_{32} : Cu(II)_2$** , 1/8 doped condition and denoted as **16:1**

N=1, **$DAB\text{-}Am_{32} : Cu(II)_1$** , denoted as **32:1**

N=0.5, **$DAB\text{-}Am_{32} : Cu(II)_{0.5}$** , denoted as **64:1**

} severely under doped condition

2.3.2 Bimetallic Nanoclusters

Bimetallic nanocluster samples were prepared such that the total concentration of metal ions in solution was 0.100 M and the concentration ratio between metal ions to DAB(G3) 0.100 M : 0.200 M. The 0.100 M metal ion solutions were prepared by mixing 0.100 M $Cu(NO_3)_2$ and 0.100 M $Ni(NO_3)_2$ as follows

Table 2.1 Mixing ratio of Ni^{+2} and Cu^{+2} ions.

V (Cu^{+2})mL	V (Ni^{+2})mL	DAB(G3)mL	Cu:Ni
7.50	2.50	10.00	3:1
2.50	7.50	10.00	1:3
9.10	0.90	10.00	10:1
0.90	9.10	10.00	1:10
5.00	5.00	10.00	1:1
Total volume of the solution = 20.00 mL			

Bimetallic nanoparticle samples were prepared to have 5% metal oxide coverage on the fumed silica surface. The same procedure was used during the synthesis of all the different type of nanoparticles on different substrates throughout the entire project.

2.3.3 Metal oxide nanoparticles in the surface mediated reactions

To investigate the contribution of the size controlled metal oxide nanoparticles in surface mediated reactions, experiments were performed by exposing different size nanoparticles to model precursors, which have been reported to form polychlorinated dibenzo-p-dioxins or polychlorinated dibenzofurans, for a certain period of time (ten minutes). Then X-ray absorption spectroscopic experiments (both EXAFS and XANES) were performed on the exposed nanoparticles. The spectra were then compared to the unexposed samples to check the changes in

the absorption edge as well as the radial distribution functions for geometry changes in metal oxide nanoclusters during the chemisorption process.

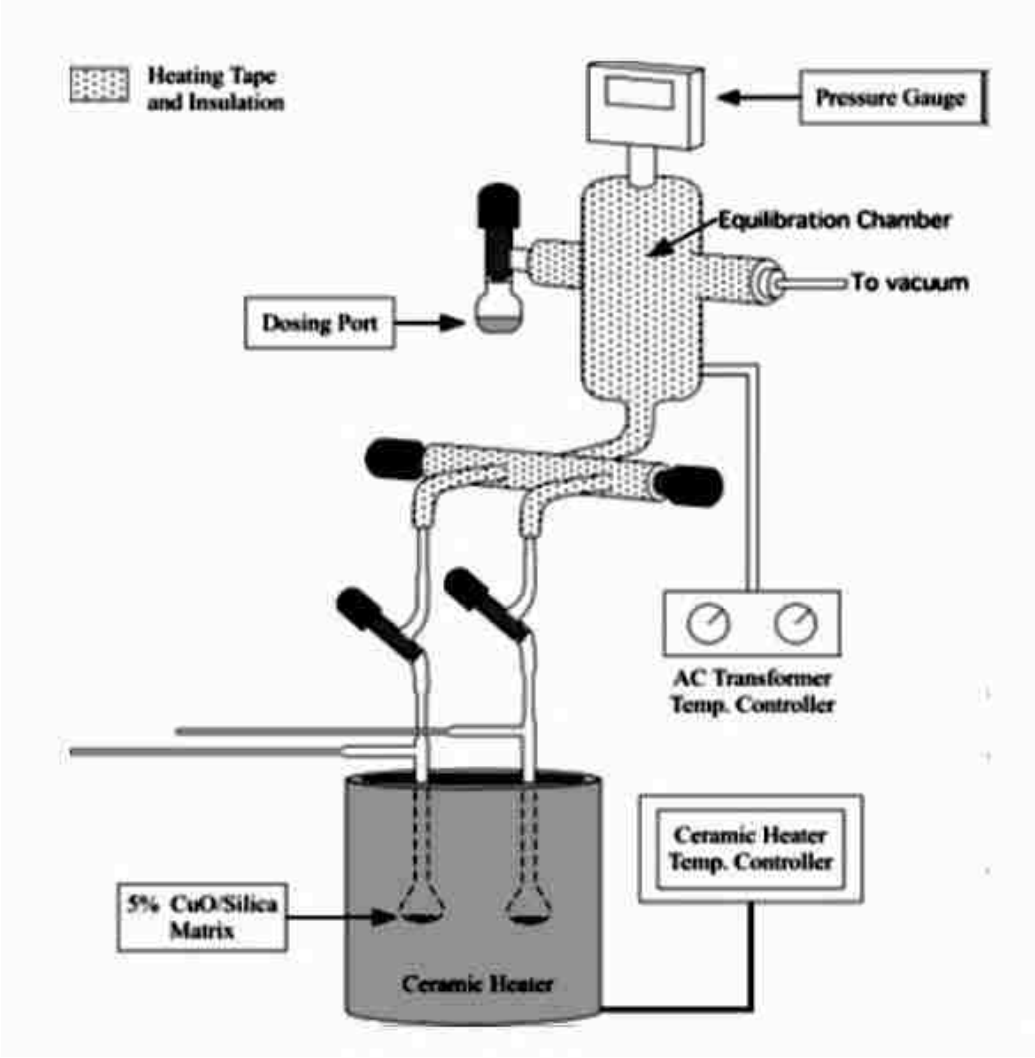

Figure 2.3 Custom-made vacuum exposure system in Dr. Dellinger's lab [12].

2.3.4 Temperature Control Dosing of Nanoparticles

The nanoparticle samples were exposed to the vapors of the adsorbates using a custom-made vacuum exposure system as in the figure above. Each sample was activated (pre heated at 450 ^{o}C / reoxidized) in situ in air at 450 ^{o}C for an hour and then evacuated to 10 $^{-2}$ Torr. Then, portions of nanoparticles were dosed with adsorbate vapors at 10 Torr at temperatures ranging from 200 ^{o}C to 400 ^{O}C at 25 ^{o}C increments for 5 min. The port and dosing

tube were evacuated for 1 h at the dosing temperature and 10^{-2} Torr to remove any residual dosant. The reactor was then sealed under vacuum with a vacuum-tight PFE stopcock and allowed to cool to room temperature for the next sample.

2.4 Double Crystal Monochromator (DCM) Beamline

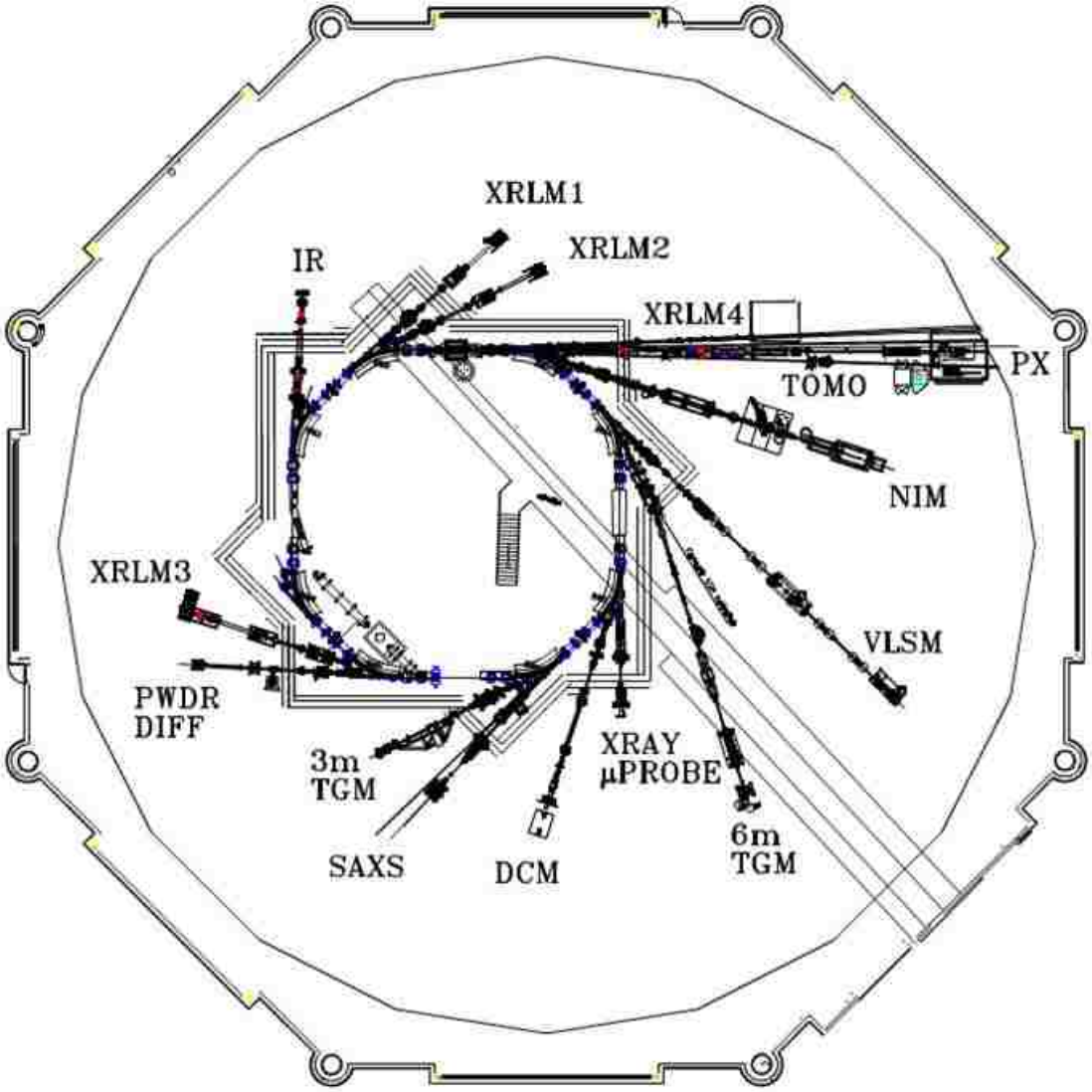

Figure 2.4 Floor diagram of the CAMD experimental floor [13].

During this study, to ascertain the structure and oxidation state information for metal oxide nanoparticles of interest to our group and collaborators in the Superfund Research Group, all measurements were performed at the bending magnet double crystal monochromator

beamlines (DCM) of the Center for Advanced Microstructures and Devices (CAMD) , the synchrotron radiation source at Louisiana State University [13,14] . Here, the sample sizes were not terribly demanding and the samples contained only 5% metal oxide concentration, therefore the DCM beamline at CAMD was an ideal tool for performing the proposed study.

Table 2.2 Monochromator Crystals and energy ranges [15,16].

Crystal	2*d* (Å)	E (eV)
KAP (001)	26.632	510 - 1800
Beryl (1010)	15.954	860 - 3000
YB66 (400)	11.72	1170 - 4090
InSb (111)	7.481	1830 - 6400
Si (111)	6.271	2180 - 7640
Ge (220)	4.00	3420 - 11980
Si (220)	3.840	3560 - 12470

The DCM is the workhorse of the X-ray group at CAMD and it has always been in its maximum usage since its installation in 1994. The beamline is located at port b of the 5th dipole chamber on the bending magnet. The lowest energy for successful data collection is at the Cu L_{III} edge at 0.932 keV and the highest is the Mo K edge at 20 keV. Data can be collected from a wide variety of samples associated with a variety of research areas, such as materials science, catalysis, geology, agronomy, and environmental science. The DCM beamline accepts 2mrad of radiation from the bending magnet. The Lemonnier-Bonn monochromator seats a single pair of crystals, and the angular range of the monochromator is roughly 15° - 65°.

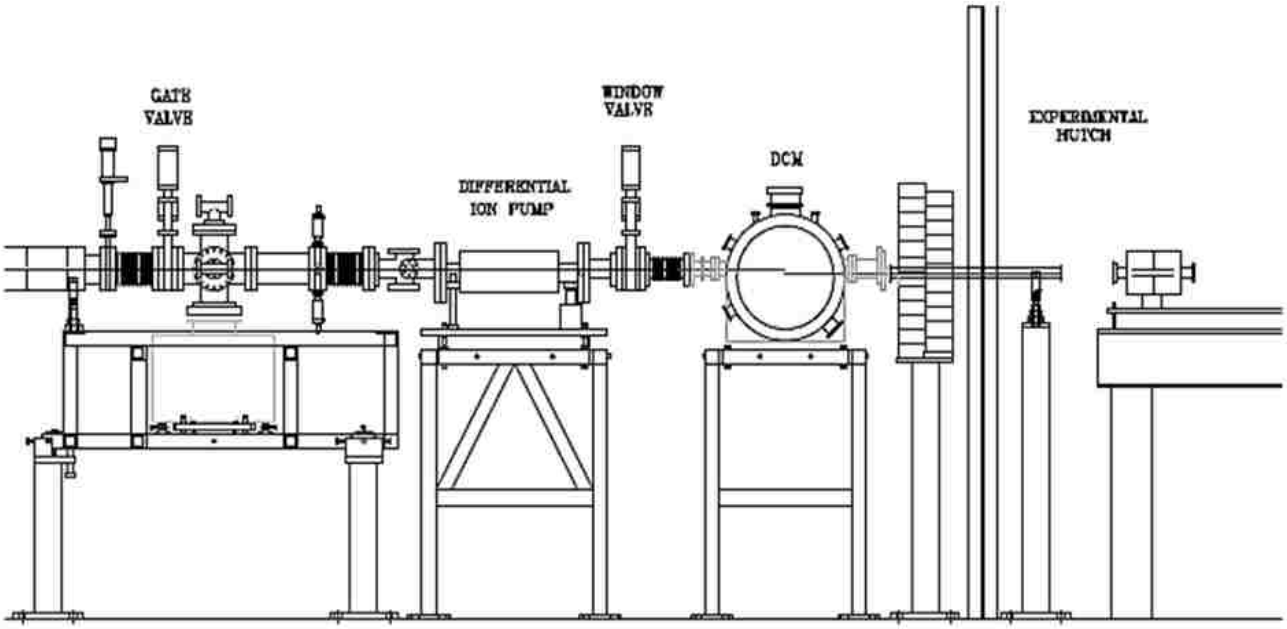

Figure 2.5 Schematic diagram of X-ray double crystal monochromator beamline at CAMD [15,16].

The energy range of the beamline corresponds to the crystals that are used in the monochromator. Therefore, the energy of the beamline can be optimized according to the experiment or the sample. The resolution is 0.5 eV at low energies and 2 eV at high energies. The beam position of the beamline is monitored by a photon beam position monitor at all times. XAS can be measured in terms of transmission, fluorescence, and electron yield modes. Detectors available in this beamline include ionization chambers, a Peltier-cooled Si(Li) detector, a 13-element germanium diode array fluorescence detector and Lytle fluorescence and electron yield detectors [15,16].

2.5 EXAFS and XANES Measurements

Both EXAFS and XANES experiments were performed at the bending magnet double crystal monochromator (DCM) x-ray beamline with a Lemonnier-type monochromator equipped with a pair of Si/Ge (220) crystals. The ring was operated at 1.3 or 1.5 GeV with corresponding average beam currents of 200 and 150 mA. In general, the injection current was maintained

roughly 200 mA and injections were typically done before the beam decayed below 50 mA. The EXAFS and XANES spectra were collected in the fluorescent mode by using the 13 channel (element) germanium detector placed 90° to the incident beam and as close as possible to the sample.

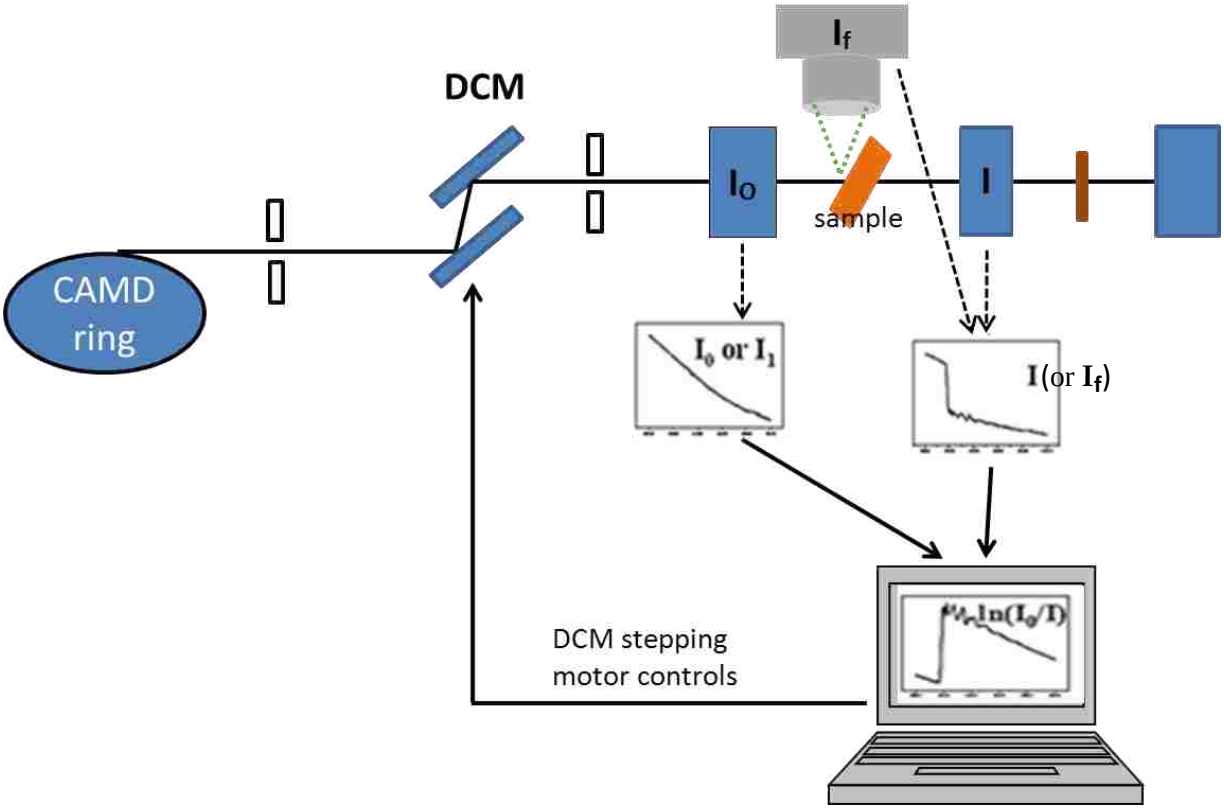

Figure 2.6 Schematic diagram of X-ray absorption spectroscopy set-up at CAMD.

Samples consisted of metal oxide nanoparticles supported on fumed silica, alumina or titania substrates, which were finely ground using a mortar and pestle. A thin layer of fine particles was dispersed onto a piece of Kapton tape. The sample was placed at 45° to both the incident beam and the detector in the horizontal plane.

The X-ray absorption data for metal oxide standards were collected at their respective edges (eg; Cu K-edge 8979 eV and Ni K-edge 8333 eV) in transmission mode. The incident beam current, I_o, was measured by an ionization chamber placed before the sample.

Transmission measurements were taken by monitoring the current in an ionization chamber placed after the sample. In addition, a copper foil was scanned during the entire experiment for calibration purposes in a third ionization chamber. Also, the calibration was checked between injections as well as upon changing samples. Reported data for both EXAFS and XANES were the average of separate scans. The average depended upon the number of counts for each corresponding scan. Both XANES and EXAFS spectra for the Cu or/and Ni oxide nanoclusters were compared with the NiO, CuO and Cu_2O standards.

2.6 Data Reduction and Refinements

Data reduction and analysis, which involves reading in beamline data, merging data sets, deglitching, aligning the spectra, shifting energies, subtracting the pre-edge, finding E_0, normalizing the spectra, subtracting the background to $\chi(k)$, Fourier transforming $\chi(k)$ to χ (R), simple data plotting and saving/reading projects, were carried out by using a well-established program in the IFEFIT library (ATHENA). The ARTEMIS program was used for data analysis in conjunction with FEFF 8.2 throughout this project. Even though data were available for *k* range from 0 to 15 $Å^{-1}$, truncation of the k range was done to eliminate low-*k* and high-*k* noise contributions. A range of $k = 2 - 12$ $Å^{-1}$ was selected for the Fourier transforms. The range chosen for the back-transform window was 1- 6 Å, and kaiser-bessel was selected as the analysis window.

2.7 Electron Microscopic Images and Analysis

Initial microscopic studies were performed with the JEOL-2010 transmission electron microscope at the Material Characterization Center (MCC) at Louisiana State University. Most of the work with transmission electron microscopy (TEM) was performed at the "Central Microscopy Research Facility (CMRF)" at University of Iowa because the instrument there has

more extensive capabilities. CMRF has the capability of providing a wide variety of microscopy techniques for materials and biomedical investigators with the aid of experienced staff. This facility has three TEMs (JEOL 1220, JEOL JEM-1230 and JEOL 2100f) and two Scanning Electron Microscopes (Hitachi S-4800 and Hitachi 3400N).

Dr. Jonas Baltrusaitis conducted our experiments at the CMRF. Here, the JEOL 2100f field emission TEM equipped with a nanotrace EDS detector and a user-friendly high performance Hitachi S-3400N SEM equipped with an EDS chamber (3.0 nm resolution in high vacuum mode) were used to collect the respective microscopic images. The TEM was operated at an acceleration voltage of 200 kV and at different standard magnifications (200-500 K). The SEM has the capability to operate in a unique VP-mode that allows for microscopy of non-conductive, wet and oily samples in their natural state (without the conventional sample preparation) at a resolution of 0.4 nm.

During our experiment, a drop of the analyte solution in methanol was placed on a carbon-coated gold TEM grid, and the solvent was allowed to evaporate. Then, samples were placed under the microscope for morphological analysis and the TEM (JEOL 2100f) was operated in bright field mode at an acceleration voltage of 200 kV (with different standard magnifications). For each sample, particles from different parts of the grid were used to determine the average diameter and size distribution of particles and elemental analysis was performed with an energy dispersive system (nanotrace EDS detector) attached to the microscope.

2.8 References

(1) Floriano, P. N.; Noble, C. O.; Schoonmaker, J. M.; Poliakoff, E. D.; McCarley, R. L. *J Am Chem Soc* **2001**, *123*, 10545.

(2) Mitran, E.; Dellinger, B.; McCarley, R. L. *Chem. Mater.* **2010**, *22*, 6555.

(3) Velarde-Ortiz, R.; Larsen, G., *Chem. Mater.***2002**, *14*, 858.

(4) Bosman, A. W., Dendrimers in action: structure, dynamics and functionalization of poly (propylene imine) dendrimers, PhD. Dissertation, Technische Universiteit Eindhoven, 1999.

(5) Tomalia, D. A.; Baker, H.; Dewald, J.; Hall, M.; Kallos, G.; Martin, S.; Roeck, J.; Ryder, J.; Smith, P. *Polym J* **1985**, *17*, 117.

(6) Tomalia, D. A.; Baker, H.; Dewald, J.; Hall, M.; Kallos, G.; Martin, S.; Roeck, J.; Ryder, J.; Smith, P., *Macromolecules* **1986**, *19*, 2466.

(7) Buhleier, E.; Wehner, W.; Vogtle, F. *Synthesis* **1978**, *2*, 155.

(8) Fréchet, J. M. J., *Science* **1994**, *263*, 1710.

(9) Chai, M.; Niu, Y.; Youngs, W. J.; Rinaldi, P. L., *J Am Chem Soc* **2001**, *123*, 4670.

(10) Worner, C.; Mulhaupt, R., *Angew Chem Int Edit*, 1993, *32*, 1306.

(11) Lomnicki, S. M.; Wu, H.; Osborne, S. N.; Pruett, J. M.; McCarley, R. L.; Poliakoff, E.; Dellinger, B. *Materials Science and Engineering: B* **2010**, *175*, 136.

(12) Lomnicki, S.; Truong, H.; Vejerano, E.; Dellinger, B., *Environ Sci Technol* **2008**, *42*, 4982.

(13) Schilling, P. J.; Morikawa, E.; Tolentino, H.; Tamura, E.; Kurtz, R. L.; Cusatis, C. *Review of Scientific Instruments* **1995**, *66*, 2214.

(14) Stockbauer, R. L.; Ajmera, P.; Poliakoff, E. D.; Craft, B. C.; Saile, V. *Nuclear Instruments and Methods in Physics Research Section A: Accelerators, Spectrometers, Detectors and Associated Equipment* **1990**, *291*, 505.

(15) The ROSE Report: CAMD, Past, Present and Future, 2009 http://www.camd.lsu.edu/pdf/Rose_Final_06-19-2009.pdf (accessed March 23, 2012).

(16) LSU-CAMD. Beamlines: Double-Crystal Monochromator (DCM). http://www.camd.lsu.edu/beamline_info/DCM_beamline_2008.pdf (accessed March 23, 2012).

Chapter 3
X-ray and TEM studies of Dendrimerically Generated Copper Oxide Nanoparticles Tethered to Fumed Silica

3.1 Background

Ambient airborne fine particles of different composition and size are recognized as a major component for most dangerous health and environmental effects [1-3]. Over the last few decades, studies have been carried out to address this issue, and it has been identified that most of these demonstrable health impacts are probably due to nanometer size fine particles [4-6]. Most of these fine particles or nanoparticles enter the environment by combustion related activities, and manufactured or engineered nanoparticles, which are used in hundreds of commercial products (i.e., sunscreens, cosmetics, textiles, pharmaceuticals, tires, electronics and so on) [7,8], can enter the environment as well.

With the advancement of society, there is a need to increase the products and services to fulfill day-to-day requirements, which in turn, increases the combustion related activities as well as the production and the uses of nanoparticles. Hence, there is a greater possibility for releasing different types of nanoparticles into the environment. Due to their small size, these nanoparticles can be transported over longer distances in the atmosphere and penetrate deep into the respiratory system, enhancing the potential of hazardous health impacts [5,9-11].

Assessments of environmental fate and mobility of nanoparticles is a must to consider the behavior of nanoparticles in relevant environmental systems and to check the speciation changes over time. Environmental conditions may act on nanoparticles to change their basic characteristics like size, shape, and surface chemistry; this may result in a final species which is significantly different from the initial nanomaterial. These physical and chemical transformations

of the nanoparticle generally include agglomeration, oxidation, which is influenced by aging on the speciation, and chemical stability of the nanoparticles in the environment [12].

Therefore, metal oxide nanoparticles have been studied intensively for numerous reasons and can be looked at from two different perspectives. From an applied perspective, it is known that well-defined nanometer size metal oxides have a number of applications not only in environmental related research, but they also have important catalytic and semiconductor properties, as well as useful electronic and optical properties [13-19]. From a fundamental perspective, it is interesting to evaluate if the basic chemical and physics properties in nanometer size metal oxides are different from macroscopic metal oxide systems.

3.2 Motivations and Goal

The primary motivation for the current study was to understand how metal oxides can have largely unanticipated effects on the environment. It is already recognized that the particulate matter in the environment, such as combustion generated airborne fine particles and the nanoparticles which leach into the environment as byproducts, consist of oxides of silica and alumina, transition metals of Ni, Cu, Fe and Zn and their oxides, semi-volatile sulfates and chlorides, other metal nanoparticles, and high molecular weight organic compounds [20-22]. Nanoparticles of transition metal or metal oxides tethered to inert oxide surfaces provide the basis to many heterogeneous catalysts that are really important in energy research, environmental cleanup and pollution prevention [23]. Catalytic activity can be strongly dependent on the nanoscale metal/metal oxide cluster size, oxide support and the extent of the reduction of the oxide [16,17]. These nanoscale metal/metal oxide clusters provide higher surface area and low coordination sites which are responsible for higher catalytic activity [17,24].

Recent studies have shown metal oxides can adsorb organic molecules, and form free radicals which persist for orders of magnitude longer than typical free radicals [25-27]. It has been observed that the lifetime of these free radicals are on the order of hours or even days [27-29]. Such long-lived interfacial pollutants have been referred to as environmentally persistent free radicals or EPFRs [26,27,29]. The current study is part of a larger effort to understand the influence of long-lived environmentally persistent free radicals (EPFRs) on biological systems. These EPFRs are interfacial pollutants, and they exist because organic molecules are chemisorbed to metal oxide surfaces, resulting in electron transfer from the organic moiety to the metal oxide substrate. Thus, it is necessary to study the structure and electronic properties of the transition metal oxide nanoparticles as a substrate in order to develop a microscopic understanding of the formation of EPFRs. Therefore, it is essential to understand the structures and chemical characteristics of such nanoparticles on inert oxide supports which are more likely to cause hazardous environmental and health effects. It is also important to understand how molecules are adsorbed onto the nanometallic surfaces and also how these nanoparticles attach to the supporting oxide surface because adsorption can produce both particle growth and surface-mediated pollutants [20,30].

Since metal oxide nanoparticles in the environment can exist in many size regimes and very complex local chemical surroundings, we have taken an approach that allows us to work with relatively simple and reproducible systems, i.e., metal oxide nanoparticles that were relatively nanodispersed and of simple composition [31,32]. It is clear from reviewing relevant literature that, the size and the dispersity of the nanoclusters can be manipulated either by choosing dendrimer scaffolds of different generations (size) of the selected dendrimer (i.e. amine-terminated diaminobutane (DAB) core dendrimers) or by adjusting the stoichiometric ratio of the metal ions to the number of NH_2 terminal groups present in the dendrimer [20,32-34]. The

results showed a decreasing trend of nano-structure size with the increasing dendrimer generation. Other studies have shown that other metal ions like Cu, Ni, Fe strongly complex with DAB dendrimers [20,32,35]. Due to these capabilities, size controlled nanoparticles were prepared by using a dendrimeric method.

A primary goal of the current study was to characterize these nanoparticles using X-ray spectroscopy, using EXAFS to ascertain the structure of the nanoparticles and expanding on the earlier XANES spectroscopic studies. X-ray spectroscopic techniques such as XANES and EXAFS probe samples with elemental specificity and were used to study the metallic cores in the complex sample mixtures. Typically, XANES was used to characterize the change in oxidation state or the electronic structure of the metal oxide nanoclusters (finger printing tool), and EXAFS was used to clarify the local geometry of the targeted species around the metal center of interest. The data analysis was typically performed with the help of ATHENA, ARTEMIS and feff8.2 software programs [36-40].

3.3 Experimental Method

Copper oxide nanoparticles of different size, supported on fumed silica, were prepared by using the dendrimeric method as described in the experimental section (chapter two). To perform the experiment at the beamline, samples were prepared by dispersing a finely ground nanoparticle sample uniformly on a piece of Kapton® tape. Then, the sample was placed on the sample stage at a 45° angle to the incident X-ray beam, and spectral data was collected in fluorescent mode. Here, the parameters for the experiment were selected to satisfy the requirements of both XANES and EXAFS. Initial experiments were performed with a silicon drift detector but due to the time constraints, a 13 element germanium (Ge) detector [41,42] was used for the majority of the data collection.

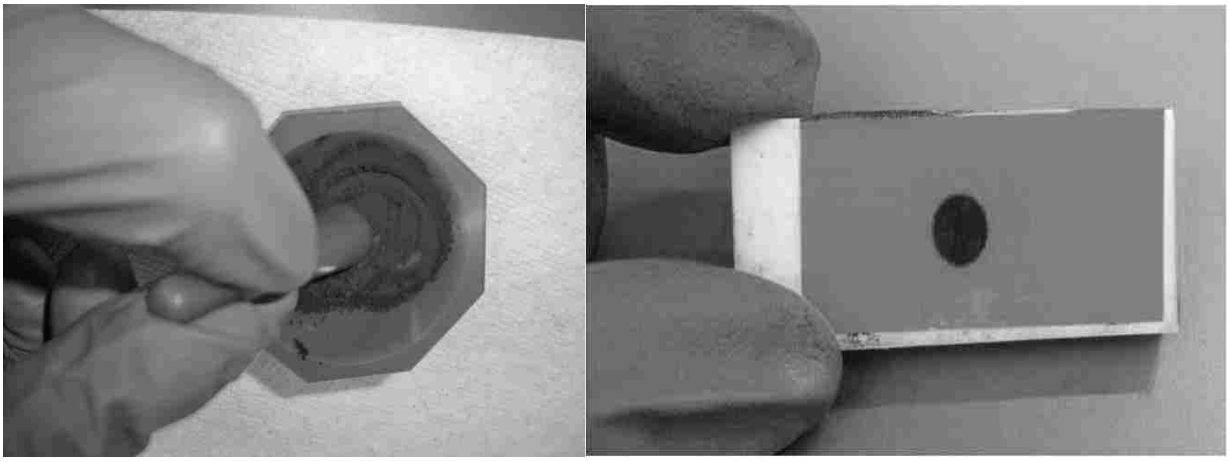

Figure 3.1 Sample preparation for XANES and EXAFS analysis [43]

All the spectral data were collected at the Cu-K edge. ATHENA and ARTEMIS programs were used to process and analyze the beamline data. TEM images of the sample were collected to confirm the findings of the X-ray absorption spectroscopy.

3.4 Results and Discussion

The X-ray absorption spectroscopic data for copper oxide nanoclusters were collected at the Cu K-edge for both the XANES and EXAFS regions and compared with the cupric oxide (CuO) and cuprous oxide (Cu_2O) standards to identify the oxidation state of the copper species. Figure 3.2 shows copper oxide nanoclusters prepared at stoichiometrically saturated or fully doped conditions (number NH_2 groups to Cu ratio of 2:1) have significant differences in the XANES region compared with nanoclusters prepared at the severely under doped (number of NH_2 groups to Cu ratio of 64 :1) conditions. Figure 3.3(a) shows the nanoclusters prepared at the fully, half and quarter doped conditions (2:1 to 8:1) possessed similar spectral features at the near edge region of the XANES spectra. Figure 3.3(b) shows nanoclusters prepared at the severely under doped conditions (32:1 and 64:1) have slightly different spectral features at the same region but have similar shape to each other. When comparing XANES spectra for these

nanoparticles (prepared at different doping ratios) to the copper oxide standards (CuO and Cu_2O), near edge features for 2:1, 4:1, 8:1 and 16:1 doped conditions have not only shifted to higher energy but also the spectral features have changed with respect to the copper standard. However, the nanoparticles prepared at severely under doped condition show a similar near edge spectral feature to cupric oxide (CuO) standard. It should also be emphasized that all of the nanoparticles are more similar to the Cu(II) standard than Cu(I) standards, corroborating the result seen in the previous study [31].

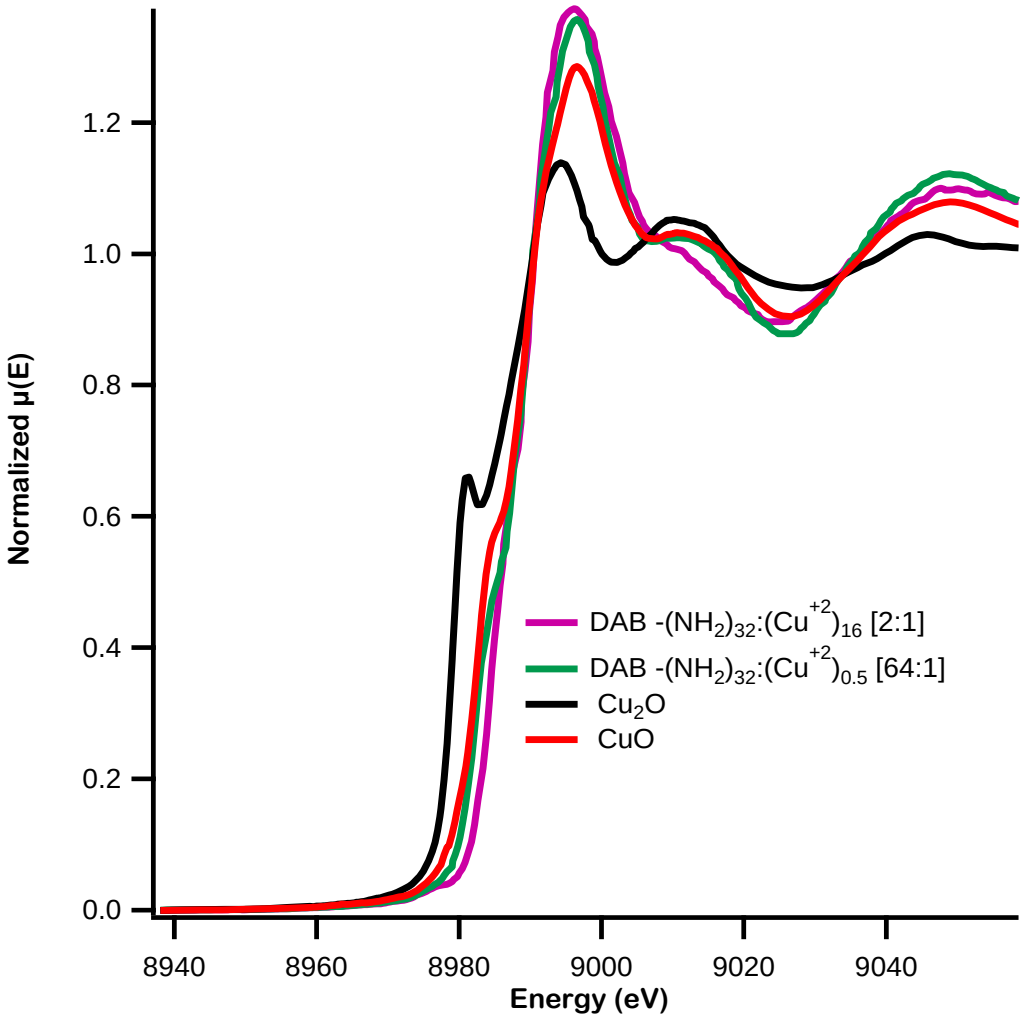

Figure 3.2 XANES spectra for copper oxide nanoparticles prepared at fully doped (2 to 1) and severely underdoped (64 to 1) conditions with both copper oxide (CuO and Cu_2O) standards.

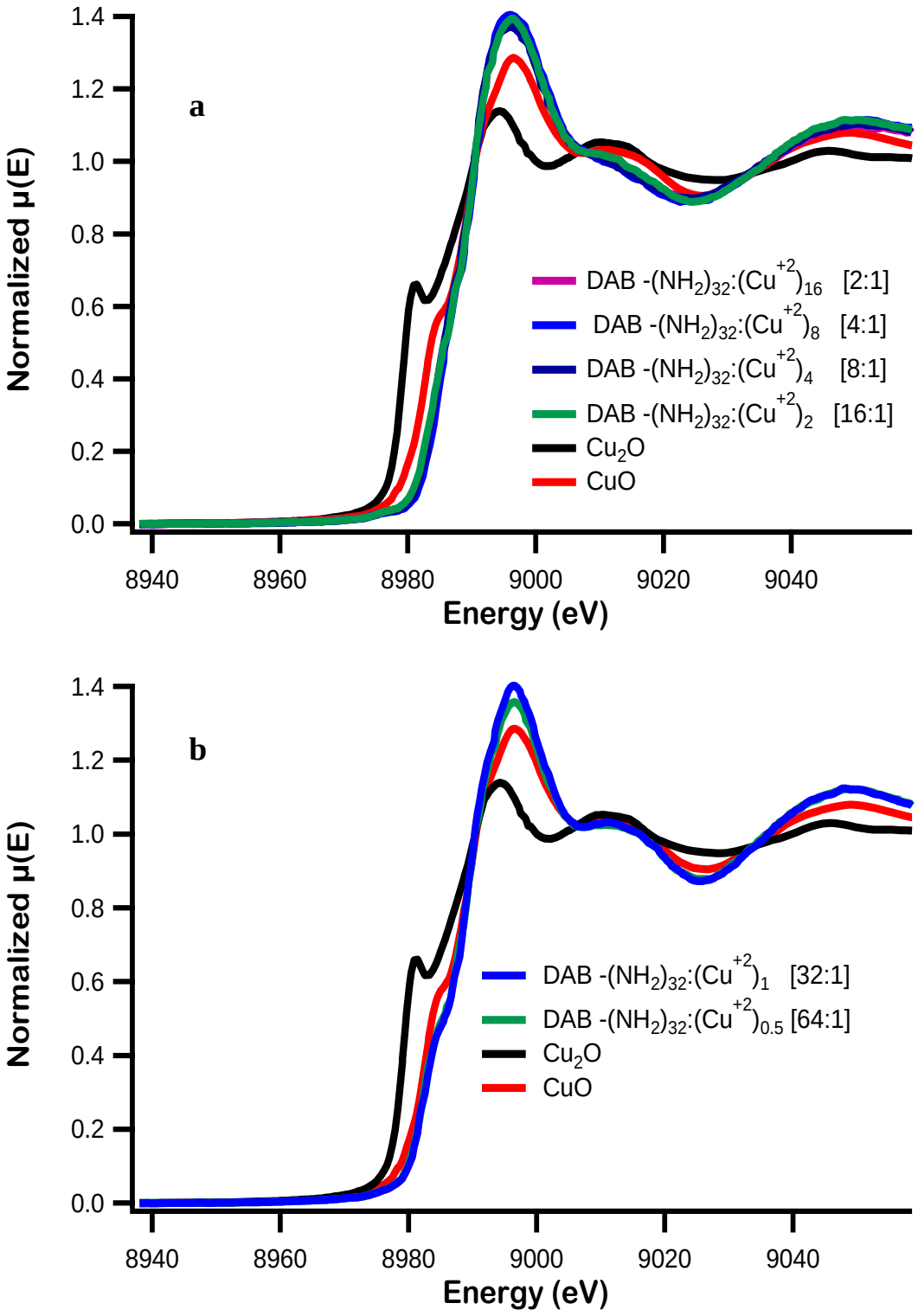

Figure 3.3 XANES spectra for copper oxide nanoparticles (a) Nanoparticles prepared at fully doped (2 :1) to 1/16 doped condition (b) Nanoparticles prepared at severely under doped (64 : 1 and 32:1) conditions, with both copper oxide (CuO and Cu_2O) standards.

Even though we observed a shift of the edge to higher energy for our samples, we have not seen the intense pre-edge features at 8986-8988 eV responsible for the higher oxidation state of copper (Cu (III)) customarily assigned for 1s→4p + LMCT shakedown transition [44]. According to the information gathered from Hodgson at al. and the relevant recent literature, the edge shift present in our data was probably due to a change in coordination geometry of the copper species in the copper oxide nanoclusters during their respective dendrimeric preparation and calcination [44-46]. XANES spectra in figure 3.2 prove all the copper ions in the nanoclusters were oxidized and mostly corresponded to Cu^{+2} rather than Cu^{+1}. Similarity between spectral features of nanoclusters prepared at the severely under doped conditions and CuO standard further suggested that the copper atoms in the nanoclusters had the same oxidation state as Cu^{+2}.

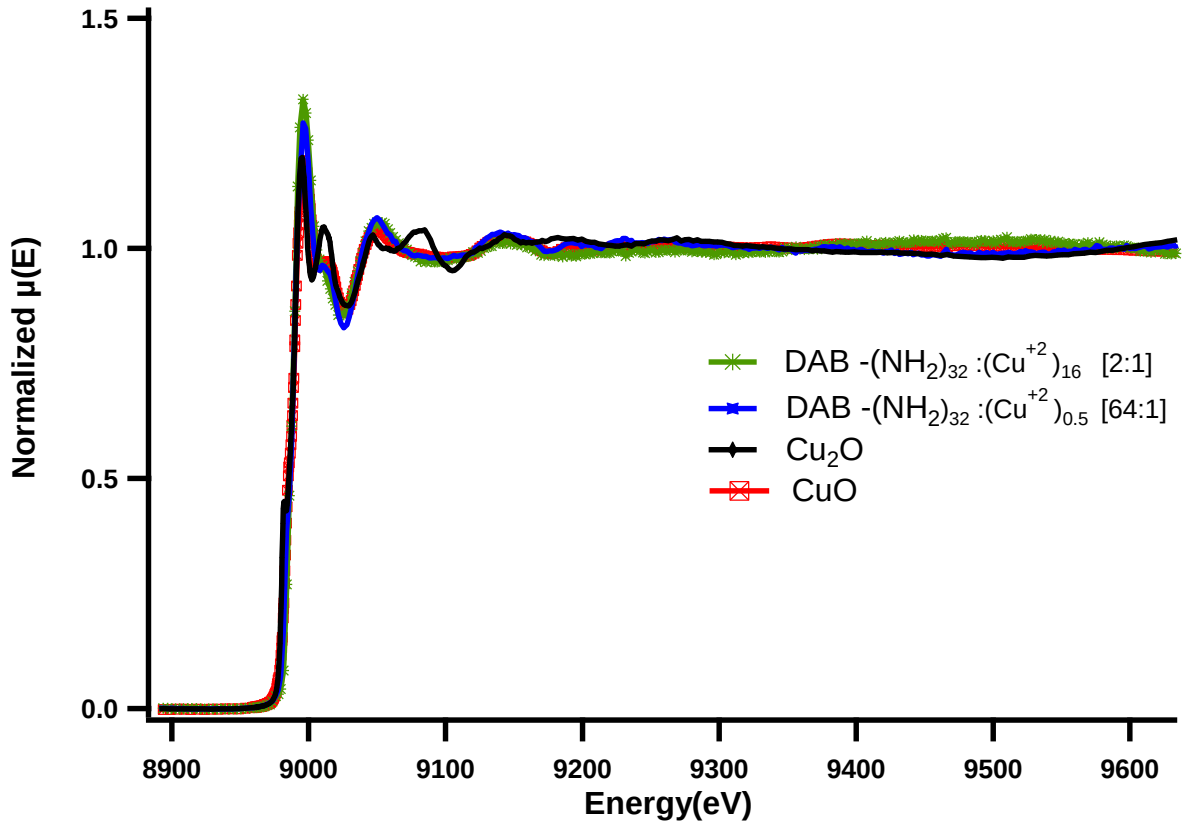

Figure 3.4 EXAFS spectra for copper oxide nanoparticles prepared at fully doped and severely underdoped conditions with copper oxide standards (CuO and Cu_2O).

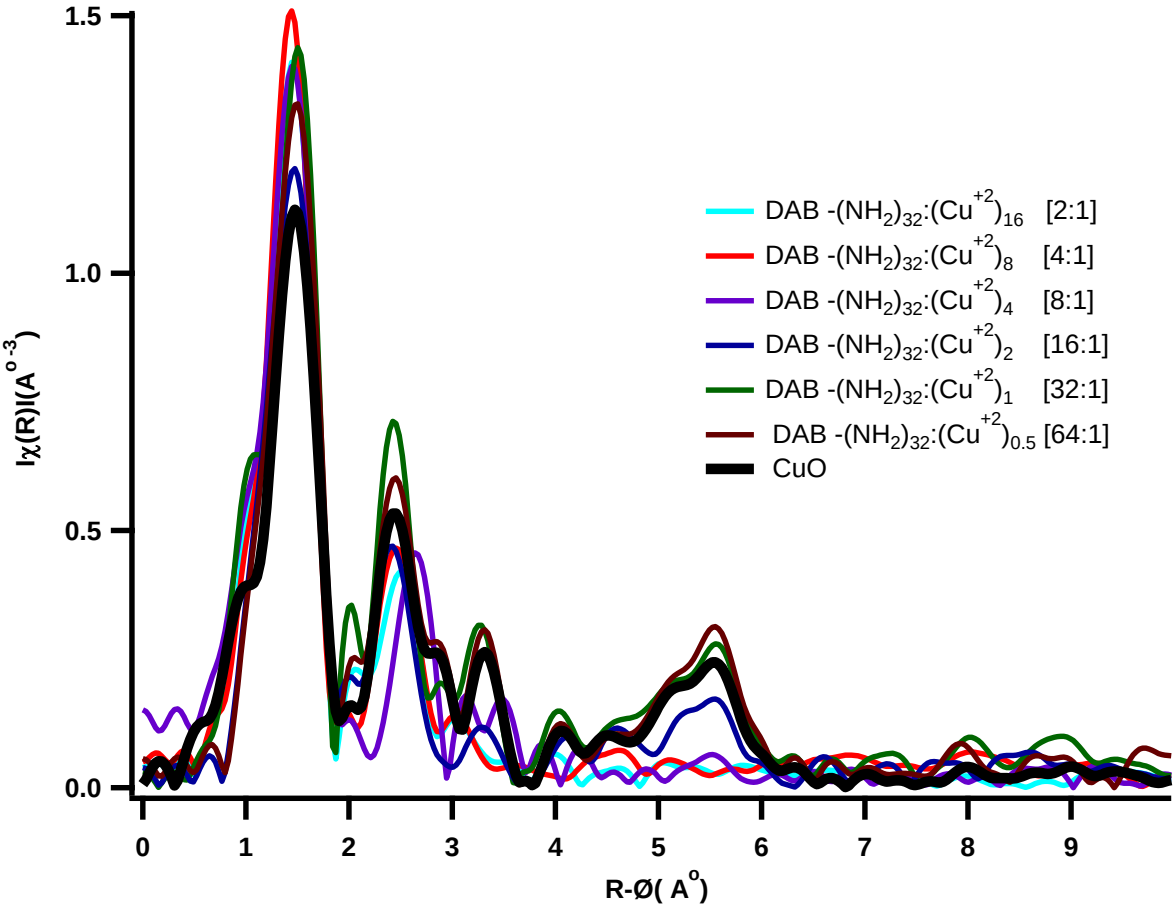

Figure 3.5 Radial distribution functions for copper oxide nanoparticles prepared at all the different concentration ratios between NH_2 groups of the dendrimer and Cu^{+2} ions with cupric oxide (CuO) standard.

Therefore, the Tenorite (CuO, B26) structure was used as the model to compare interatomic distances and coordination numbers of the copper local arrangement in the copper oxide nanoclusters. RDF (R space spectra) obtained from Fourier transformed EXAFS data were used to study the structure and the local geometry of the copper in the nanoclusters prepared at different doping conditions. Figure 3.5 displays the radial distribution functions for all the nanoparticles with the cupric oxide standard. The comparison of RDFs further supported the previous observation, that the nanoclusters prepared at the severely under doped conditions mimic the spectral features of the bulk CuO standard.

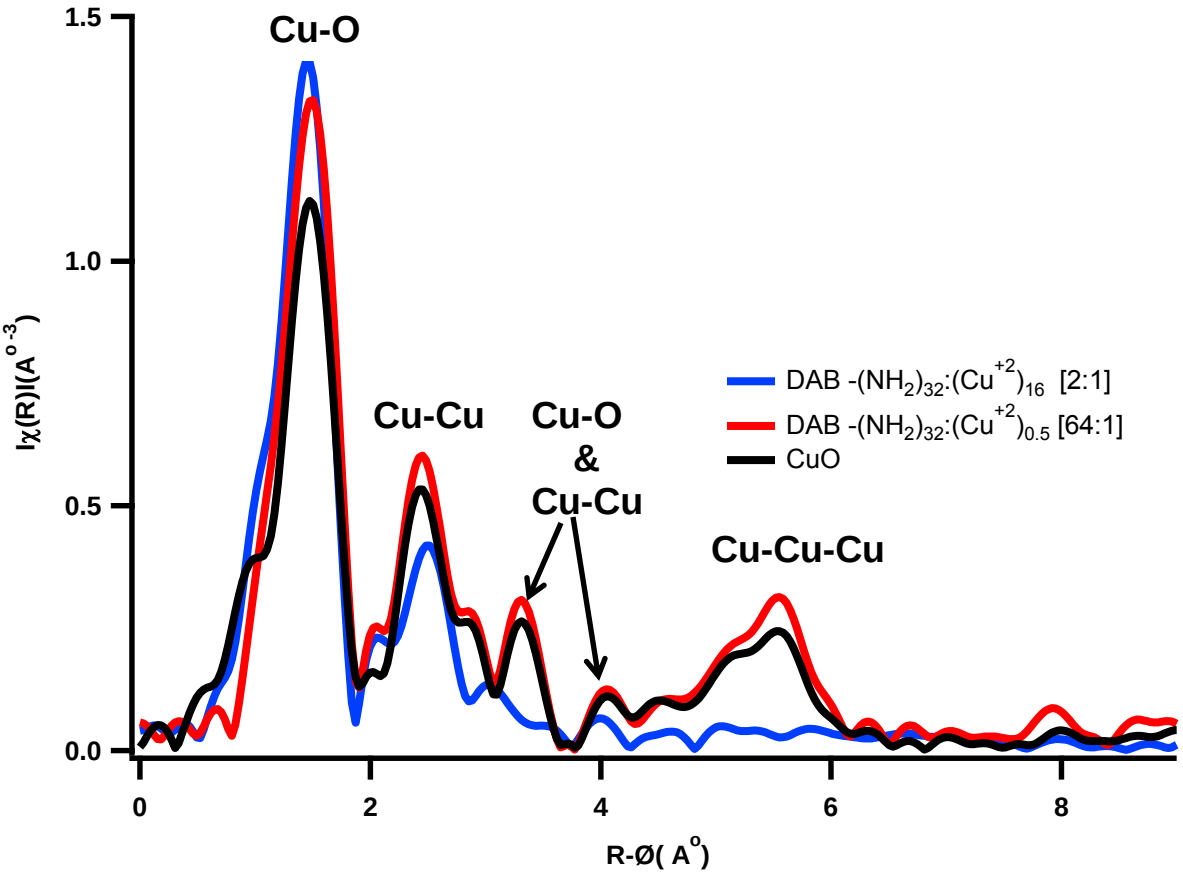

Figure 3.6 Radial distribution functions for copper oxide nanoparticles prepared at both fully doped and severely underdoped conditions with cupric oxide (CuO) standard (Note the differences in the spectra between 2-3 Å and 5-6 Å).

However, there is a significant difference in R space data for the copper oxide nanoclusters prepared at fully doped conditions with both the CuO standard and the nanoclusters prepared at under doped conditions (figure 3.6). Figure 3.6 shows the RDF curves for the nanoclusters prepared at different conditions and CuO standards without phase correction. Observed peaks on the RDF curve for CuO standard at around 1.96, 2.90, 3.75, 4.35 and 5.80 Å correspond to the actual (after the phase correction) interatomic distance from which the photoelectron was scattering back with respect to the central Cu atom. Peaks at 1.96 Å and 2.96 Å correspond to single scattering paths of Cu-O and Cu-Cu respectively. However, the two peaks at 3.75 Å and 4.35 Å exhibited a considerable reduction of intensity corresponding to absence of

the Cu and O neighbors that, contribute to these peaks. The peak around 5.80 Å corresponds to a two legged path where the photoelectron was backscattering from a second shell Cu atom (Cu-Cu-Cu).

Table 3.1 Scattering paths and corresponding distances of the x-ray photoelectron for CuO (cupric oxide) standard

Scattering Paths	Distance (Å)
Cu-O	**1.96**
Cu-Cu	**2.90**
Cu-Cu & Cu-O	**3.75 , 4.35**
Cu-Cu-Cu	**5.80**

As mentioned earlier, comparison of R space data shows that the CuO standard possessed very close spectral similarities to the nanoclusters prepared at severely under doped conditions. Whereas the copper oxide nanoclusters prepared at saturated conditions are much different from the other two spectra beyond 3.0 Å. This indicated CuO nanoclusters prepared at severely under doped conditions showed higher long range order than the nanoclusters prepared at fully doped conditions when they were dispersed on a fumed silica surface. Also, TEM images (figure 3.7) of these respective nanoparticles showed a decreasing trend of particle size when changing the preparation conditions from fully doped (bigger) to quarter doped conditions (smaller).

However, TEM images collected at the same resolution did not indicate the presence of any particles for nanoparticles prepared at severely under doped conditions. Here, we assumed that this could be due to few different reasons, such as inability of the technique (resolution of

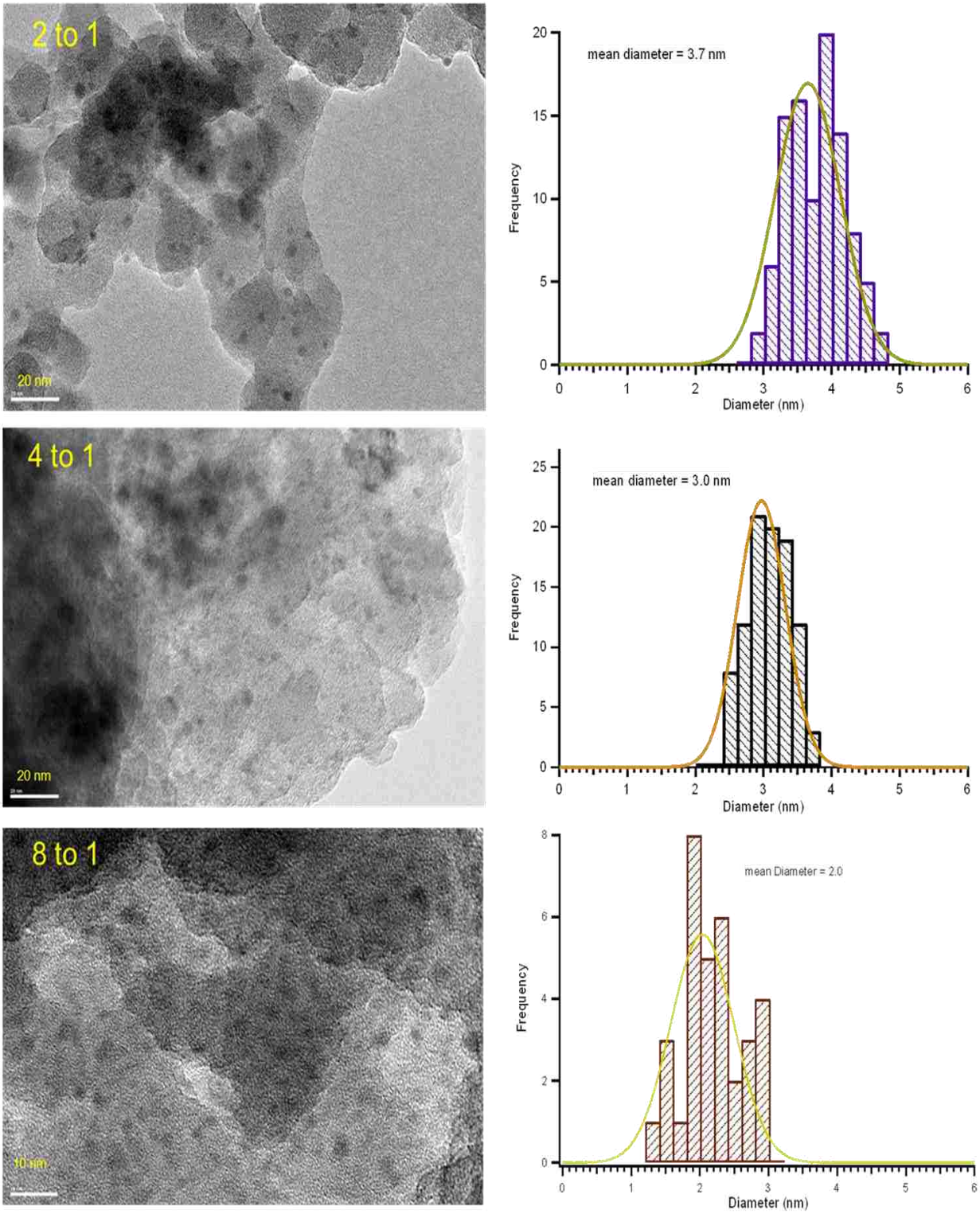

Figure 3.7 TEM images and histograms of nanoparticles prepared at different concentration ratios between NH_2 groups of the dendrimer and Cu^{+2} ions (2 to1 refers to nanoparticles prepared under fully doped conditions).

the TEM) to see smaller size nanoparticles or that under doped conditions may not result in any nanoclusters during the process. We seriously doubt it is for the second reason since we used the same amount of Cu^{+2} ions for every sample, and EXAFS spectra for the samples prepared at same condition mimic the bulk properties of CuO standards. Therefore, further TEM studies were performed with lower resolution at both facilities (along with SEM), and TEM images confirmed that CuO particles prepared at severely under doped conditions did form nanoparticles but they were much larger nanoparticles, ~100nm in size.

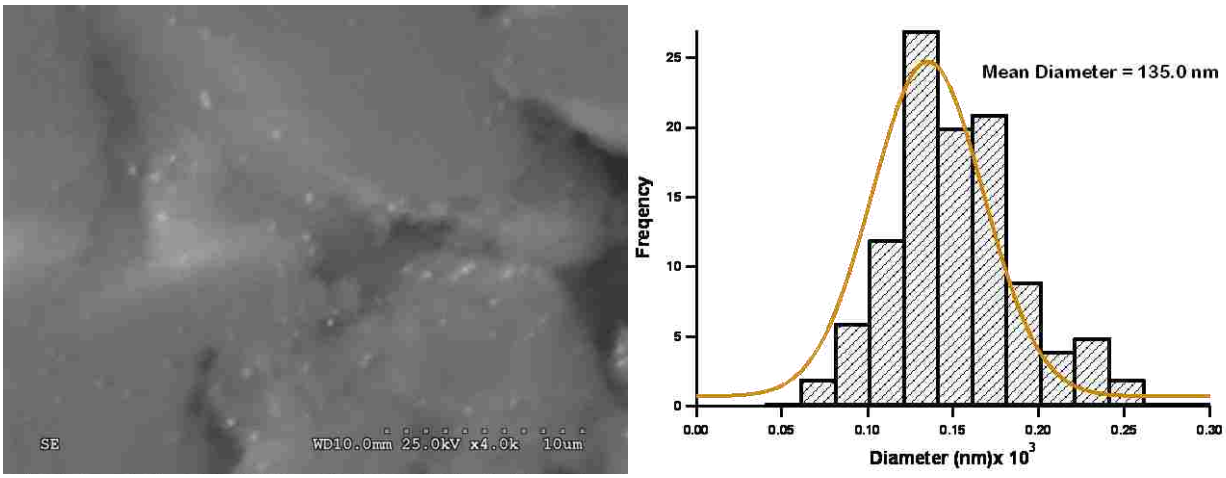

Figure 3.8 SEM image of the nanoparticles prepared at severely under doped conditions (64:1).

Here, we assume that nanoparticles prepared under fully doped conditions produced particles with size approximately ~3.7 Å and may have been located inside the pockets on the fumed silica surface like pancakes, so they did not possess a long range order. Particles that were prepared at severely under doped conditions form much larger (~100nm in size) nanoparticles, or smaller nanoparticles which were agglomerated to form bigger particles in those pockets, so that they possessed relatively higher long range order.

We have performed a few more experiments to understand how the percentage of CuO present on the substrate can affect nanoparticle formation for severely under doped conditions. A set of experiments was carried out by changing the percentage of copper oxide present in the

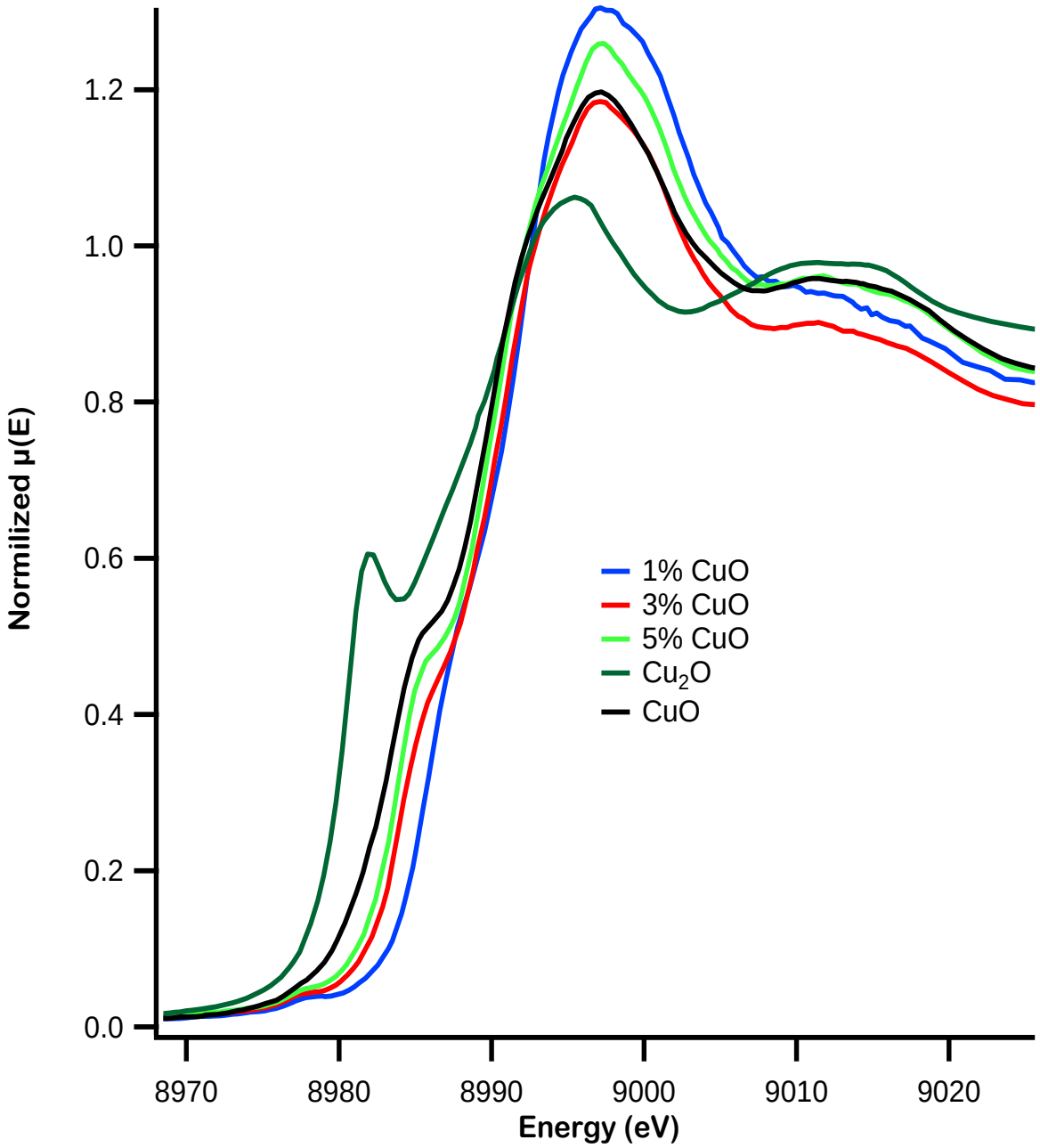

Figure 3.9 XANES spectra for the nanoparticles prepared at severely under doped condition (32:1) at different CuO coverage on fumed silica with copper oxide standards.

sample without changing the support substrate for nanoclusters prepared at the severely under doped conditions (32:1). Here, samples were prepared by selecting the percent coverage (w/w%) of copper oxide on supported fumed silica to be 1% , 3% and 5% sample.

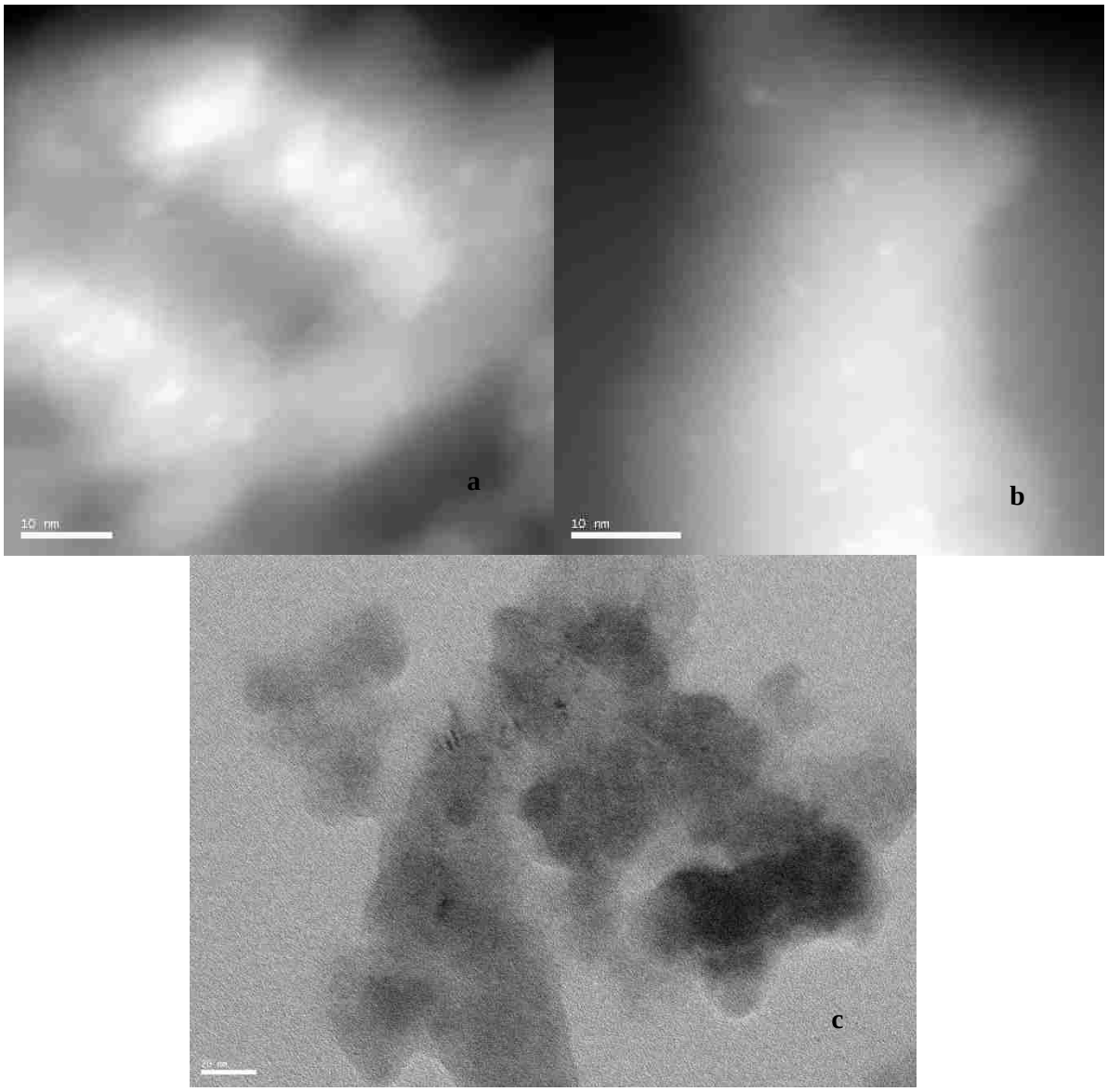

Figure 3.10 Microscopic imagers (a and b: High Angle Annular Dark Field TEM and c: High resolution TEM) of nanoparticles prepared at severely under doped condition (32:1) at different CuO coverage on fumed silica (a) 1% (b) 3% (C) 5%.

Here, we wanted to check whether the lower percentages like 3% or 1% of copper oxide could make smaller size nanoparticles on fumed silica substrate surfaces compared to bigger

nanoparticles found in the 5% condition. X-ray absorption spectroscopy and electron microscopy experiments were performed on the respective samples. Both XANES and Fourier transformed EXAFS showed differences compared to the 5% samples. XANES spectra in figure 3.8 indicate with the decrease of copper oxide coverage there was a disappearance of the shoulder characteristic for Cu (II), and the spectra became more like for the fully doped nanoparticles. This observation was well supported by TEM images. Figure 3.10 shows the formation of nanoparticles for 1% copper oxide containing samples prepared at severely under doped conditions.

3.5 Conclusions

Comparison of XANES spectra indicated all the copper ions in the nanoclusters corresponded to Cu^{+2} rather than Cu^{+1}, but the near edge absorption feature of the copper in the nanoparticles had shifted to a higher energy compared to bulk cupric oxide (CuO). EXAFS data showed a lack of long range order in the smaller nanoparticles, which indicated the presence of flatter and amorphous nanoparticles. TEM studies indicated nanoparticles prepared at fully (2:1), half (4:1) and quarter (8:1) doped conditions show a decreasing trend of their approximate particle size from 3.7 nm, 3.0 nm and 2.0 nm, respectively. Further, TEM images showed particles prepared at severely under doped conditions may have formed larger nanoparticles (~100 nm), and this information was consistent with the observed long range order in the EXAFS data. This work also suggested nanoparticles prepared at severely under doped conditions did form smaller size nanoparticles at lower percent coverage (1%-3%) of copper oxide on fumed silica.

3.6 References

(1) Sgro, L. A.; Basile, G.; Barone, A. C.; D'Anna, A.; Minutolo, P.; Borghese, A.; D'Alessio, A. *Chemosphere* **2003**, *51*, 1079.

(2) D'Alessio, A.; Barone, A. C.; Cau, R.; D'Anna, A.; Minutolo, P. *Proceedings of the Combustion Institute* **2005**, *30*, 2595.

(3) Kennedy, I. M. *Proceedings of the Combustion Institute* **2007**, *31*, 2757.

(4) Dockery, D. W.; Speizer, F. E.; Stram, D. O.; Ware, J. H.; Spengler, J. D.; Ferris, B. G. *Am. Rev. Respir. Dis.* **1989**, *139*, 587.

(5) Donaldson, K.; Li, X. Y.; MacNee, W. *Journal of Aerosol Science* **1998**, *29*, 553.

(6) Pope, C. A.; Dockery, D. W.; Spengler, J. D.; Raizenne, M. E. *American Journal of Respiratory and Critical Care Medicine* **1991**, *144*, 668.

(7) Tiede, K.; Boxall, A. B. A.; Tear, S. P.; Lewis, J.; David, H.; Hassellöv, M. *Food Additives & Contaminants: Part A* **2008**, *25*, 795.

(8) Teow, Y.; Asharani, P. V.; Hande, M. P.; Valiyaveettil, S. *Chemical Communications* **2011**, *47*, 7025.

(9) Costa, D. L.; Dreher, K. L. *Environmental Health Perspectives* **1997**, *105*, 1053.

(10) Seaton, A.; Macnee, W.; Donaldson, K.; Godden, D. *Lancet* **1995**, *345*, 176.

(11) Agius, R. *Lancet* **1995**, *345*, 799.

(12) Oskam, G. *J Sol-Gel Sci Techn* **2006**, *37*, 161.

(13) Aiken, J. D.; Finke, R. G. *Journal of Molecular Catalysis a-Chemical* **1999**, *145*, 1.

(14) Biswas, P.; Wu, C. Y. *Journal of the Air & Waste Management Association* **2005**, *55*, 708.

(15) Christian, P.; Von der Kammer, F.; Baalousha, M.; Hofmann, T. *Ecotoxicology* **2008**, *17*, 326.

(16) Kaden, W. E.; Wu, T. P.; Kunkel, W. A.; Anderson, S. L. *Science* **2009**, *326*, 826.

(17) Vajda, S.; Pellin, M. J.; Greeley, J. P.; Marshall, C. L.; Curtiss, L. A.; Ballentine, G. A.; Elam, J. W.; Catillon-Mucherie, S.; Redfern, P. C.; Mehmood, F.; Zapol, P. *Nature Materials* **2009**, *8*, 213.

(18) Hirano, S.; Nitta, H.; Moriguchi, Y.; Kobayashi, S.; Kondo, Y.; Tanabe, K.; Kobayashi, T.; Wakamatsu, S.; Morita, M.; Yamazaki, S. *Journal of Nanoparticle Research* **2003**, *5*, 311.

(19) Jimenez, I.; Arbiol, J.; Dezanneau, G.; Cornet, A.; Morante, J. R. *Sensors and Actuators B-Chemical* **2003**, *93*, 475.

(20) Floriano, P. N.; Noble, C. O.; Schoonmaker, J. M.; Poliakoff, E. D.; McCarley, R. L. *Journal of the American Chemical Society* **2001**, *123*, 10545.

(21) Linak, W. P.; Wendt, J. O. L. *Fuel Processing Technology* **1994**, *39*, 173.

(22) Domingos, R. F.; Baalousha, M. A.; Ju-Nam, Y.; Reid, M. M.; Tufenkji, N.; Lead, J. R.; Leppard, G. G.; Wilkinson, K. J. *Environmental Science & Technology* **2009**, *43*, 7277.

(23) Farmer, J. A.; Campbell, C. T. *Science*, *329*, 933.

(24) Alves, D.; Santos, C. G.; Paixao, M. W.; Soares, L. C.; de Souza, D.; Rodrigues, O. E. D.; Braga, A. L. *Tetrahedron Letters* **2009**, *50*, 6635.

(25) Cormier, S. A.; Lomnicki, S.; Backes, W.; Dellinger, B. *Environmental Health Perspectives* **2006**, *114*, 810.

(26) Khachatryan, L.; Vejerano, E.; Lomnicki, S.; Dellinger, B. *Environmental Science & Technology* **2011**, *45*, 8559.

(27) Lomnicki, S.; Truong, H.; Vejerano, E.; Dellinger, B. *Environmental Science & Technology* **2008**, *42*, 4982.

(28) Dellinger, B.; Pryor, W. A.; Cueto, R.; Squadrito, G. L.; Hegde, V.; Deutsch, W. A. *Chemical Research in Toxicology* **2001**, *14*, 1371.

(29) Truong, H.; Lomnicki, S.; Dellinger, B. *Chemosphere* **2008**, *71*, 107.

(30) Farquar, G. R.; Alderman, S. L.; Poliakoff, E. D.; Dellinger, B. *Environmental Science & Technology* **2003**, *37*, 931.

(31) Lomnicki, S. M.; Wu, H.; Osborne, S. N.; Pruett, J. M.; McCarley, R. L.; Poliakoff, E.; Dellinger, B. *Materials Science and Engineering: B* **2010**, *175*, 136.

(32) Mitran, E.; Dellinger, B.; McCarley, R. L. *Chem. Mater.* **2010**, *22*, 6555.

(33) Larsen, G.; Lotero, E.; Marquez, M. *Journal of Physical Chemistry B* **2000**, *104*, 4840.

(34) Larsen, G.; Noriega, S. *Applied Catalysis a-General* **2004**, *278*, 73.

(35) Velarde-Ortiz, R.; Larsen, G. *Chemistry of Materials* **2002**, *14*, 858.

(36) Rehr, J. J.; Mustre de Leon, J.; Zabinsky, S. I.; Albers, R. C. *Journal of the American Chemical Society* **1991**, *113*, 5135.

(37) Newville, M. *Journal of Synchrotron Radiation* **2001**, *8*, 96.

(38) Ravel, B.; Newville, M. *Physica Scripta* **2005**, *T115*, 1007.

(39) Ravel, B.; Newville, M. *Journal of Synchrotron Radiation* **2005**, *12*, 537.

(40) Stern, E. A. *Scientific American* **1976**, *234*, 96.

(41) Dooley, K. M.; Bhat, A. K.; Plaisance, C. P.; Roy, A. D. *Applied Catalysis A: General* **2007**, *320*, 122.

(42) Singh, V.; Palshin, V.; Tittsworth, R. C.; Meletis, E. I. *Carbon* **2006**, *44*, 1280.

(43) N.Gonzalez Pech; A. Barron **2011**.

(44) Kau, L. S.; Spirasolomon, D. J.; Pennerhahn, J. E.; Hodgson, K. O.; Solomon, E. I. *Journal of the American Chemical Society* **1987**, *109*, 6433.

(45) Henson, M. J.; Mukherjee, P.; Root, D. E.; Daniel, T.; Stack, P.; Solomon, E. I. *Abstracts of Papers of the American Chemical Society* **2000**, *219*, 85.

(46) DuBois, J. L.; Mukherjee, P.; Stack, T. D. P.; Hedman, B.; Solomon, E. I.; Hodgson, K. O. *Journal of the American Chemical Society* **2000**, *122*, 5775.

Chapter 4
Effect of Substrate on Formation of CuO Particles: How Cu Oxide Forms on Alumina

4.1 Introduction

An important aspect of this research was to see how the substrate affected the properties of nanoparticles formation. Specifically, we wanted to study the ability of copper oxide to form different size nanoparticles on a fumed alumina substrate surface. Motivation for this work came from our previous work in which we synthesized series of different size copper oxide nanoparticles on fumed silica and looked for a substrate dependency for the formation of copper oxide nanoparticles. Here, fumed alumina was used as the alternative substrate surface that would match the purpose of the overall project of formation of surrogates for fly ash.

Alumina (i.e γ -Al_2O_3) is used as one of the major support surfaces because of its unique mechanical and chemical properties [1-3]. Among γ-Al_2O_3 supported catalysts, CuO/γ-Al_2O_3 shows potential catalytic activity for NOx elimination and CO oxidation. Alumina supported copper oxide was also used as an alternative catalyst for lean-burn NOx removal instead of expensive precious metal supported catalysts [1,4]. Activity of CuO/γ-Al_2O_3 for CO oxidation was investigated by Park and Ledford, and results suggested the turnover frequency for CO oxidation would increase with the amount of CuO presence in the catalyst [5,6]. Although many studies have been conducted to check the catalytic activity of alumina supported metal and metal oxide catalytic systems, detailed studies on the structure and phase transition of copper-alumina during the preparation of supported surfaces at higher temperatures are rarely reported. Therefore, it is important to understand the structure of 5% copper oxide on fumed alumina during calcination. As in the studies of copper oxide nanoparticle formation on fumed silica, we applied X-ray

absorption and TEM methods to characterize the copper oxide particle formation on fumed alumina.

4.2 Background

CuO, cupric oxide, the simplest member of the copper compound family, has attracted particular attention due to its potentially useful physical properties and many diverse applications. Its ability to form various size particles (i.e. nanoparticles), availability as a cheaper substitute for commonly used expensive metals like silver, and capability of easily mixing with polymers without losing its physical or chemical stability, make CuO a useful candidate/raw material for many different industries such as high temperature semiconductors, sensors, catalysis, health (i.e. antimicrobial), energy conservation, and field emission emitters [7-9]. With the increased usage of CuO, it is significant to have CuO in many different forms (i.e. micron/nano-particles and fine particles) in the environment. These environmentally persistent CuO particles may be present in many different substrates and can be involved with different chemical reactions (i.e. surface mediated reactions).

Over the last decade, our group and collaborators have been working on surrogates for fly ash and have extensively studied the effect of formation of transition metal oxide (Cu, Ni and Fe) nanoclusters on fumed silica surfaces [10,11]. Fly ash is a complex heterogeneous mixture, which mostly (more than 90%) consists of SiO_2 and Al_2O_3 and also contains metal species. A significant fraction of the metals are present as fine particles (i.e., nanoparticles), including transition metals and their oxides that are generated during combustion processes, and as byproducts of the above mentioned technologies. These fine particles can be deposited on many different surfaces in the environment including abundant SiO_2 and Al_2O_3. Previously, fumed silica was selected because it has a high surface area (CAB-O-SIL, 380 m^2/g) and sites to form

nanoparticles. Since we haven't studied the nanoparticle formation on any other surface, there is a greater urgency to use some other substrates that are present in the fly ash and have high surface areas. It is important to understand the effect of substrate on nanoparticle formation and size distribution on different surfaces.

During the synthesis of such supported particles (transition metal/metal oxide catalytic nanoparticles), the substrate can interact both physically and chemically with the metal oxide particles [12]. The particle size can be controlled by using powdered, fumed or micro-porous solids as substrates. Since a central goal of our project is to elucidate the role of supported metal oxide nanoparticles on surface mediated reactions, such as the formation of harmful substances like furans and dioxins, it is important to understand the substrate effect on particle formation as well as the interactions of such metal oxide nanoparticles on substrate surfaces. Also, it is important to understand the interaction of supported transition metal nanoparticles (catalyst) and how this interaction may apply to transition metal oxide nanoparticles supported on porous fumed substances (fumed silica / fumed alumina).

Over the years, great attention has been paid to the interaction between the active component (metal and metal oxide nanoparticles) and the support due to their extensive uses in a variety of important industrial reactions (e.g., cracking, polymerization) [13]. Many studies have been carried out to explore how substrate/metal interactions affect the catalytic activity of metal nanoparticles on supported substrates (both fumed and powdered substrates of SiO_2, Al_2O_3 and TiO_2) [12,14,15]. It was found that physicochemical and catalytic properties of such systems would be greatly influenced by factors such as the amount of active component (percentage), promoter, temperature for calcination and precursor [1,16,17]. There are a few other issues which should be addressed to have a complete understanding of the interaction of supported metal nanoparticle

systems. These issues include how the method of preparation, chemical composition, crystallinity, pore size and phase of the substrate (whether the substrate is in fumed or powdered form) affect the interaction and catalytic activity of such systems [1,12].

According to the literature, there are two types of interaction which can happen between metal nanoparticles and support substrates, and such interactions may alter the catalytic activity of the nanoparticles [12,18,19]. Strong metal support interactions between catalytic nanoparticles and the support arise from partial reduction of the oxide of the metal cations by the donation of a partial negative charge to the metal nanoparticles from the support. Another type of interaction can arise from metal nanoparticles being exposed to anion sites on the support substrate via Lewis acid/base interactions. This behavior has been extensively studied by using different metal nanoparticle systems of Ru, Pt, Pd and some transition metals on Al_2O_3, Si_2O_3, TiO_2 and SiO_2. These studies have revealed transition metals like Ni show stronger metal support interactions on substrates like TiO_2 than on SiO_2 and Al_2O_3 [12,19].

4.3 Experimental Method

The procedures were similar to what has been described previously for the copper oxide nanoparticles supported on fumed silica in Chapter 3. A series of fumed alumina (surface area 100 m^2/g) supported copper oxide (5% w/w) samples were prepared using the dendrimeric method by varying the concentrations of the NH_2 groups of the dendrimer with respect to the copper ion concentration as described in the experimental section. Then, the experimental samples were prepared according to the DCM beamline requirements and data was collected in fluorescent mode (here, the sample was placed on the stage at a 45° angle to the incident X-ray beam). During the experiment parameters for the X-ray absorption measurements were selected to satisfy both the XANES and EXAFS regions of the spectra. Data were collected with the 13

element germanium detector and all the data were collected at the Cu K-edge. ATHENA and ARTEMIS programs were used respectively to process and analyze the beamline data. TEM and SEM images for these samples were taken at the CMRF (at the University of Iowa) to confirm the findings from X-ray absorption spectroscopy.

4.4 Results and Discussion

Figure 4.1 shows the XANES region of the X-ray absorption spectra for the fumed alumina supported 5% copper oxide samples prepared under all the doping conditions compared with the two copper oxide, cupric oxide (CuO) and cuprous oxide (Cu_2O), standards. The spectra indicate the copper K-edge for the samples (prepared at different doping ratios) have shifted to a higher energy with respect to both the copper oxide standards, and there was no edge shift observed among the samples. These observations suggested the copper species present in the fumed alumina support surface were more like Cu^{+2} than Cu^{+1} and the copper species present in all the samples possessed the same oxidation state.

XANES spectra for the samples showed the appearance of a pre-edge absorption feature at around 8978 eV due to the dipole forbidden 1s → 3d transition and the disappearance of the shoulder characteristic for the Cu(II) compounds. These pre-edge structures are commonly observed for every first row transition metal in the periodic table which does not have fully occupied 3d orbitals. Although the 1s to 3d transition is forbidden by dipole selection rules, these transitions can be observed due to 3d to 4p orbital mixing as well as direct quadrupolar coupling [20-22]. The feature which disappeared from the sample spectra compared to the Cu (II) standard corresponded to 1s → 4p excitations combined with strong ligand to metal charge transfer, or shake down effect.

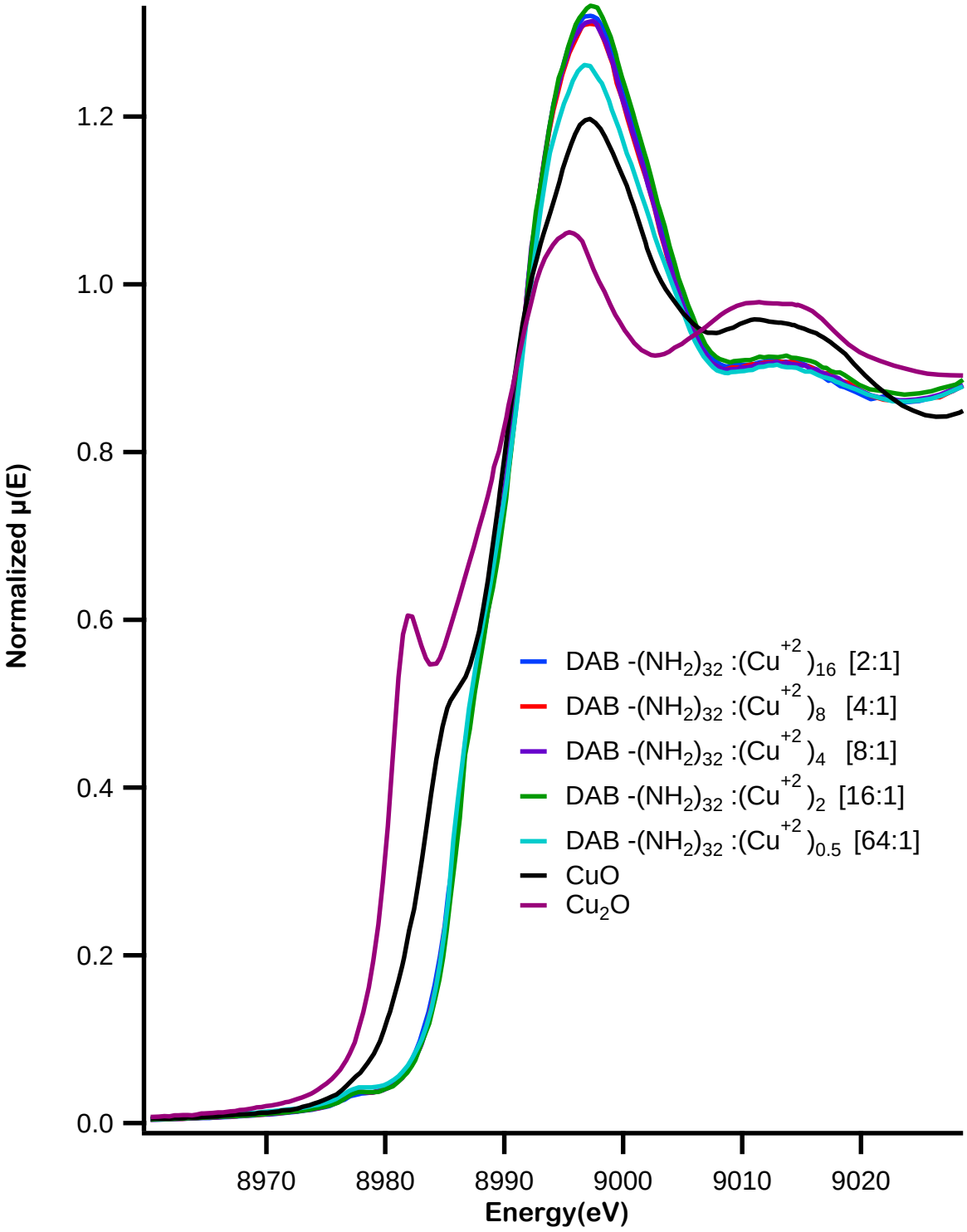

Figure 4.1 XANES spectra for copper oxide particles supported on fumed alumina prepared at fully doped (2:1), half doped (4:1), quarter doped (8:1), 1/8 doped (16:1) and severely underdoped (64:1) conditions with both copper oxide (Cu_2O and CuO) standards at Cu K-edge.

The trends of the appearance of the 1s to 3d transition and the disappearance of the shoulder structure can be utilized as a tool to probe the molecular geometric properties of the absorption sites. It was reported that a distortion of the geometry of the absorption site can result in an increase in the 1s → 3d transitions as well as the shake down effect [21,22].

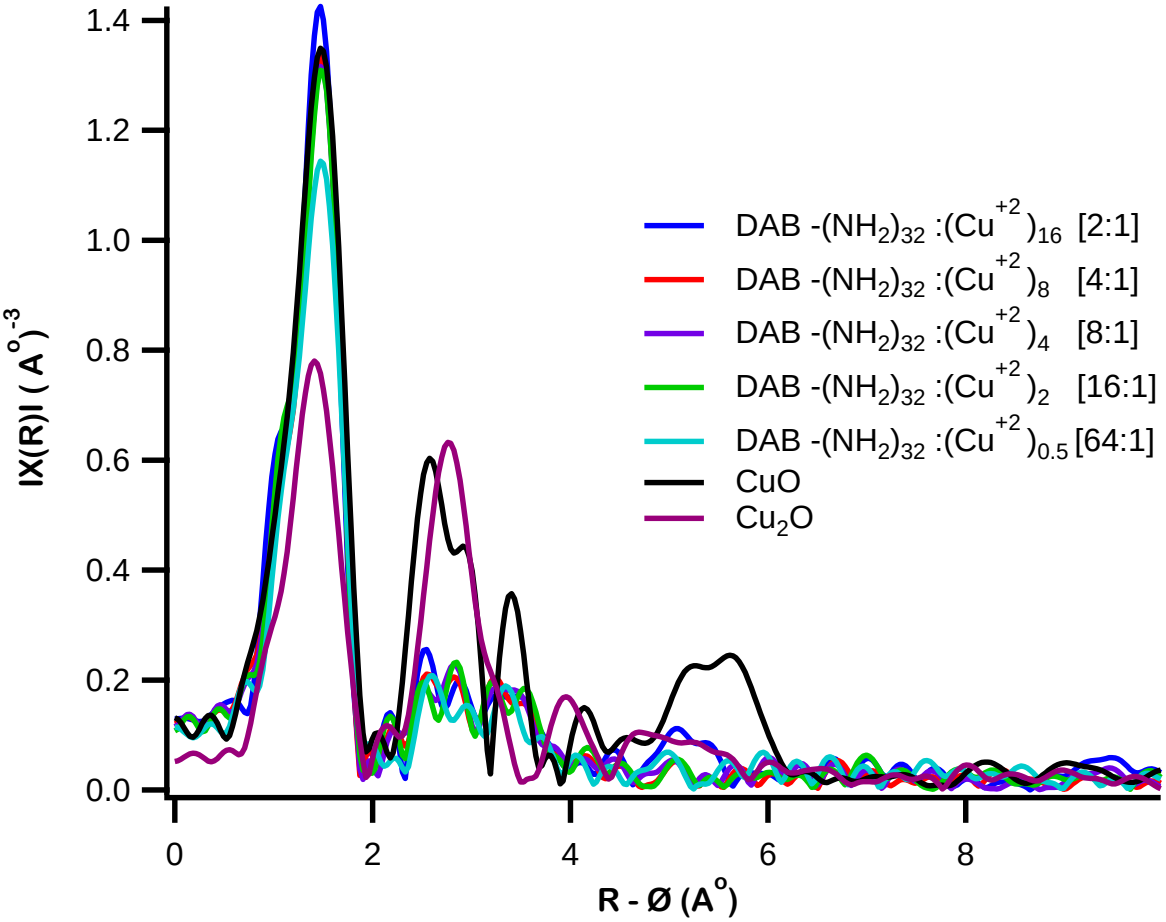

Figure 4.2 Radial distribution function for EXAFS data for copper oxide particles supported on fumed alumina prepared at fully doped (2:1), half doped (4:1), quarter doped (8:1), 1/8 doped (16:1) and severely underdoped (64 :1) conditions with both copper oxide (Cu_2O and CuO) standards.

Fourier transformed EXAFS data at the Cu K-edge were used to obtain the radial distribution function (R-space data) data for fumed alumina supported copper oxide species. During the data analysis, the range for the k-space data was selected from 2-12 cm^{-1} and a Kaiser-Bessel window [23] was used as the analysis window. As in the Figure 4.2, R-space data

indicated the presence of an intense first shell peak around 1.9 Å for all the samples. Even though there were no significant other peaks due to scattering from neighboring atoms as intense as the first peak there were a few very low intensity peaks (slightly higher than the background) present between 2-4 Å. Comparison of corresponding RDF's with the copper oxide standards suggested the RDFs for the samples do not have contributions from single or multiple scattering due to Cu-Cu or Cu-O-Cu bonding structure. Therefore, we assumed the Cu species present in the fumed alumina support surface were in highly oxidized form (Cu^{+2}) and had to be attached to oxygen attached to the alumina surface or present as CuO directly attached to the positively charged fumed alumina surface. This stands in stark contrast to the result obtained using silica as a support.

Several groups have identified the incorporation of copper into alumina forms the copper aluminate ($CuAl_2O_4$) spinel phase [6,24-26], and $CuAl_2O_4$ exists only as a surface species [24,26,27]. Formation of surface $CuAl_2O_4$ can result in the presence of Cu^{+2} species [26-28] in starting materials or any intermediates. Copper-modified alumina catalysts by M. Ozawa et al. have been investigated from the viewpoint of the structural phase transition and thermal stability (designed for NO removal under lean-burn engine conditions). For the as-prepared materials, powder-diffraction patterns revealed a mixture of crystalline γ-Al_2O_3 and CuO, and electron spin resonance (ESR) data showed well-dispersed Cu^{+2} cations coordinated by O atoms in open-octahedron geometry. Also, their neutron diffraction measurements confirmed the elimination of the CuO phase above 800^oC [4]. This is a very important observation since the initial heat treatment of (500^oC) their experiment is really close to our calcination temperature of 450^oC and mimics the same experimental conditions even though γ-Al_2O_3 used in their experiment has a surface area slightly larger than the surface area of the fumed alumina used by us. Therefore, it is

fair to use their experimental findings to interpret our observations related to the geometry and the interactions present in our system. In another study, where copper oxide (CuO_x) catalysts were dispersed on SiO_2−Al_2O_3 support, researchers found that copper species were uniformly spread on the SiO_2−Al_2O_3 support as small aggregates in both high and low copper containing samples [29].

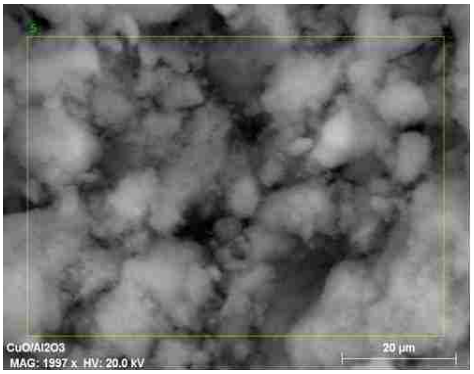

Spectrum: 5

El	AN	Series	unn. C [wt.%]	norm. C [wt.%]	Atom. C [at.%]	Error [wt.%]
O	8	K-series	48.35	46.92	60.79	5.9
Al	13	K-series	51.05	49.54	38.06	2.5
Cu	29	K-series	3.64	3.54	1.15	0.2
		Total:	103.05	100.00	100.00	

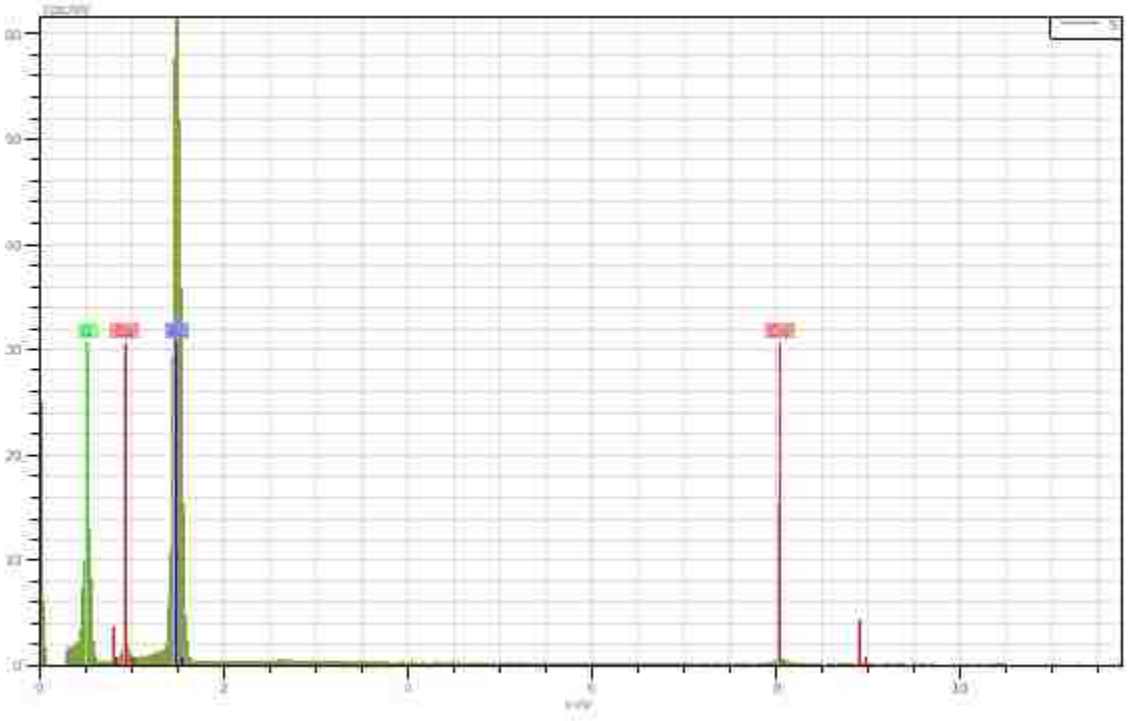

Figure 4.3 SEM image of CuO particles supported on fumed alumina prepared at fully doped conditions (molar ratio of NH_2-groups of the dendrimer (DAB-G4) to Cu^{+2} maintained at 2:1).

It was also reported that increasing the copper content can limit the mobility of the CuO_x species. However, their spectroscopic evidence agreed with previously reported observations of Cu^{+2} ions present in an axially distorted octahedral environment of an O-containing ligand and, at high copper loading, the existence of copper centers in closer interaction via formation of oxocation-like structures [29].

Spectrum: 20

El	AN	Series	unn. C [wt.%]	norm. C [wt.%]	Atom. C [at.%]	Error [wt.%]
O	8	K-series	44.42	43.24	57.30	6.0
Al	13	K-series	53.98	52.54	41.29	2.6
Cu	29	K-series	4.34	4.22	1.41	0.2
		Total:	102.74	100.00	100.00	

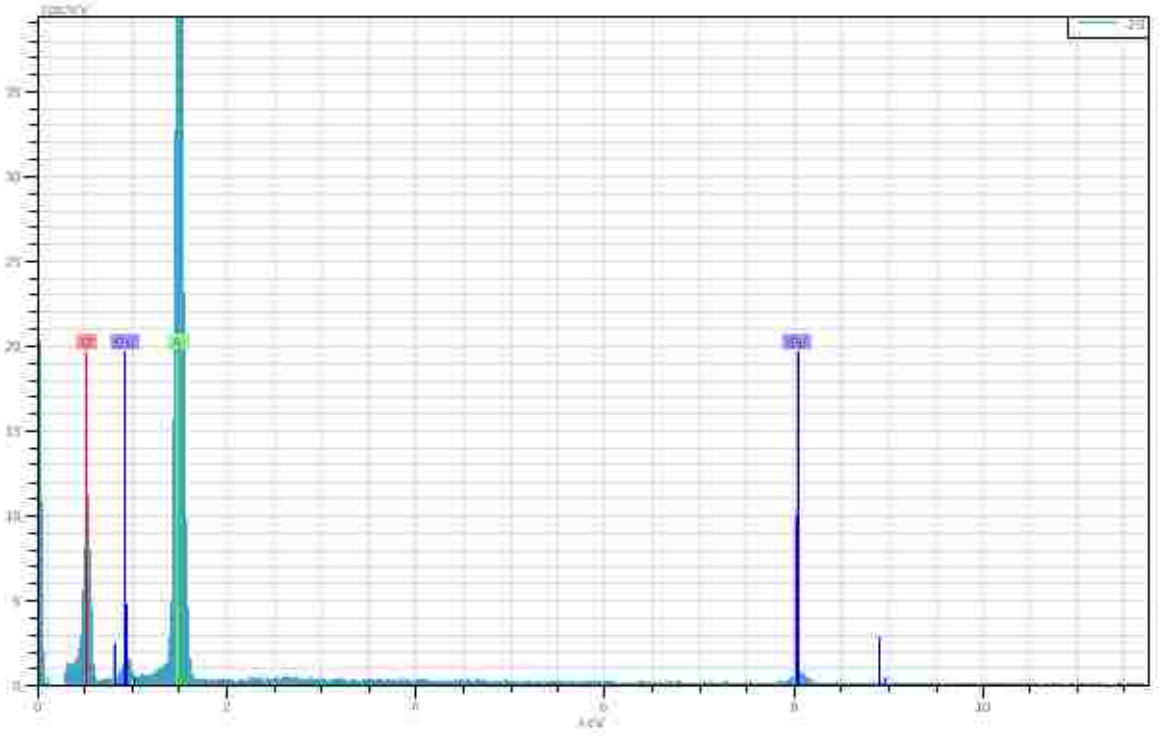

Figure 4.4 SEM image of CuO particles supported on fumed alumina prepared at severely under doped conditions (molar ratio of NH_2-groups of the dendrimer (DAB-G4) to Cu^{+2} maintained at 64:1)

To confirm the X-ray absorption spectroscopic observations, a set of microscopy experiments were conducted at the University of Iowa's CMRF. Both TEM and SEM images were taken at different magnifications for oxidized copper species on fumed alumina support surfaces prepared under extreme doping conditions.

Spectrum: 7

El	AN	Series	unn. C [wt.%]	norm. C [wt.%]	Atom. C [at.%]	Error [wt.%]
O	8	K-series	47.09	54.25	69.09	5.9
Si	14	K-series	34.81	40.10	29.09	1.5
Cu	29	K-series	4.91	5.65	1.81	0.2
		Total:	86.81	100.00	100.00	

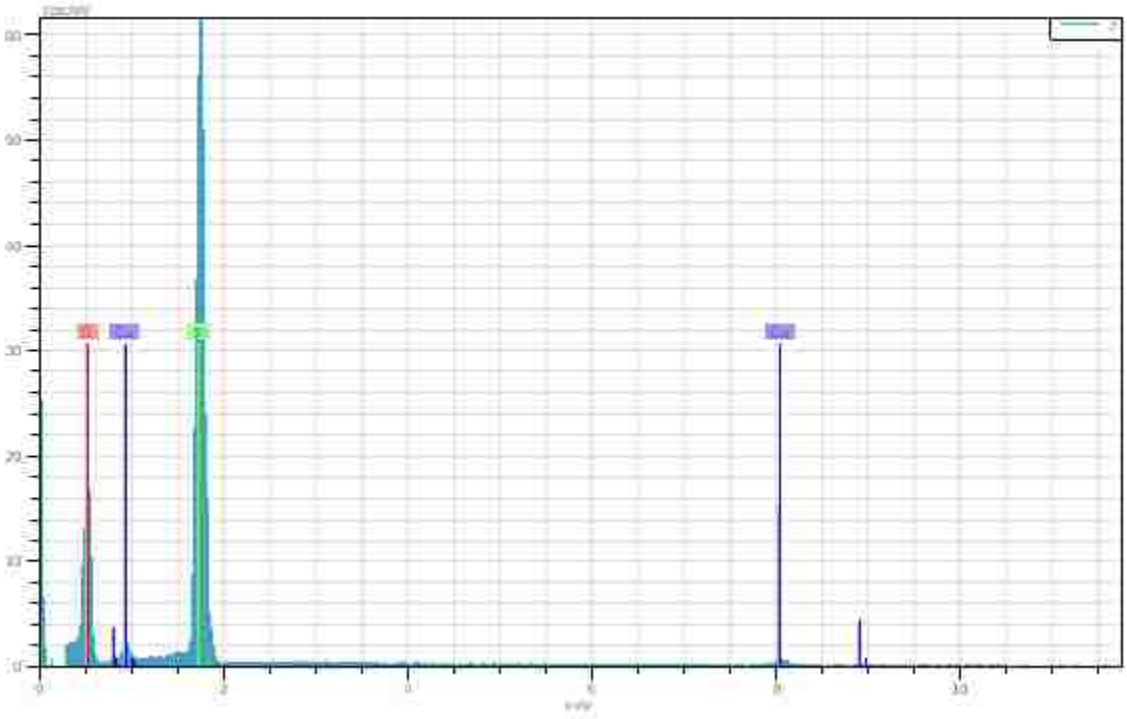

Figure 4.5 SEM image of CuO particles supported on fumed silica prepared at fully doped conditions (molar ratio of NH_2-groups of the dendrimer (DAB-G4) to Cu^{+2} maintained at 2:1)

Figures 4.3 and 4.4 show the SEM images of dendrimerically prepared oxidized copper species at fully doped (2:1) and extremely under doped conditions, respectively. TEM and SEM images confirmed that no nanometer size particles formed on fumed alumina for 5% CuO samples like copper oxide nanoparticles formed on the fumed silica support surface (figure 4.5). However, SEM data suggested the presence of copper on the fumed alumina surface, but the copper was not in the form of nanometer size particles.

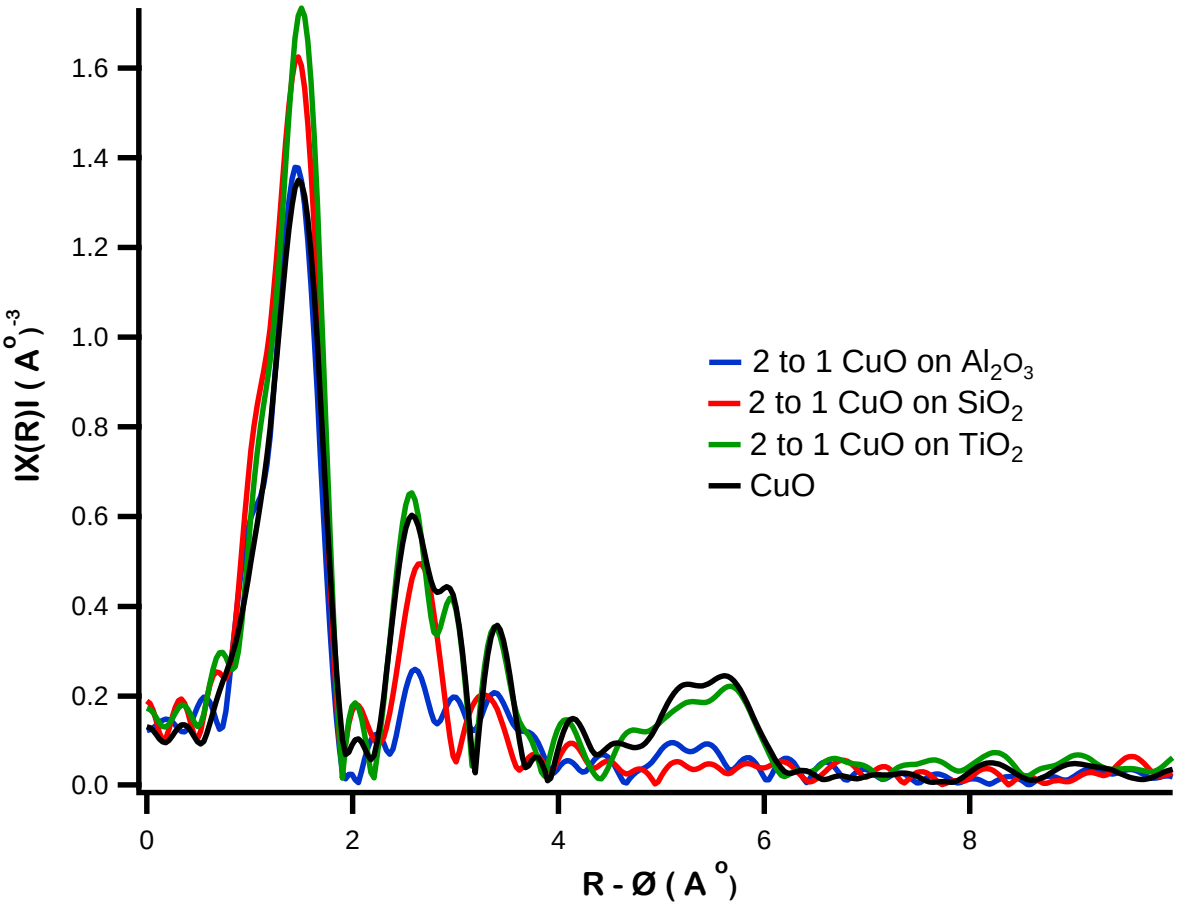

Figure 4.6 Radial distribution functions of copper oxide particles (prepared at fully doped conditions with the dendrimer) on different support substrate surfaces with CuO standard.

As mentioned earlier, there are a few literature reports indicate that the bonding between copper and alumina happens via an oxocation-like connection in the presence of high percentage of copper on alumina support surfaces [4,29]. Since 5% copper oxide concentration, which we used

during our preparation, is a high concentration than found for typical environmental samples, we suspected the same scenario could apply in our case, and the copper may have bonded to cationic fumed alumina via oxocation-like interaction.

To understand the substrate effect on particle formation, another experiment was performed by changing the support substrate without changing the percentage of copper oxide (5%) in the sample. This experiment was used to confirm the presence of substrate effect on particle formation. Here, Anatase grade titanium dioxide (TiO_2) was selected as the support substrate surface and an identical dendrimeric method was used for the sample preparation. TEM and SEM images showed the presence of copper oxide nanoparticles on TiO_2 support surface. R-space X-ray absorption data showed the copper oxide nanoparticles formed on TiO_2 support had relatively large long range order compared to copper oxide particles and nanoparticles found on fumed alumina and fumed silica support substrates. Even though it has been found that copper oxide forms nanoparticles on TiO_2 surfaces, these nanoparticles possessed fairly similar R-space spectra to cupric oxide (CuO) standard. This suggested that these nanoparticles were somewhat bigger than the nanoparticles formed on silica substrate using identical preparation conditions.

4.5 Conclusions

After X-ray absorption spectroscopic observations for fumed silica supported CuO showed the presence of CuO nanoparticles, we wanted to perform an identical set of experiments by changing the support substrate to identify whether there is an effect of the substrate in particle formation. Here, fumed alumina was selected as the support substrate and identical preparation conditions were used to understand the dependency of copper oxide particle formation on different porous surfaces. The XANES region of the X-ray absorption spectra for all the samples

showed a shift in their absorption edge (Cu K-edge) towards higher energy compared to copper oxide standards, but there were no edge shifts observed among the sample spectra. Unlike in copper oxide on fumed silica, radial distribution functions for copper oxide species on fumed alumina did not show long range order for any of the samples beyond the first shell (i.e., that corresponding to an oxygen attached to the copper atom. Microscopic images of both TEM and SEM did not show formation of copper oxide nanoparticles, even though SEM confirms the presence of copper on the fumed alumina surface. Spectroscopic observations and literature suggested copper species present in the fumed alumina support consisted of Cu^{+2} ions which may have been bonded to the cationic surface via oxygen forming oxocation-like structure. Therefore, we can speculate copper species found on the support may have formed Cu-Oxygen (CuO^{+}) sites on the fumed alumina surface instead of forming CuO nanoparticles. Also, the observation of nanoparticles for dendrimerically prepared copper oxide on anatase grade TiO_2 has confirmed that the dendrimeric formation of copper oxide nanoparticles on support surfaces depends highly upon the selected support substrate.

4.6 References

(1) Wang, Z.; Wan, H.; Liu, B.; Zhao, X.; Li, X.; Zhu, H.; Xu, X.; Ji, F.; Sun, K.; Dong, L.; Chen, Y. *Journal of Colloid and Interface Science* **2008**, *320*, 520.

(2) Hillerova, E.; Vit, Z.; Zdrazil, M. *Appl Catal a-Gen* **1994**, *118*, 111.

(3) Stará, I.; Zeze, D.; Matolín, V.; Pavluch, J.; Gruzza, B. *Applied Surface Science* **1997**, *115*, 46.

(4) Ozawa, M.; Suzuki, S.; Loong, C. K.; Richardson, J. W.; Thomas, R. R. *Applied Surface Science* **1997**, *121*, 441.

(5) Park, P. W.; Ledford, J. S. *Catal Lett* **1998**, *50*, 41.

(6) Park, P. W.; Ledford, J. S. *Applied Catalysis B: Environmental* **1998**, *15*, 221.

(7) Cava, R. J. *Science* **1990**, *247*, 656.

(8) Pandey, P.; Merwyn, S.; Agarwal, G.; Tripathi, B.; Pant, S. *Journal of Nanoparticle Research* **2012**, *14*, 1.

(9) Ren, G.; Hu, D.; Cheng, E. W. C.; Vargas-Reus, M. A.; Reip, P.; Allaker, R. P. *International Journal of Antimicrobial Agents* **2009**, *33*, 587.

(10) Mitran, E.; Dellinger, B.; McCarley, R. L. *Chem. Mater.* **2010**, *22*, 6555.

(11) Lomnicki, S. M.; Wu, H.; Osborne, S. N.; Pruett, J. M.; McCarley, R. L.; Poliakoff, E.; Dellinger, B. *Materials Science and Engineering: B* **2010**, *175*, 136.

(12) Vander Wal, R. L.; Ticich, T. M.; Curtis, V. E. *Carbon* **2001**, *39*, 2277.

(13) Rodríguez-Ramos, I.; Guerrero-Ruiz, A.; Homs, N.; de la Piscina, P. R.; Fierro, J. L. G. *Journal of Molecular Catalysis A: Chemical* **1995**, *95*, 147.

(14) Vuurman, M. A.; Wachs, I. E.; Stufkens, D. J.; Oskam, A. *Journal of Molecular Catalysis* **1993**, *80*, 209.

(15) Zheng, N.; Stucky, G. D. *Journal of the American Chemical Society* **2006**, *128*, 14278.

(16) Arena, F.; Horrell, B. A.; Cocke, D. L.; Parmaliana, A.; Giordano, N. *Journal of Catalysis* **1991**, *132*, 58.

(17) Radwan, N. R. E.; El-Sharkawy, E. A.; Youssef, A. M. *Applied Catalysis A: General* **2005**, *281*, 93.

(18) Moreno, F.; García-Cámara, B.; Saiz, J. M.; González, F. *Opt. Express* **2008**, *16*, 12487.

(19) Heiz, U.; Vanolli, F.; Sanchez, A.; Schneider, W. D. *Journal of the American Chemical Society* **1998**, *120*, 9668.

(20) Bair, R. A.; Goddard, W. A. *Phys Rev B* **1980**, *22*, 2767.

(21) Kau, L. S.; Spirasolomon, D. J.; Pennerhahn, J. E.; Hodgson, K. O.; Solomon, E. I. *Journal of the American Chemical Society* **1987**, *109*, 6433.

(22) Kau, L. S.; Hodgson, K. O.; Solomon, E. I. *Journal of the American Chemical Society* **1989**, *111*, 7103.

(23) Antoniak, C. *Beilstein journal of nanotechnology* **2011**, *2*, 237.

(24) Strohmeier, B. R.; Levden, D. E.; Field, R. S.; Hercules, D. M. *Journal of Catalysis* **1985**, *94*, 514.

(25) Centi, G.; Perathoner, S.; Biglino, D.; Giamello, E. *Journal of Catalysis* **1995**, *152*, 75.

(26) Larsson, P. O.; Andersson, A. *Appl Catal B-Environ* **2000**, *24*, 175.

(27) Friedman, R. M.; Freeman, J. J.; Lytle, F. W. *Journal of Catalysis* **1978**, *55*, 10.

(28) Park, P. W.; Ledford, J. S. *Appl Catal B-Environ* **1998**, *15*, 221.

(29) Bennici, S.; Gervasini, A.; Ravasio, N.; Zaccheria, F. *The Journal of Physical Chemistry B* **2003**, *107*, 5168.

Chapter 5
Cu/Ni Oxide Bimetallic Nanoparticles

5.1 Introduction

Bimetallic nanoparticles, synthesized by combining two metals, display superior chemical reactivity and selectivity compared to monometallic nanoparticles [1,2]. This gives bimetallic nanoparticles potential for a wide range of applications. In fact, bimetallic nanoparticles have become a key component in many optical, catalytic, materials manufacturing and magnetic devices [3]. Properties of such multicomponent nanoparticle systems can be tailored by controlling their composition, shape, [4-6] and architecture [6,7]. In this chapter, I describe my effort to synthesize and characterize bimetallic oxide catalysts composed of Cu and Ni.

Characterization and determination of physical and chemical properties of materials are two of the most common routines in chemistry. Nanoparticles are analyzed in terms of atoms and in the size range of a billionth of a meter. It is a huge challenge to work with such small particles with the available existing technologies, since most of them are inadequate to access some of a material's properties [6]. Also, it is critical to understand and identify the properties of nanoscale materials, since changes in the atomic structure of such nanoparticles can alter their chemical behavior. Emergent properties with the reduction of nanoparticle size and the ability to modify the shape and structure at the atomic level make these nanoparticles an important component of many different research fields. Therefore, it is important to establish a relationship between nanoparticles and their physicochemical properties in order to utilize them according with their applicability.

The majority of catalysts that consist of bimetallic nanoparticles are prepared by impregnation and/or deposition methods that often give highly active, well-dispersed systems, but ascertaining details about the composition, as well as the local structure of these nanoparticles is difficult and

often these properties remain ill-defined [6,8,9]. Heterogeneous catalysts consist of oxide supported bimetallic nanoparticles typically in the size range [2] of 1-10 nm. Bryan Eichhorn, at al. [6,10] showed bimetallic particles of the same composition, size, and shape show significant differences in activities when they are configured into different architectures, such as core shell, alloy, or monometallic mixtures.

Figure 5.1 Different architectures of bimetallic nanoparticle (a) core shell (b) alloy (c) monometallic mixtures [6,10].

The ability to tune the activity of the shell metal through interactions with the core has led to the emergence of the core shell structure as an attractive catalytic architecture [3,6,10-12]. However, control of particle's activity for a rational design requires precise synthetic methodology and full knowledge of structure/composition. Bimetallic nanoparticles with the same composition, shape, and crystal structure can have different architectures. Shape, structure[6], composition, [13] and architecture [6,10,14] are extremely important parameters affecting catalytic activities of bimetallic nanostructured materials, and knowledge of these parameters is critical in understanding the underlying surface science and catalytic chemistry. Also, it is known that introduction of another metal ion into a monometallic nanoparticle system can change the properties of the overall system. Such properties (i.e. catalytic) of the system could be manipulated (either increased or decreased) by changing the composition of the individual metal ions.

Over the years, most of the structural and compositional information has been gleaned from TEM, XRD and XPS techniques. These traditional techniques are more than adequate for the analysis of lager size (>10 nm) nanoparticles [6], but obtaining information for smaller size particles (<5.0 nm) remains quite challenging. Recently, it was found that X-ray related techniques such as X-ray absorption spectroscopy (XAS), XRD and FE-TEM with XDS are a few techniques that can be used for structural analysis of nanoparticles and also for comparative studies to provide information to construct a detailed picture of the nanostructures [15,16].

5.2 Why Cu/Ni oxide bimetallic nanoparticles?

Not only the properties but also the potential applications of both CuO and NiO nanoparticles have attracted extensive interest in many different fields of science and technology. For example, their catalytic properties of these types of nanoparticles are interesting for many processes [1,13,17]. Over the last decade our group and collaborators have studied CuO and NiO bulk material and individual nanoparticle systems on inert oxide surfaces (e.g., fumed silica) as surrogates for fly ash. Our collaborators have studied how these metal oxide particles promote the formation of environmentally persistent free radicals (EPFR's)[18,19] as well as their contribution to surface mediated reactions [18,20]. Most of our studies were based on size controlled CuO nanoparticles.

The goal of this project was to ascertain the structure and oxidation state information for the metals present in oxidized bimetallic nanoparticles. Such transition metal oxide nanoparticles are of interest because they are likely to be present in the emissions from combustion sources. Since naturally occurring nanoparticles are a complex mixture, here again we use a dendrimeric method to generate metal oxide nanoparticles as a means of controlling the size distribution in a systematic manner. It is possible to manipulate the nanocluster size, typically by varying the

concentration ratio of the number of amine groups of the dendrimer with respect to the total metal ion concentration.

5.3 Sample Preparation

Bimetallic nanoparticles were prepared by mixing copper (II) nitrate and nickel (II) nitrate at various concentrations with generation three (G-3) DAB-Am_{16} dendrimer in methanol. The molar ratio between the number of NH_2 groups of the dendrimer and metal ions was kept at 2:1 throughout the preparation. The dendrimer-metal ion complex was impregnated onto the fumed silica surface and the nanoparticle samples were prepared as described in the experimental section. X-ray absorption experiments were performed at CAMD's DCM beamline at the respective K-edges of the bimetallic nanoparticles. TEM and SEM images and energy dispersive X-ray analysis (EDS spectra) were taken at the CMRF at the University of Iowa.

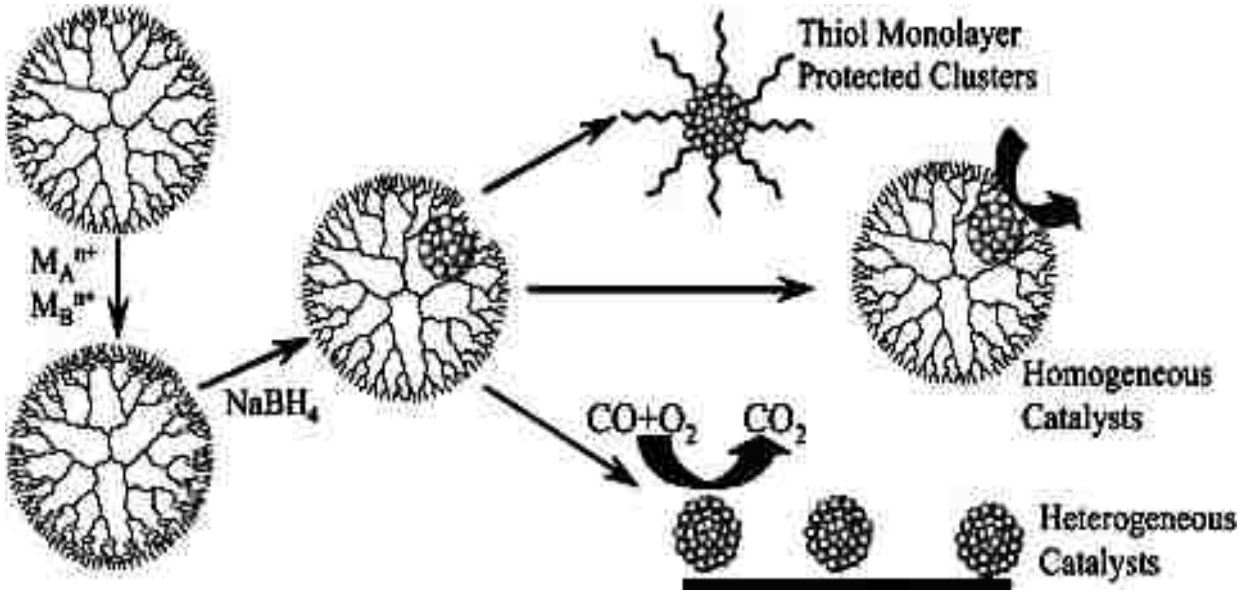

Figure 5.2 Schematic diagram of dendrimeric (PAMAM) preparation bimetallic nanoparticles [21].

5.4 Results and Discussion

5.4.1 EXAFS Data

X-ray absorption data were collected at the respective K-edges of the mixed metal oxide nanoclusters with different ratios of Cu to Ni. EXAFS data were used to acquire k-space data, and radial distribution functions (R-space data) were obtained by Fourier transforming the k-space data, as described in previous chapters.

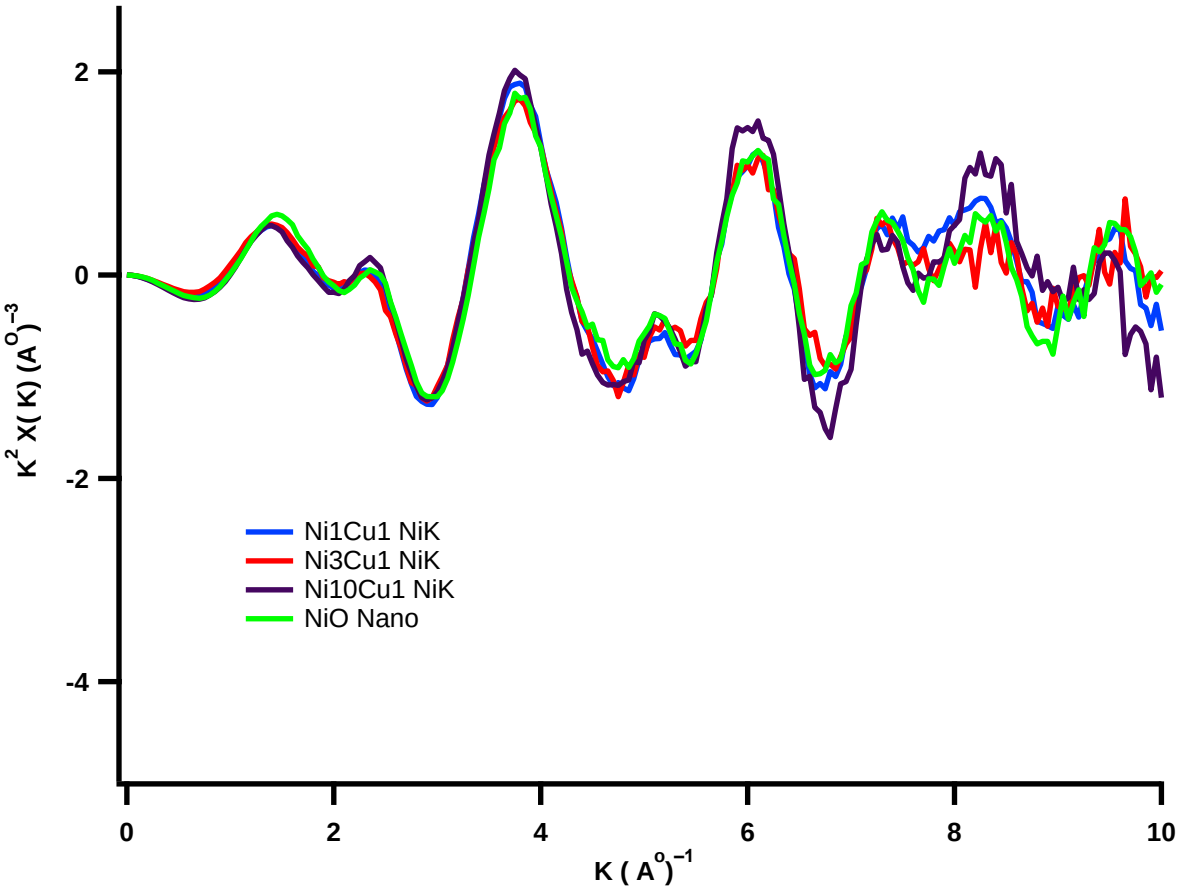

Figure 5.3 k-space data (spectra) for bimetallic nanoclusters and NiO nanoclusters at Ni K-edge.

Then k-space and R-space data for the mixed metal oxide or bimetallic oxide nanoclusters were compared to the respective metal oxide standards and the individual monometallic oxide, both CuO and NiO, nanoclusters at their respective K-edges. The k-space

data for the bimetallic nanoclusters at the Ni K-edge possessed a perfect similarity to the respective metal oxide nanoclusters up to a K value of six. However, at higher K values, samples that contained a higher amount of Ni (with respect to Cu) tended to show very high noise, as in figure 4.3 Both of these observations were not only true for Ni K-edge data but also true for k-space data at Cu K-edge for the nanocluster samples with higher copper percentages (figure 5.4). However, even with higher noise at a higher k value, the k-space spectra showed very good agreement with each other. As marked in figure 5.5, there was a slight difference in k-space data for the samples which contained a higher amount of Ni (Cu1Ni3 & Cu1Ni10) compared to the k-space spectra of cupric oxide (CuO) standard and CuO nanoparticles (prepared by the same method) at the Cu K-edge.

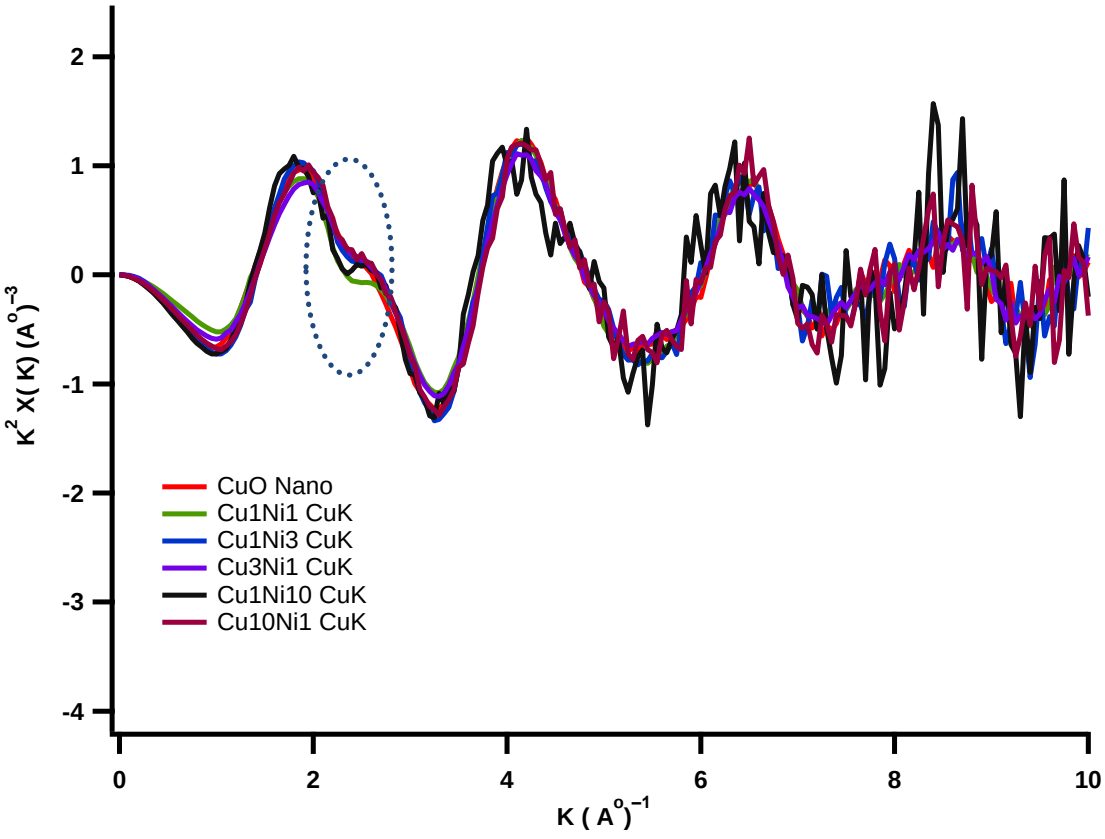

Figure 5.4 k-space data for all the bimetallic nanoclusters and CuO nanoclusters at Cu K-edge.

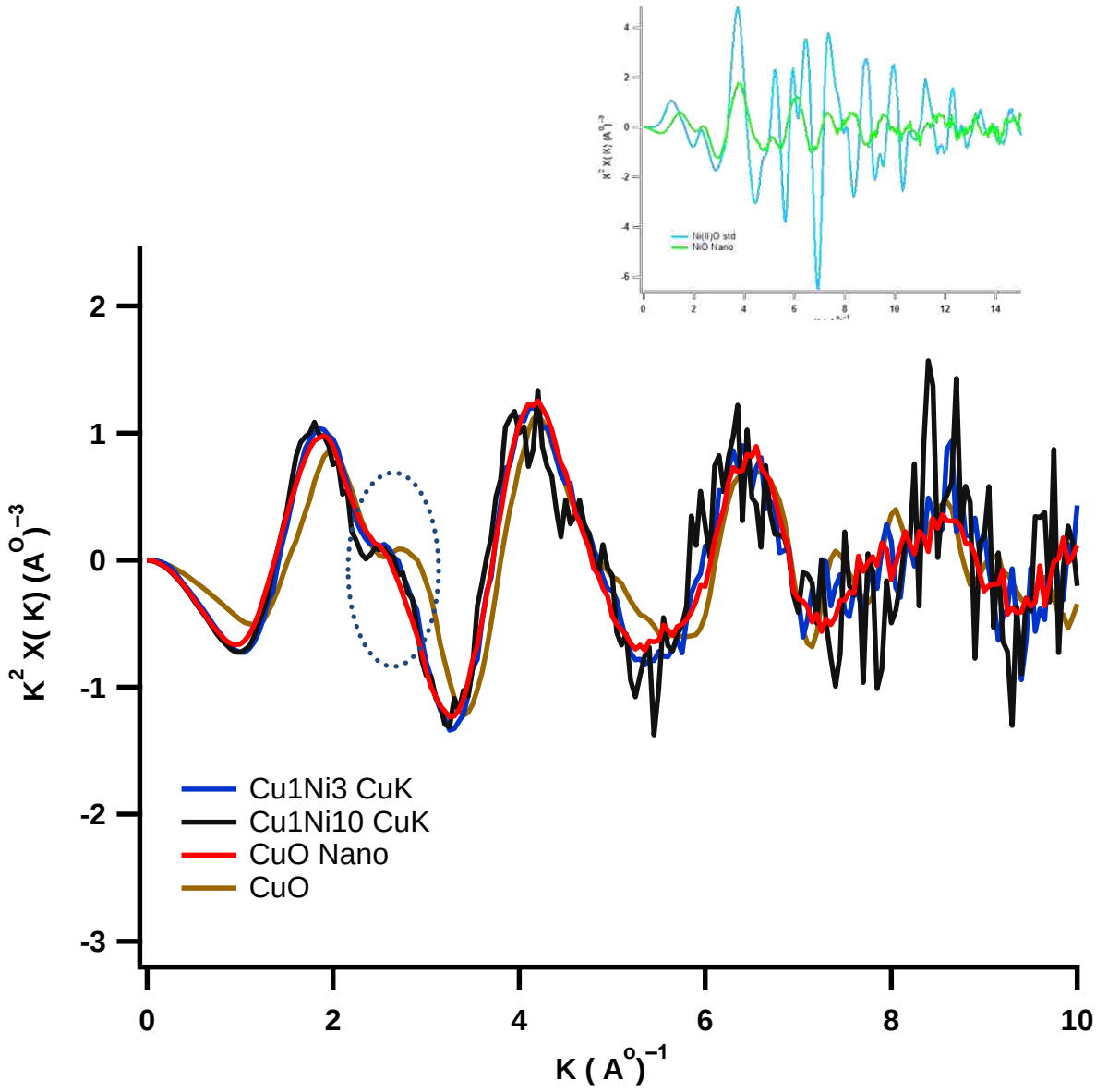

Figure 5.5 k-space data for highest amount of Ni containing bimetallic nanoclusters and CuO nanoclusters at Cu K-edge with CuO standard; Insert: Comparison of k-space data for NiO nanoclusters and NiO Standard.

The k-space data of the fully doped metal oxide nanoclusters and the corresponding metal oxide standards were not perfectly alike, but they did have fairly good agreement with each other (Figure 5.5). This observation should be obvious since we were comparing bulk metal oxide standards to dendrimerically prepared metal oxide nanoparticles.

5.4.2 R Space Data for mixed metal oxide at their respective K edges

Fourier transformed EXAFS data was used to obtain the R-space data. These R-space data (radial distribution functions) for the bimetallic nanoclusters were plotted at their respective K-edges. These radial distribution functions (RDF's) were compared with the fully doped metal oxide nanoclusters and their respective metal oxide standards. All these RDF's for mixed metal oxide nanoclusters at Cu K-edge are shown in Fig. 5.6 below. They are plotted without doing the correction for the phase shift.

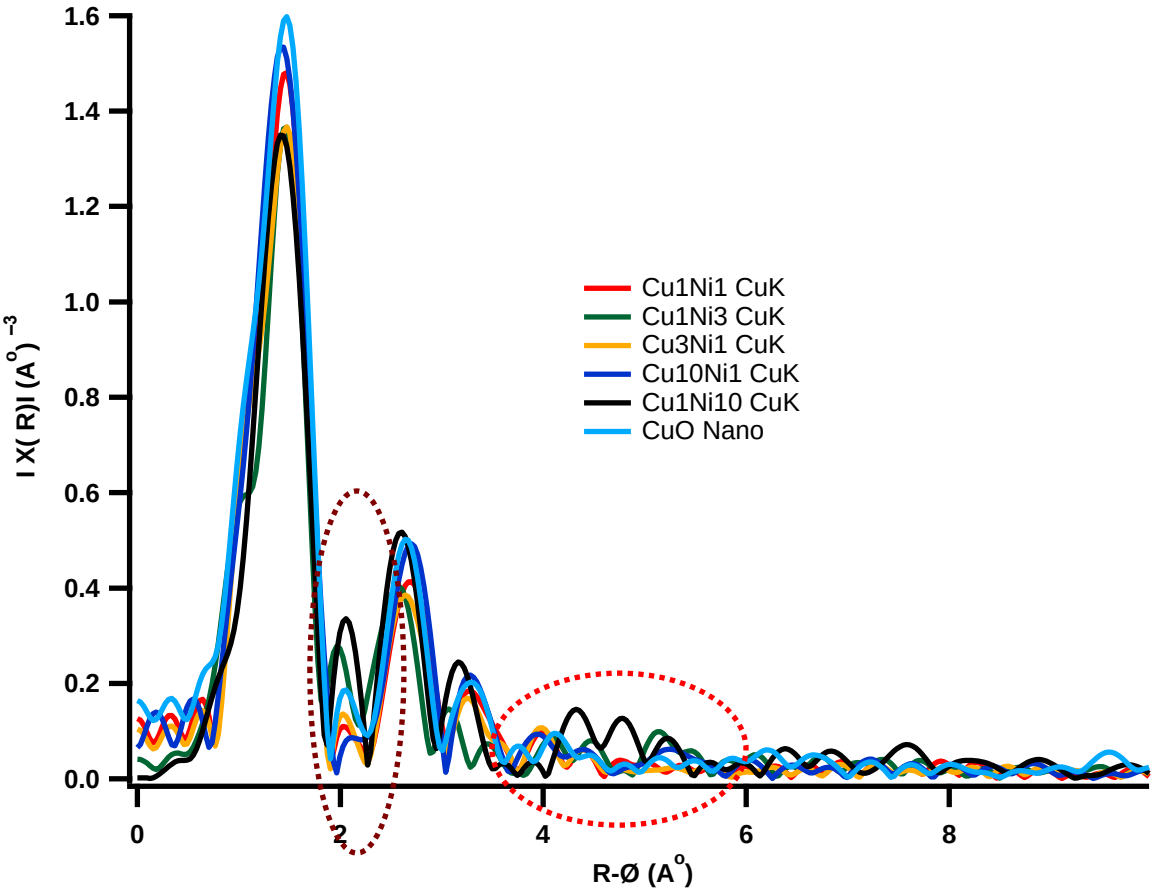

Figure 5.6 Radial distribution functions (R-space spectra) for bimetallic nanoclusters and CuO nanoclusters at Cu K-edge.

Quantitative analysis of the RDF spectra can provide information about the coordination number of the element around the target element and bond length or distance of the scattering

atoms from the central atom (most accurate up to 6 Å). Also, the data can be used to analyze the structural changes of nanoparticles absorbing small molecules such as oxygen. All these spectra showed the presence of the first two shells corresponding to Cu-O and Cu-Cu and the appearance of a third peak between 3.0 - 3.5 Å. This third peak was fairly significant in the spectra for all the samples along with the shoulder around 2 Å.

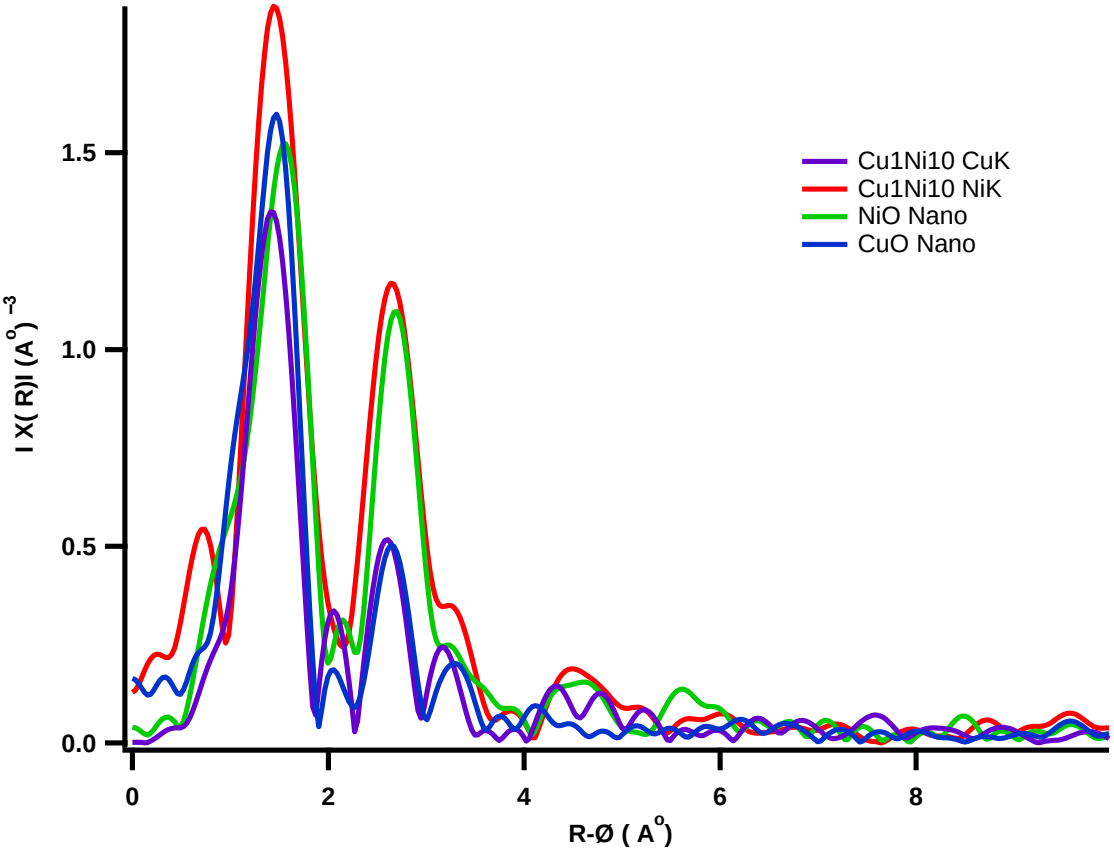

Figure 5.7 Radial distribution functions for Cu1Ni10 bimetallic nanoclusters at Cu K-edge with CuO and NiO nanoclusters.

The radial distribution function for Cu1Ni10 sample at Cu K-edge had considerable differences to the other bimetallic nanoclusters (as marked in the figure 5.6). Corresponding spectra have shown significant other peaks beyond 4.0 Å and higher intensity for second and third shells with the most intense shoulder around 2 Å. Also, these peaks were shifted towards a lower R.

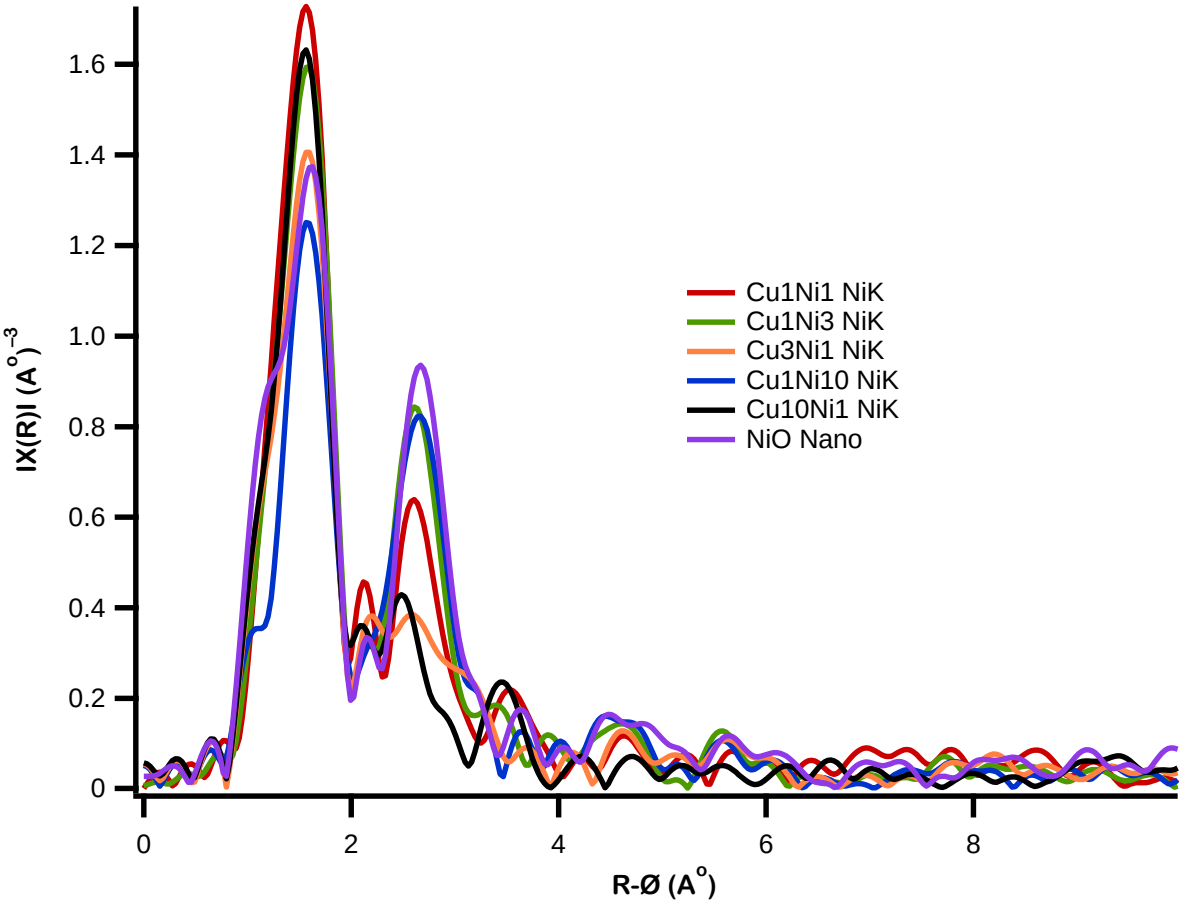

Figure 5.8 Radial distribution functions for bimetallic nanoclusters at the Ni K-edge.

Comparing the R space spectrum for the Cu1Ni10 sample at both K edges with the respective fully doped spectra for Ni and Cu oxide nanoparticles (NiO and CuO), as shown in the figure 5.7, there were no significant differences between the spectra for respective metal oxide nanoparticles with the highest Ni containing nanoparticle sample at the respective K-edge. Figure 5.8 shows the RDF for mixed metal oxide nanoclusters at the Ni K-edge. All these spectra follow a similar pattern aside from the intensity of the spectra. The intensity of the second shell of the RDF spectra at the Ni K-edge is mostly dependent on the concentration of the Ni present in the sample.

When comparing the RDF at the Cu K-edge and Ni K-edge, it was found that the mixed metal oxide nanoparticle sample with a higher concentration of nickel showed slight differences compared with the other nanoparticle samples at the Cu K-edge (figure 5.6), and vice versa is true for Ni K-edge (figure 5.8). Another interesting spectral difference observed for the RDFs at the Ni K-edge, there was no significant separation of the second and third peak for nanoparticle samples with a high concentration of Cu (Ni1Cu10 and Ni1Cu3) compared to the other spectra. This particular feature was common to the Ni1Cu10 and Ni1Cu3 samples, but the R space spectrum for Ni1Cu10 closely resembled the rest of the samples at the same K edge.

Overall, these results show that the k-space and R-space data for fumed silica supported mixed metal oxide nanoclusters have fairly good agreement with the respective metal oxide standards as well as the individual metal oxide nanoclusters at their respective K-edges. This is not sufficient to determine the architecture, such as the option sketched in (Figure 5.9.

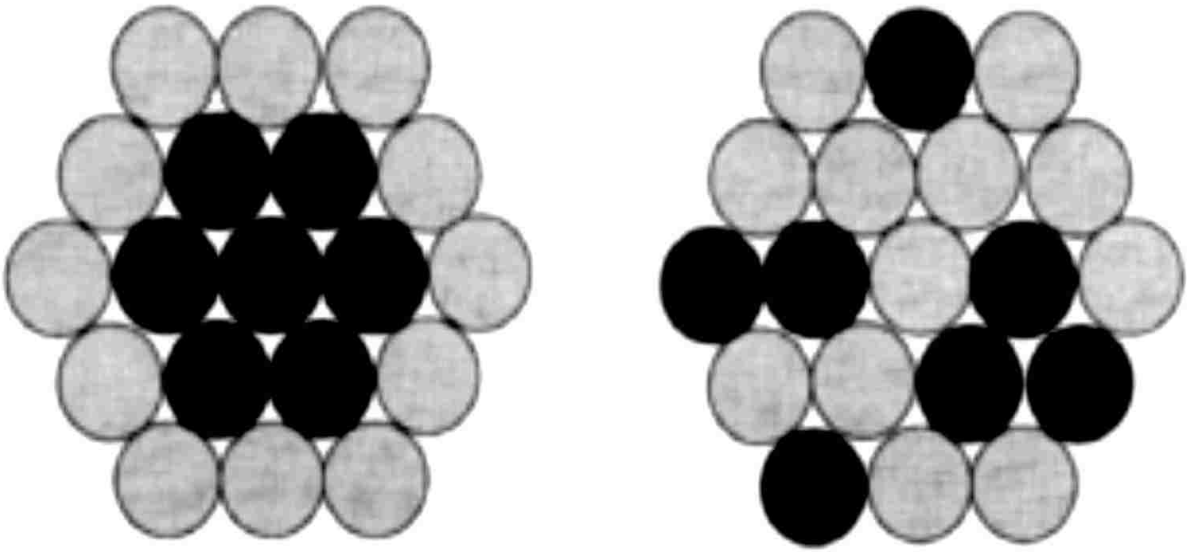

Figure 5.9 Suggested core - shell models [22].

5.4.3 XANES Data

Figure 5.10 shows the comparison of copper oxide standards with the copper oxide nanoclusters prepared at the fully doped or saturated condition.

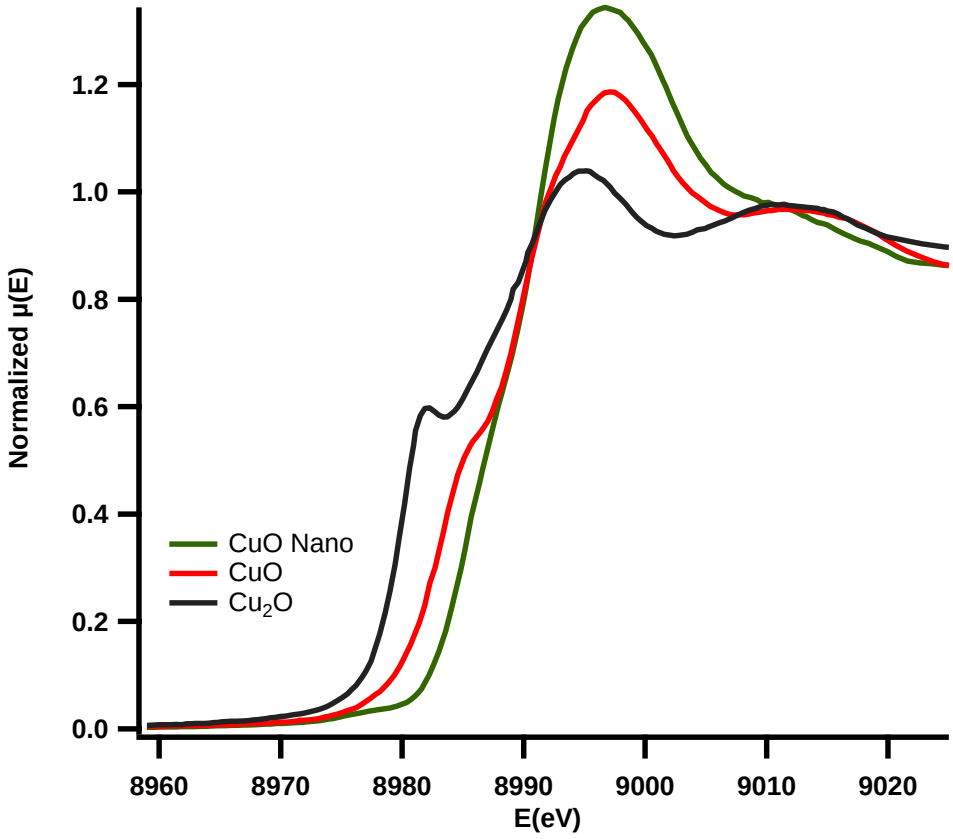

Figure 5.10 XANES spectra CuO nanoclusters with Copper oxide standards.

Note that the nanoparticles more closely resemble the Cu(II) standard, which we will also find for the mixed metal oxide clusters. With that said, there are noticeable differences between the nanoparticle spectrum and the Cu(II) standard, particularly the pre-edge shoulder. XANES data are given in figure 5.11, and they showed the absorption edges of the bimetallic nanoclusters had shifted to higher energy at the Cu K-edge compared to the Cu oxide standards and CuO nanoclusters. Bimetallic nanoclusters prepared at 3:1 Cu to Ni ratio, showed a slightly different trend compared to the other bimetallic samples.

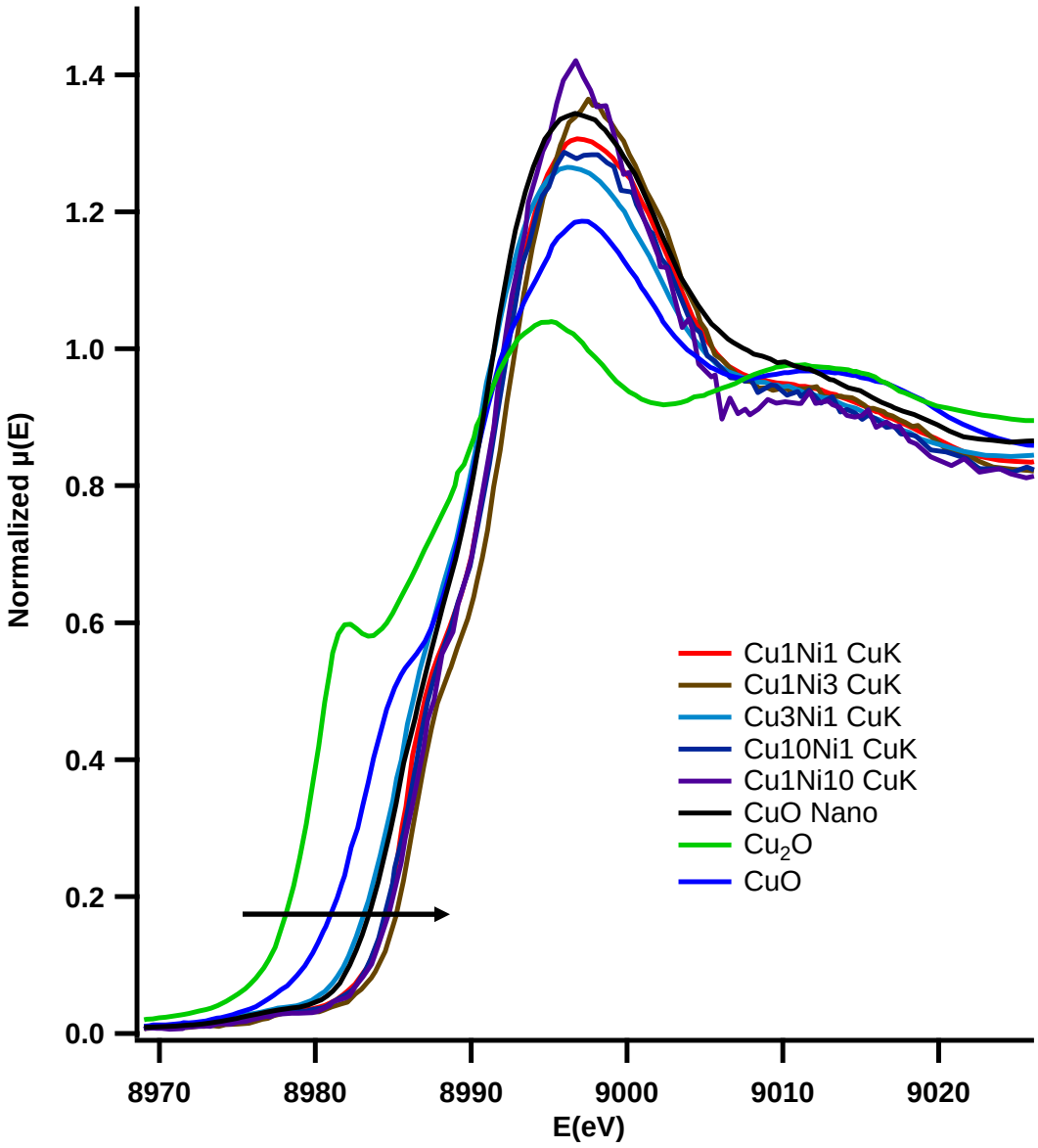

Figure 5.11 XANES spectra for bimetallic and CuO nanoclusters with copper oxide standards.

Notice that all of the samples closely resemble the Cu oxide nanoparticles, indicating that the nanoparticles have Cu in the +2 oxidation state. However, there were a couple of subtle differences worth noting. First, almost all of the thresholds for the mixed metal oxides were shifted to higher energy when compared to the pure copper oxide nanoparticles, indicating a more oxidized state. Second, there was an exception to this, namely, the particles with the most copper (3:1 for Cu:Ni ratio).

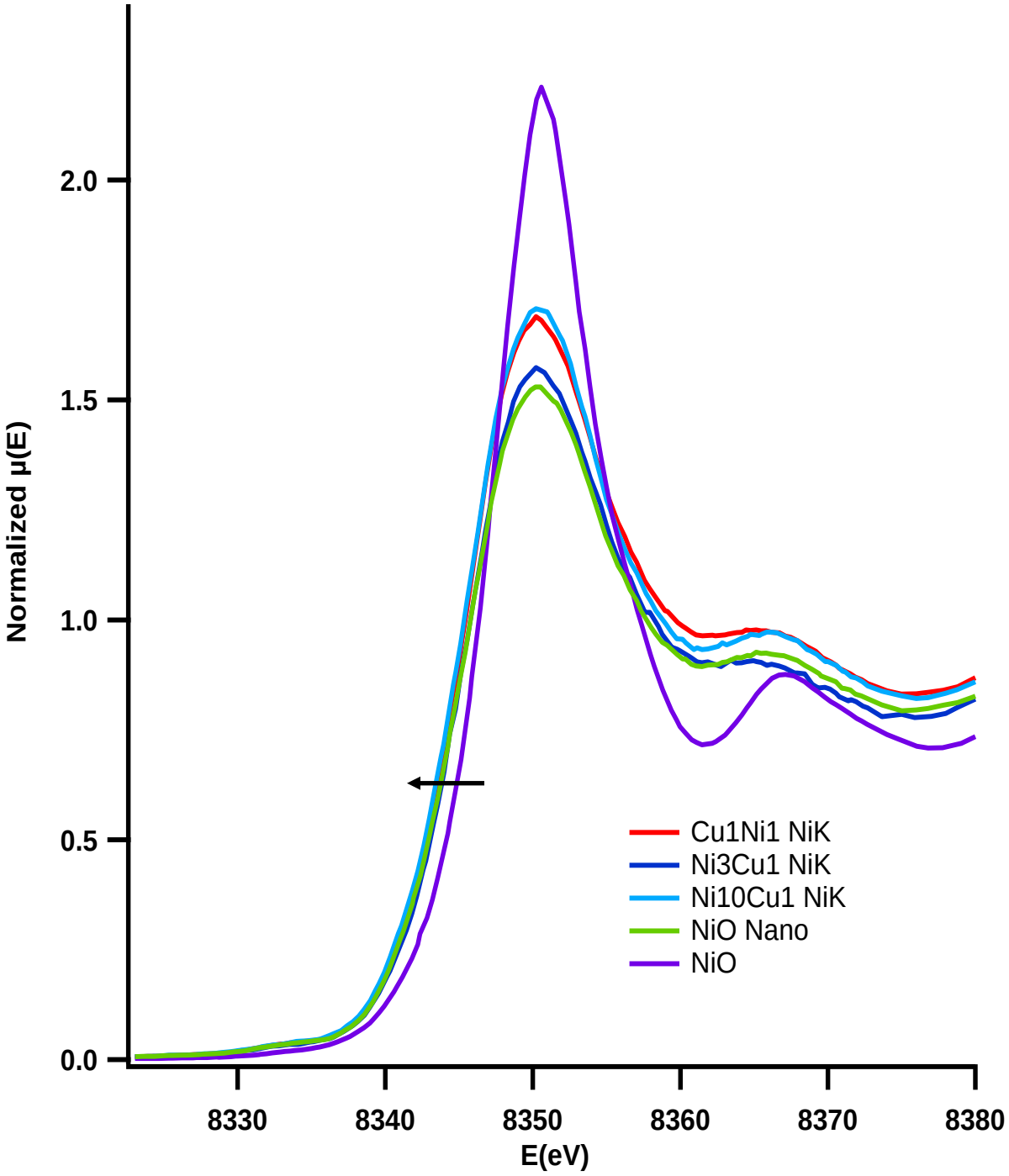

Figure 5.12 XANES spectra for bimetallic and NiO nanoclusters with Nickel oxide standard.

XANES data for both bimetallic and NiO nanoclusters at the Ni K-edge show the edge shift towards lower energy compared to the NiO standard (figure 5.12). Note that the shift for the

Ni was opposite from what was observed for the Cu K-edges, suggesting that the Cu became more electropositive while the Ni became more electronegative in the mixed metal oxide clusters.

5.5 Microscopic Data

Due to inconclusive evidence obtained from X-ray absorption spectroscopy regarding architecture, further studies were carried out at the University of Iowa's microscopic facility to broaden our understanding of the above observations. TEM, SEM and EDS studies were performed on the same samples to understand the nanoparticle formation and their composition. It was found that mixed metal oxides from nanoparticles contain both Ni and Cu metal in them. The percentage of the metals in the nanoparticles depends up on the concentration of the metal ion solution used during preparation. Figure 5.13 shows the TEM image (a) for Cu1Ni1 mixed metal oxide nanoparticles with (b) energy dispersive spectra for the selected nanoclusters (pt1 and pt2).

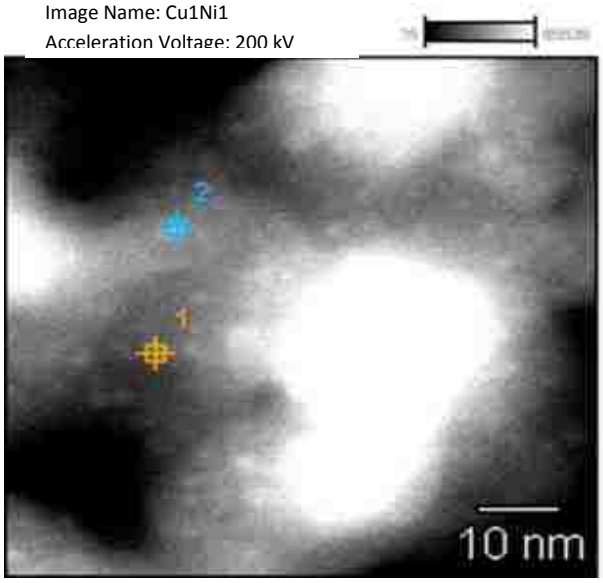

Figure 5.13 (a): High Angle Annular Dark Field TEM image of Cu1Ni1 mixed metal oxide nanoparticles

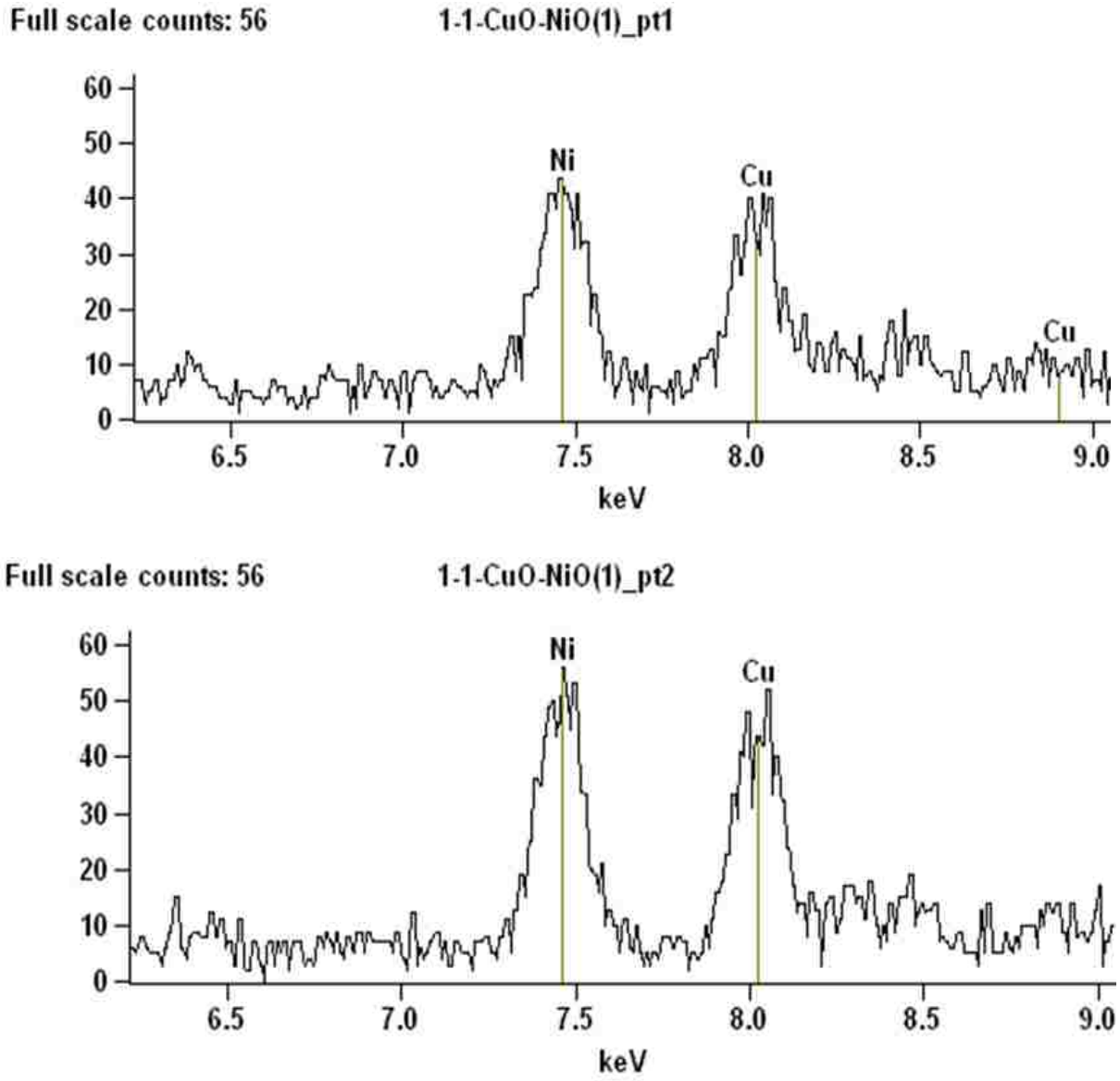

Figure 5.13 (b): Energy dispersive spectra (EDS) of Cu1:Ni1 mixed metal oxide sample at the selected nanoparticles (pt1 and pt2)

5.6 Summary of findings

The shift of absorption edge for XANES spectra for the mixed metal oxide nanoclusters (compared to the respective metal oxide standards) indicated a change in the geometry of the surrounding oxygen atoms during the formation of the metal oxide nanoparticle. At the Cu-K edge, the appearance of the very weak pre-edge feature around 8975-8980 eV, which is

responsible for the forbidden transition of 1s to 3d for octahedral symmetry, and the disappearance or shift of the shoulder at 8983-8986 eV, to higher energy indicated the existence of Cu (II) in the samples and the change of geometrical environment of Cu (II) from an octahedral to a tetragonal Cu (II) environment [23]. This may have lead Cu (II) in nanoclusters to have a more ionic structure with distorted tetragonal to tetrahedral geometry [24] or distorted octahedral geometry. The shift of absorption edge at the Ni-K edge towards lower energy suggested Ni was in a more electronegative environment compared to Cu in the mixed metal oxide nanoclusters.

According to the k-space data, most of these bimetallic nanoclusters have geometries closely resembling the monometallic oxide nanoclusters at their respective K-edges. Here, we assumed when preparing mixed metal oxides nanoclusters of CuO/NiO using their metal nitrates, samples that contained similar or higher percentages of copper ion may have predominantly formed nanocluster islands of CuO and NiO on the fumed silica surface. Samples containing comparatively higher amounts of nickel (Ni3Cu1 and Ni10Cu1) had a slight change in k-space spectra around 2.3 $(Å)^{-1}$ compared to the others (figure 5.4 and 5.5). This suggested there may have been some type of Ni/Cu alloying occurring in the samples with a higher percentage of Ni ions, or this could have been due to higher spectral noise.

According to the SEM and TEM data with energy dispersive spectra, the presence of both metals in one nanoparticle has been confirmed. Therefore, using information from both EDS and EXAFS, we can speculate that these nanoparticles contained both Ni and Cu and they segregated within the nanoclusters as their respective metal oxides, like in the proposed core-shell model (figure 5.9).

5.7 References

(1) Wang, D.; Li, Y. *Advanced Materials* **2011**, *23*, 1044.

(2) Gustafson, J.; Haire, A. R.; Baddeley, C. J. *Surface Science* **2011**, *605*, 220.

(3) Liu, Y.; Li, D.; Sun, S. *Journal of Materials Chemistry* **2011**, *21*, 12579.

(4) Susut, C.; Nguyen, T.; Chapman, G.; Tong, Y. *Journal of Cluster Science* **2007**, *18*, 773.

(5) Susut, C.; Tong, Y. *Electrocatalysis* **2011**, *2*, 75.

(6) Alayoglu, S.; Zavalij, P.; Eichhorn, B.; Wang, Q.; Frenkel, A. I.; Chupas, P. *ACS Nano* **2009**, *3*, 3127.

(7) Lai, F.-J.; Sarma, L. S.; Chou, H.-L.; Liu, D.-G.; Hsieh, C.-A.; Lee, J.-F.; Hwang, B.-J. *The Journal of Physical Chemistry C* **2009**, *113*, 12674.

(8) Hills, C. W.; Nashner, M. S.; Frenkel, A. I.; Shapley, J. R.; Nuzzo, R. G. *Langmuir* **1999**, *15*, 690.

(9) Nashner, M. S.; Frenkel, A. I.; Adler, D. L.; Shapley, J. R.; Nuzzo, R. G. *Journal of the American Chemical Society* **1997**, *119*, 7760.

(10) Alayoglu, S.; Nilekar, A. U.; Mavrikakis, M.; Eichhorn, B. *Nat Mater* **2008**, *7*, 333.

(11) Tedsree, K.; Li, T.; Jones, S.; Chan, C. W. A.; Yu, K. M. K.; Bagot, P. A. J.; Marquis, E. A.; Smith, G. D. W.; Tsang, S. C. E. *Nat Nano* **2011**, *6*, 302.

(12) Sarkar, A.; Manthiram, A. *The Journal of Physical Chemistry C* **2010**, *114*, 4725.

(13) Park, J. Y.; Zhang, Y.; Grass, M.; Zhang, T.; Somorjai, G. A. *Nano Letters* **2008**, *8*, 673.

(14) Chen, C.-H.; Sarma, L. S.; Chen, J.-M.; Shih, S.-C.; Wang, G.-R.; Liu, D.-G.; Tang, M.-T.; Lee, J.-F.; Hwang, B.-J. *ACS Nano* **2007**, *1*, 114.

(15) Antoniak, C. *Beilstein journal of nanotechnology* **2011**, *2*, 237.

(16) Harpeness, R.; Gedanken, A. *Langmuir* **2004**, *20*, 3431.

(17) Wang, A.-Q.; Chang, C.-M.; Mou, C.-Y. *The Journal of Physical Chemistry B* **2005**, *109*, 18860.

(18) Lomnicki, S.; Truong, H.; Vejerano, E.; Dellinger, B. *Environmental Science & Technology* **2008**, *42*, 4982.

(19) Vejerano, E.; Lomnicki, S.; Dellinger, B. *Environmental Science & Technology* **2010**, *45*, 589.

(20) Evans, C. S.; Dellinger, B. *Environmental Science & Technology* **2005**, *39*, 4857.

(21) Chandler, B.; Gilbertson, J.; Gade, L., Ed.; Springer Berlin / Heidelberg: 2006; Vol. 20, p 97.

(22) Toshima, N.; Yonezawa, T. *New Journal of Chemistry* **1998**, *22*, 1179.

(23) Kau, L. S.; Spira-Solomon, D. J.; Penner-Hahn, J. E.; Hodgson, K. O.; Solomon, E. I. *Journal of the American Chemical Society* **1987**, *109*, 6433.

(24) Kau, L. S.; Hodgson, K. O.; Solomon, E. I. *Journal of the American Chemical Society* **1989**, *111*, 7103.

Chapter 6
X-ray Studies of Copper Oxide Nanoparticles on a Silica Matrix Exposed to Different Types of Dioxin/Furan Precursors

6.1 Introduction

The work presented in this chapter represents a set of experiments carried out to investigate the role of size controlled metal oxide nanoparticles in surface mediated reactions. Here, we consider dendrimerically prepared size controlled copper oxide (CuO) nanoparticles supported on a fumed silica surface that can serve as a model for fly ash. The experiment was performed by exposing the supported CuO nanoparticles with precursor molecules that have been reported to form surface associated free radicals that persist longer than typical free radicals. Such environmentally persistent free radicals (EPFRs) can also lead to the formation of polychlorinated dibenzo-p-dioxins (PCDDs) and polychlorinated dibenzo-furans (PCDFs) which are known to cause hazardous health effects [1-4]. Selection of such precursors is done by choosing mono/ poly chlorinated benzenes and phenols which can be byproducts of incompletely combusted organic materials [5,6].

The goals of this set of experiments were to determine the fate of Cu^{+2} ions present in the fumed silica supported copper oxide nanoparticles after exposure to the precursors using X-ray absorption near edge spectroscopy (XANES), and to check if the results were consistent with XANES data published in 2005 for micron scale particles at higher temperatures [3]. As mentioned previously, element specific studies in complex mixtures are rather common in soil science, geochemistry and catalysis literature [7-12]. To investigate the influence of the precursor adsorbate on the nanoparticle, XANES experiments were performed on the exposed nanoparticles at the Cu K-edge. Then, the spectra were compared to the unexposed samples as well as the two copper oxide standards to check the changes in the absorption edge as well as the radial distribution

functions for the geometry changes in metal oxide nanoclusters during the chemisorption process.

6.2 Background and Motivation

Over the last decade, findings of the environmental and combustion research community have suggested that surface mediated reactions are responsible for the formation of a significant fraction of toxic air pollutants due to combustion related processes. It is well established that transition metals found in fly ash play an active role in the formation of surface associated long-lived free radicals known as EPFRs, and are also responsible for the production of dangerous persistent organic pollutants, such as dibenzo-p-dioxins (PCDDs) and polychlorinated dibenzo-furans (PCDFs) [3-5,13,14]. Among transition metals, oxides of Cu, Ni, Zn and Fe have received particular attention[14,15] due to their ability to form different size (nano- to micron size) particles on many different surfaces (i.e. SiO_2, Al_2O_3, TiO_2 and CaO) that may be present in native fly ash.

There are two different surface mediated pathways proposed for the formation of PCDDs and PCDFs. Namely they are known as de novo and precursor pathways; both have been reported to form PCDDs and PCDFs at temperatures approximately between 250 and 450 ^oC with the maximum efficiency around 350^oC [3]. In de novo pathway, PCDD/Fs are formed by the carbon species present in the fly ash via processes such as oxidation and chlorination at the appropriate reaction conditions [4,16,17]. However, in the precursor pathway, PCDD/Fs are formed by aromatic precursors like poly/mono-chlorinated phenols and benzenes via surface mediated association processes or coupling reactions [3,13,18].

Environmentally persistent free radicals (EPFRs) are formed by adsorption of substituted aromatic precursors (i.e. chlorinated phenols or benzenes) on to a transition metal oxide (i.e.

CuO) surface [13,14]. Formation of EPFRs is possible at temperatures between 100 and 400 °C where this temperature range corresponds to the combustion cool zone and post flame conditions. Here, both substituted phenoxyl and semi-quinone radicals can be formed depending upon the adsorption temperature and the nature of the precursor. In general, EPFRs are formed through a mechanism of initial physisorption, then chemisorption via elimination of hydrogen chloride or water, accompanied by an electron transfer resulting in simultaneous reduction of the transition metal (i.e. Cu(II) to Cu(I)) to form the metal ion associated EPFR (other transition metals (redox-active) such as iron and nickel are also expected to mediate the formation of EPFRs) [4,13,14].

Regardless of the formation path, at the low temperature post combustion region, the presence of a transition metal is required for the formation of PCDD/Fs and EPFRs. It has also been suggested that both the de novo and precursor paths probably involve the same reaction intermediates during surface associated reactions [5,16].

Two of the few previous studies on reactions of PCDD/F precursors with model fly ash (5% bulk CuO supported on fumed silica) and high temperature reduction of Cu(II)O by 2-chlorophenol on simulated fly ash have proposed a few possible mechanisms for the formation of PCDD/Fs and EPFRs via surface associated reactions as in the figure 6.1. Results of these studies suggest that PCDDs were formed through the Eley-Rideal mechanism and PCDFs were formed via the Lanmuir-Hinshelwood mechanism [3,19-21].

Comparison of the experimental data with the literature reported gas phase radical-radical or/and radical-molecule reactions of 2-MCP and EPR spectroscopic studies by Dellinger et al. suggested that when 2-MCP is absorbed onto the CuO supported silica surface , chlorophenol absorbs to the Cu^{+2} site as chlorophenolate as in the scheme below [3]. Here, the surface associated

radical is formed by electron transfer from the chlorophenolate to the metal cation site with the reduction of Cu^{+2} to Cu^{+1}.

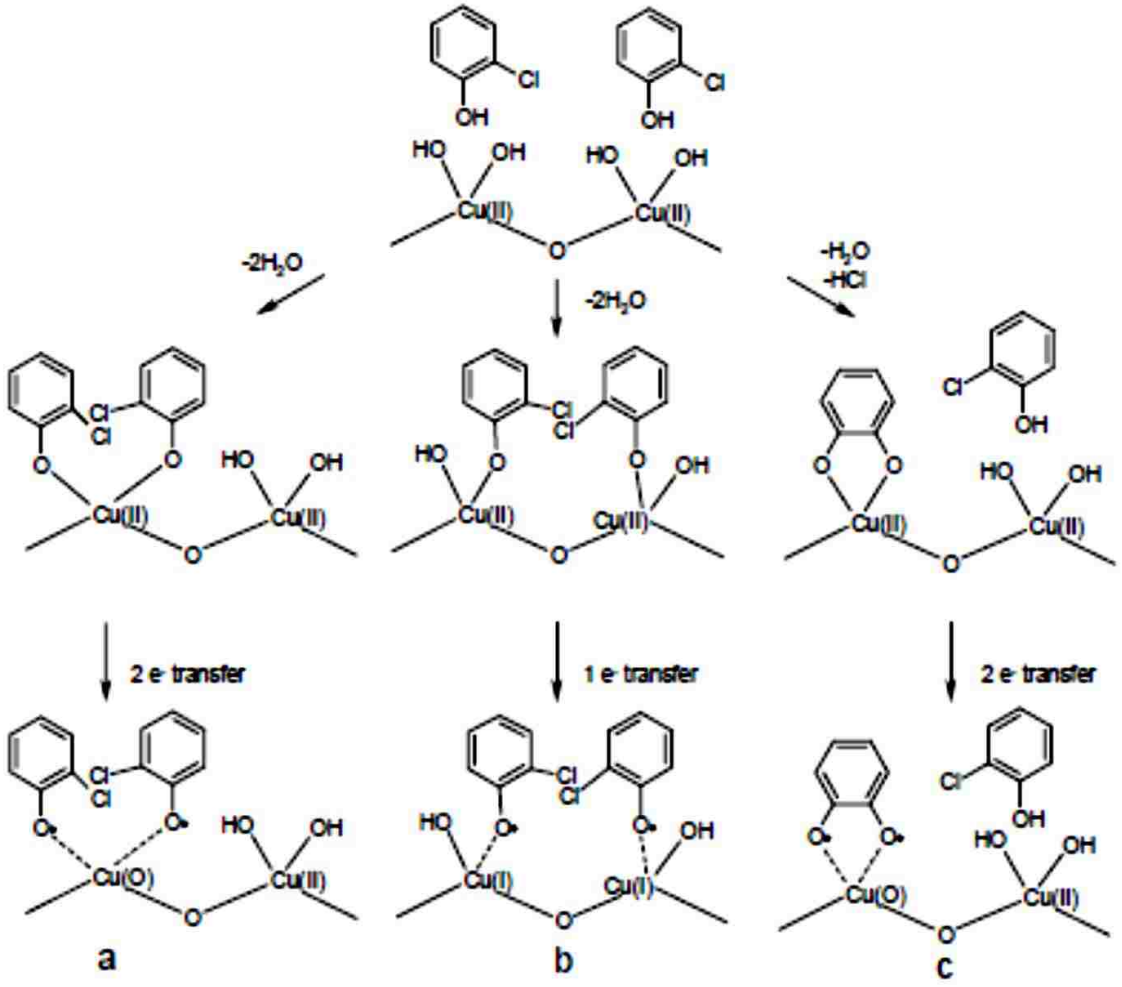

Figure 6.1 Possible mechanisms for the adsorption of 2-chlorophenol and reduction of Cu (II) O on fumed silica support matrix[4]. We were interested in pathway b, two 2-chlorophenols are chemisorbed at vicinal sites and result in formation of Cu (I) by a 1e- transfer reaction at each site.

According to the work done by Dr. Barry Dellinger and Dr. E.D. Poliakoff, CuO tended to reduce to Cu_2O in the presence of 2-chlorophenol (MCP) at 375 ^{o}C. Later they found 1,2 dichlorobenzene (DCBz) and chlorobenzene (MCBz) also have the ability to reduce CuO to Cu_2O upon exposure at temperatures between 275 - 375 ^{o}C [3]. The earlie work by Dellinger and Poliakoff was performed on micron scale copper oxide particles.

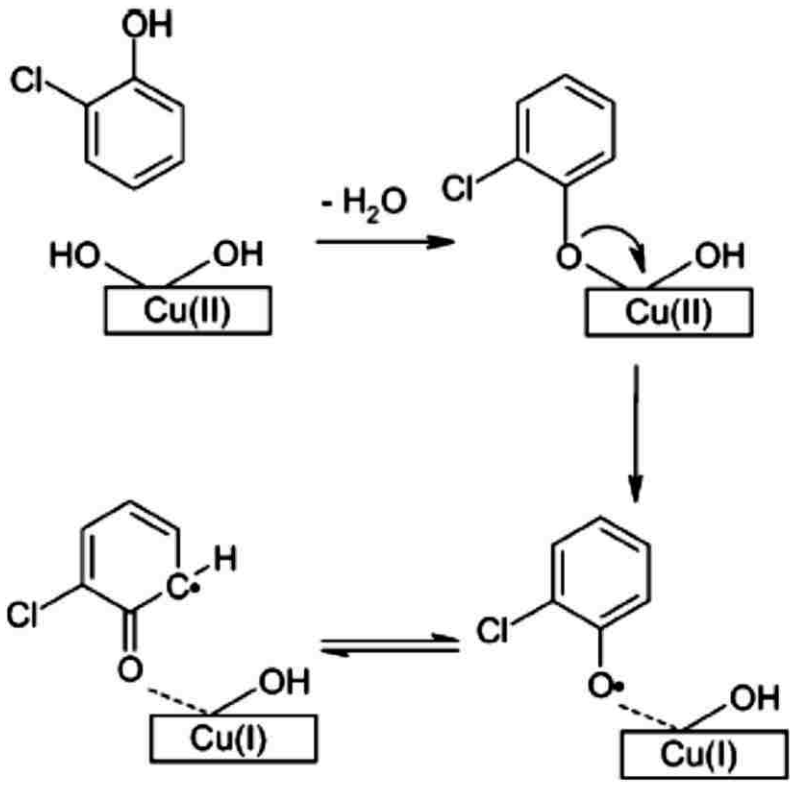

Figure 6.2 Formation of Chlorophenoxyl radical from the absorption of 2-Chlorophenol on surface hydroxyl of CuO [3].

For my work, dendrimerically prepared size controlled CuO nanoparticles were used instead of bulk CuO. Here, we wanted to understand the behavior of CuO nanoparticles supported on fumed silica in surface mediated reactions which form EPFRs and PCDD/Fs. Also, we wanted to check whether supported nanoparticles behave similarly to bulk CuO by changing oxidation state at a specific temperature range as mentioned earlier.

6.3 Experimental Method

Two sets of experiments were planned by using 2-chlorophenol (2-MCP) as the PCDD/F precursor. The first experiment was performed by reacting the model precursor with different size nanoparticles keeping the reaction (exposing) temperature at 250^{o}C. During the second experiment the same precursor was used with one particular size nanoparticle by changing the

reaction temperature from 250-400^{o}C. Another set of experiments was performed to check the precursor effect on the CuO nanoparticle surface by changing the type of the model precursor the with same selected nanoparticle size keeping the reaction temperature at 250^{o}C.

The reaction/exposure of dendrimerically prepared size controlled nanoparticles to model precursors was performed inside a slightly modified apparatus developed by Dellinger et al. as explained in chapter two. During the second set of experiments, nanoparticles prepared at the 2:1 (ratio between number of NH_2 groups of DAB-G_4 dendrimer to Cu^{+2} ions) condition were selected as the CuO reaction surface, and six different temperatures (250, 300, 325, 350, 375 and 400 ^{o}C) were used to perform the surface exposure reaction. Then, samples from both sets of experiments were collected into vials and sealed in inert atmosphere. Samples for the DCM beamline were prepared as explained in previous chapters by dispersing them on Kaptan tape. X-ray absorption measurements were obtained at the Cu K-edge for all the samples.

6.4 Results and Discussion

Figure 6.3 depicts the XANES spectra for 2-chlorophenol reacted fumed silica supported CuO nanoparticles, prepared at the fully doped condition, at different temperatures compared with two copper oxide standards. Comparison of spectra for the unreacted CuO nanoparticles with the reacted nanoparticle at 250^{o}C did not show any spectral shifts. However at 375^{o}C, 2-chlorophenol reacted CuO nanoparticles show a slight shift in the spectral edge towards lower energy. This observation corresponds to the reduction of Cu (II) species present in the nanoparticles, but the spectra did not show a complete reduction of Cu (II) → Cu (I) when compared with two copper oxide standards.

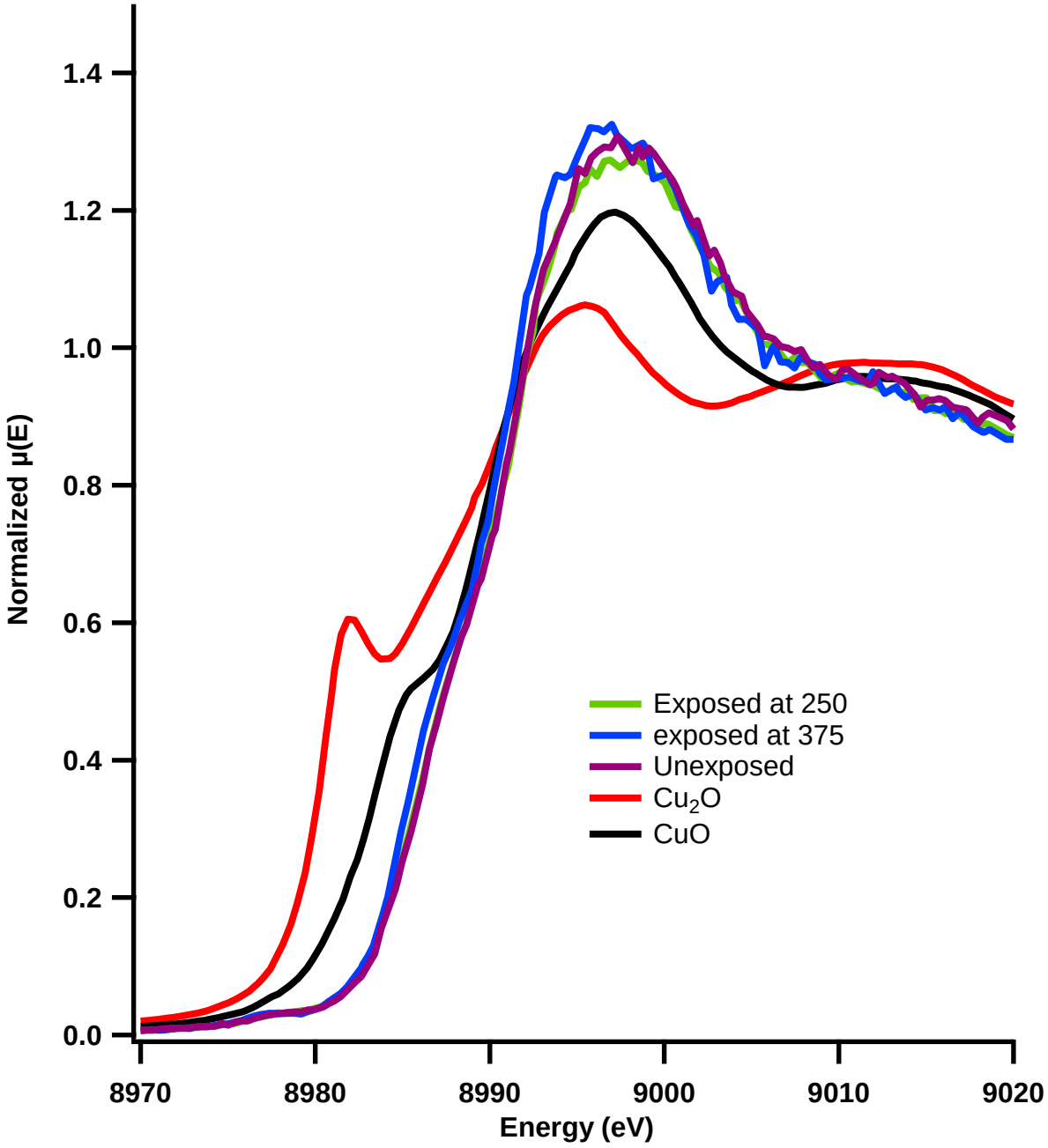

Figure 6.3 XANES spectra for the CuO nanoparticles (fully doped) exposed 2-Chlorophenol at different temperatures.

Even though supported CuO nanoparticle systems produce partial reduction of the Cu(II) species present, our observations are in good agreement with the reported reaction conditions that are known to be favorable in formation of PCDD/Fs.

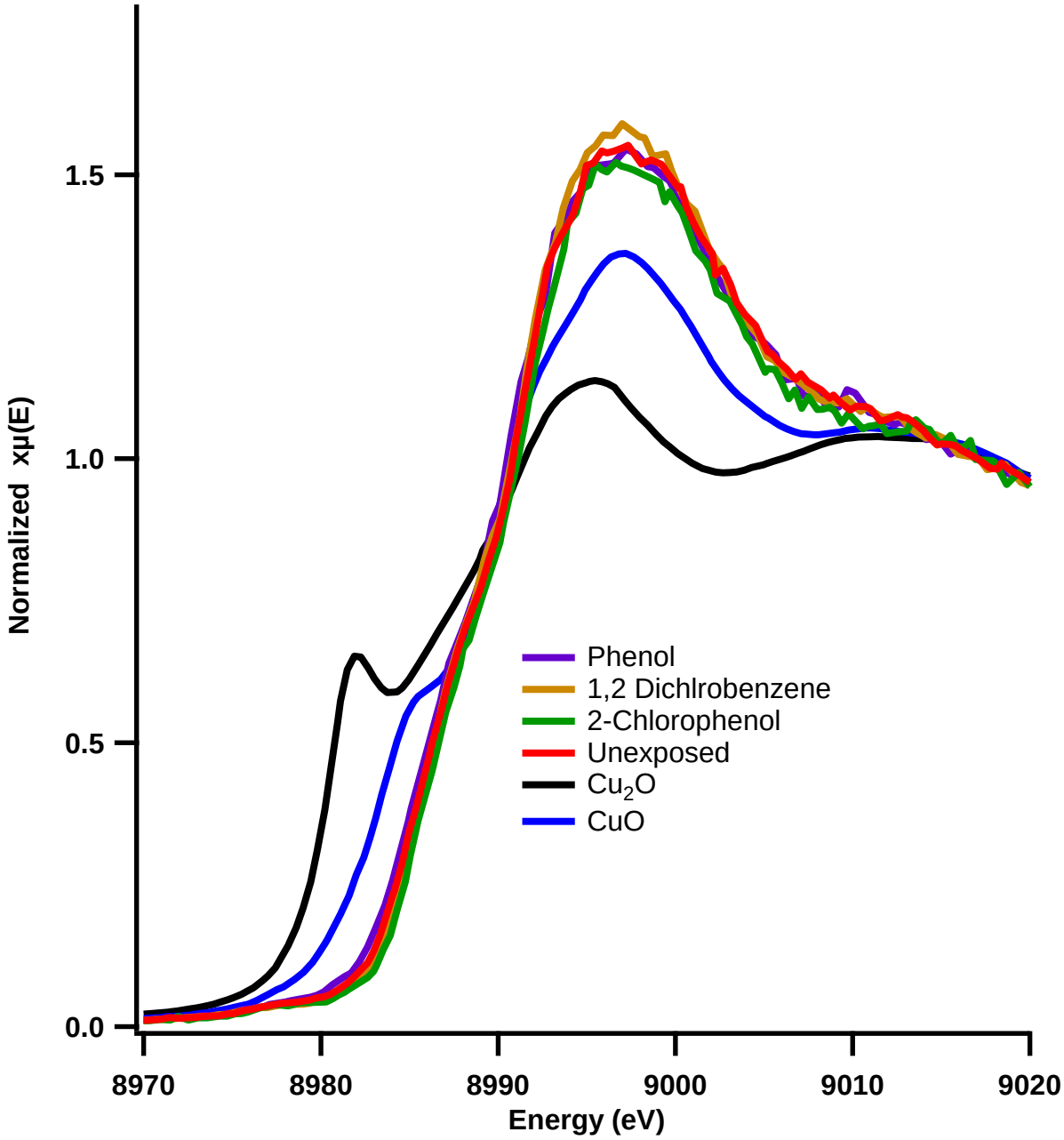

Figure 6.4 XANES spectra for the CuO nanoparticles (fully doped) exposed to different types of dioxin precursors.

Figure 6.4 shows the XANES spectra for the CuO nanoparticles prepared at fully doped conditions reacted with different types of dioxin precursors. We used 1, 2-dichlorobenzene and phenol as other possible precursors which are reported to form PCDDs, PCDFs, and EPFRs.

Comparison of nanoparticles reacted with different types of PCDD/Fs precursors did not show a significant difference with the unexposed samples.

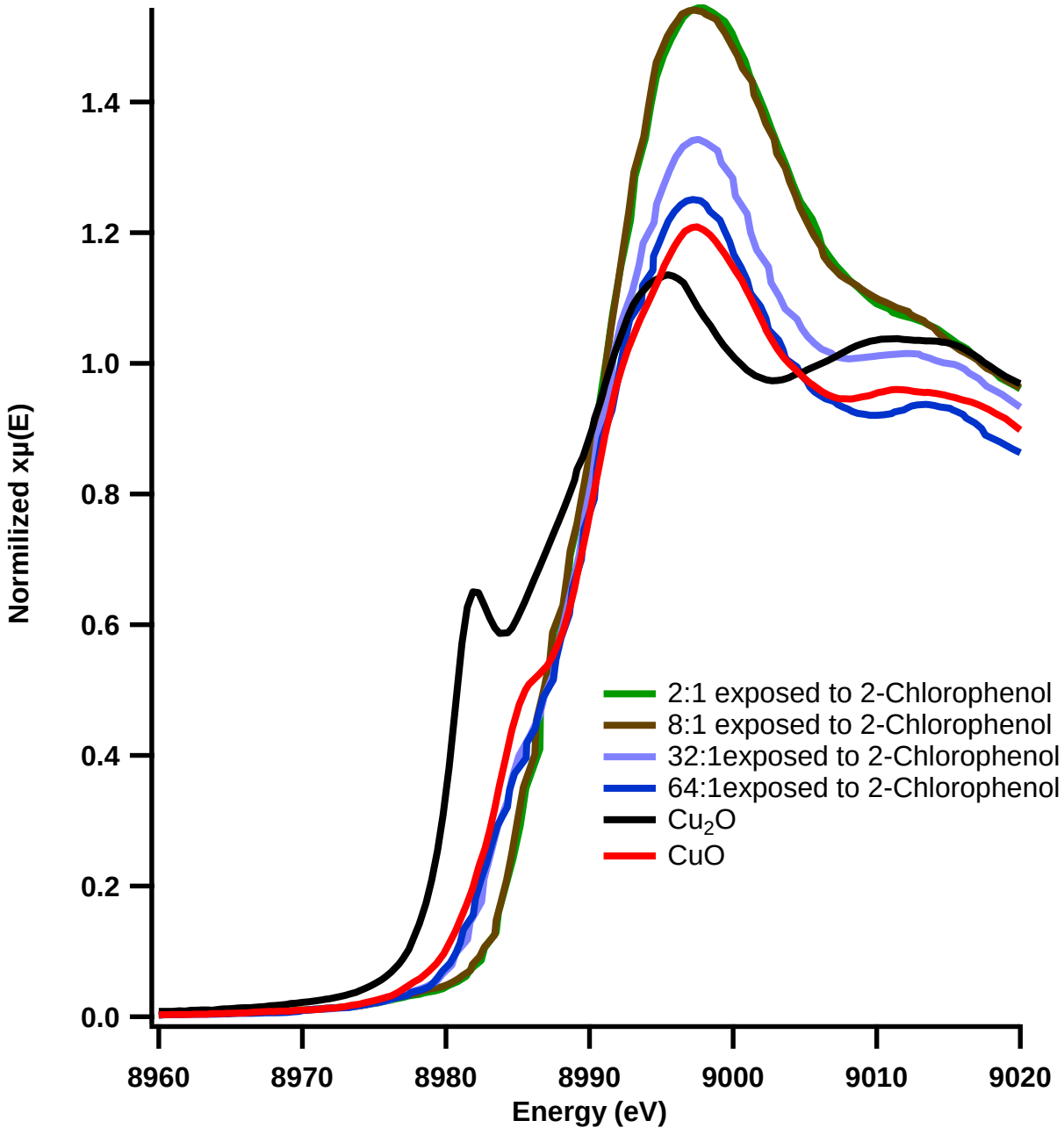

Figure 6.5 Different size nanoparticles reacted with identical PCDD/F precursor (2-Chlorophenol) at 250^{o}C.

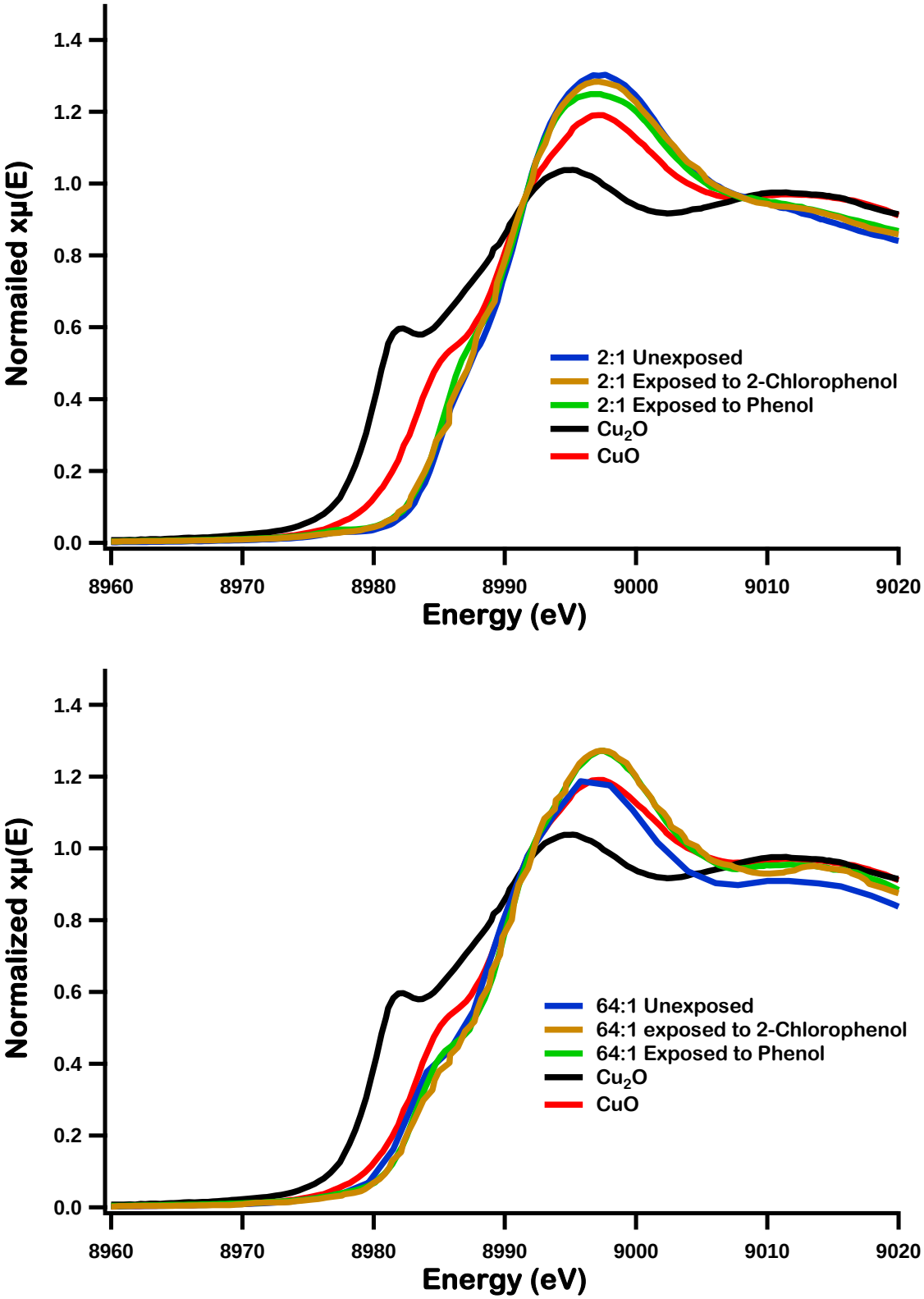

Figure 6.6 Different size nanoparticles reacted with different PCDD/F precursors at 250°C.

The same observation is true for the different size nanoparticles that were exposed to both identical and different PCDD/F precursors at 250^{o}C as in figure 6.5 and 6.6. The reaction conditions used in our system provide necessary and sufficient requirements for EPFRs formation, but the absence of edge shift suggested silica supported nanoparticle systems did not participate for EPFR formation via Cu(II) associated surface mediated reactions below 350^{o}C. Therefore, we assumed unlike Cu(II) species present in the bulk CuO/ SiO_2 system, Cu(II) in fumed silica supported CuO nanoparticles did not undergo full reduction and may only result in partial reduction upon reaction with 2-Chlorophenol at 375^{o}C. This idea was further confirmed with the absence of any observable edge shift at the lower temperatures including the experiments performed at 250^{o}C with different size nanoparticles.

In summary, this set of X-ray absorption spectroscopy data provides critical information regarding the reaction of CuO nanoparticles with PCDD/Fs precursors inside the above mentioned dosing apparatus. We were not able to produce data where the formation of PCDD/Fs occurred via surface mediated processes by complete reduction of Cu (II) → Cu(I) as reported previously [3,4]. Also, we did not see any significant changes in the XANES spectra due to the reduction of Cu (II) species present in the nanoparticles exposed or reacted at temperatures below 375^{o}C.

These experimental observations raise two questions

1. Are these Cu (II) species really undergoing full reduction as reported earlier or is there only a partial reduction of the Cu(II) species happening during surface mediated reactions of model PCDD/Fs precursors (e.g., 2-chlorophenol)?
2. Was there a problem with the amount of CuO nanoparticles exposed to the model precursor inside the sample vial during the allocated reaction time (ten minutes)?

I assumed that only Cu (II) species present in the top surface of the CuO nanoparticle sample may have reacted with 2-chlorophenol and the bulk of the 5% CuO nanoparticles supported on fumed silica remained unreacted inside the sample vial. Since X-ray absorption spectroscopy (XAS) is a technique which considers the bulk property of an experimental sample and our beamline samples may consist of a significantly lower fraction of reduced Cu (II) compared to the total amount of Cu (II), we might not be able to see any or only a small edge shift for our samples used for XAS at lower temperatures (250^{o}C - 350^{o}C). However, the observation of a slight shift in the Cu K-edge (figure 6.3) for the CuO nanoparticle samples exposed (or reacted) to 2-chlorophenol using the same experimental conditions at 375 ^{o}C would indicate there is a significant need to further investigate the importance of the reaction temperature during surface mediated reactions that form PCDD/Fs.

6.5 Conclusion and Future Directions

Our results gave good agreement with the proposed mechanism for 2-chlorophenols (by Barry Dellinger and E.D Poliakoff, published in 2005 [3] at 375^{o}C. There were a few practical difficulties in exposing and transporting exposed samples along with time gap between performing X-ray experiments after the exposure. These experimental observations, concerns and literature reported mechanisms lead to new avenues in using XAS to study in pollution formation via surface mediated reactions. During these experiments we will be using copper oxide nanoparticles (of different sizes starting with one) by exposing them to known precursors of polychlorinated dioxins/furans, like mono/di-chlorobenzene and mono/poly chlorinated phenolic adsorbates, starting with phenols. Here, we are planning to perform a set of XAS experiments with in-situ exposure of model dioxin/furan precursors to nanoparticles and so avoiding difficulties such as the amount of exposure and lead times. Chad Thibodeaux is taking

the lead in this part of the experiment with a modified design of a reaction chamber where we could perform in-situ exposure at the beamline and avoid the delay time between sample exposure and data collection as well as increase the percent exposure of Cu (II).

6.6 References

(1) Van den Berg, M.; Birnbaum, L. S.; Denison, M.; De Vito, M.; Farland, W.; Feeley, M.; Fiedler, H.; Hakansson, H.; Hanberg, A.; Haws, L.; Rose, M.; Safe, S.; Schrenk, D.; Tohyama, C.; Tritscher, A.; Tuomisto, J.; Tysklind, M.; Walker, N.; Peterson, R. E. *Toxicological Sciences* **2006**, *93*, 223.

(2) Wilhelm, M.; Wittsiepe, J.; Lemm, F.; Ranft, U.; Krämer, U.; Fürst, P.; Röseler, S.-C.; Greshake, M.; Imöhl, M.; Eberwein, G.; Rauchfuss, K.; Kraft, M.; Winneke, G. *Mutation Research/Reviews in Mutation Research* **2008**, *659*, 83.

(3) Alderman, S. L.; Farquar, G. R.; Poliakoff, E. D.; Dellinger, B. *Environmental Science & Technology* **2005**, *39*, 7396.

(4) Farquar, G. R.; Alderman, S. L.; Poliakoff, E. D.; Dellinger, B. *Environmental Science & Technology* **2003**, *37*, 931.

(5) Tuppurainen, K.; Halonen, I.; Ruokojärvi, P.; Tarhanen, J.; Ruuskanen, J. *Chemosphere* **1998**, *36*, 1493.

(6) Hagenmaier, H.; Kraft, M.; Brunner, H.; Haag, R. *Environmental Science & Technology* **1987**, *21*, 1080.

(7) Schulze, D. G.; Bertsch, P. M. In *Advances in Agronomy*; Donald, L. S., Ed.; Academic Press: 1995; Vol. Volume 55, p 1.

(8) Ginder-Vogel, M.; Sparks, D. L. In *Developments in Soil Science*; Balwant, S., Markus, G., Eds.; Elsevier: 2010; Vol. Volume 34, p 1.

(9) Ginder-Vogel, M.; Landrot, G.; Fischel, J. S.; Sparks, D. L. *Proceedings of the National Academy of Sciences* **2009**.

(10) Kleymenov, E.; Sa, J.; Abu-Dahrieh, J.; Rooney, D.; van Bokhoven, J. A.; Troussard, E.; Szlachetko, J.; Safonova, O. V.; Nachtegaal, M. *Catalysis Science & Technology* **2012**, *2*, 373.

(11) Bare, S. R.; Kelly, S. D.; Ravel, B.; Greenlay, N.; King, L.; Mickelson, G. E. *Physical Chemistry Chemical Physics* **2010**, *12*, 7702.

(12) Lombi, E.; Susini, J. *Plant and Soil* **2009**, *320*, 1.

(13) Lomnicki, S.; Truong, H.; Vejerano, E.; Dellinger, B. *Environmental Science & Technology* **2008**, *42*, 4982.

(14) Vejerano, E.; Lomnicki, S.; Dellinger, B. *Environmental Science & Technology* **2010**, *45*, 589.

(15) Yinon, L.; Themelis, N. J.; McNeill, V. F. *ASME Conference Proceedings* **2010**, *2010*, 85.

(16) Huang, H.; Buekens, A. *Science of The Total Environment* **1996**, *193*, 121.

(17) Hell, K.; Stieglitz, L.; Dinjus, E. *Environmental Science & Technology* **2001**, *35*, 3892.

(18) Iino, F.; Imagawa, T.; Takeuchi, M.; Sadakata, M.; Weber, R. *Chemosphere* **1999**, *39*, 2749.

(19) Lomnicki, S.; Dellinger, B. *Proceedings of the Combustion Institute* **2002**, *29*, 2463.

(20) Lomnicki, S.; Dellinger, B. *The Journal of Physical Chemistry A* **2003**, *107*, 4387.

(21) Khachatryan, L.; Lomnicki, S.; Dellinger, B. *Chemosphere* **2007**, *68*, 1741.

Chapter 7
General Conclusions and Outlook

7.1 Conclusions

The general objectives of our study were to synthesize well defined nanoparticles of different size, supported on different types of inert substrates with high surface area, and to use these systems as laboratory surrogates for combustion generated fly ash to understand their role in the formation of surface associated pollutants via surface mediated processes. The purpose of the study was to obtain information about electronic structure, coordination geometry, oxidation state and coordination number of the transition metal present in the metal oxide nanoparticles on selected support substrates using X-ray absorption spectroscopic studies. To obtain supportive size, morphology and elemental information, HR-TEM (with EDS) and SEM were also used. The dendrimeric method was used to synthesize transition metal oxide nanoparticles with lower disparity on porous support surfaces. During the course of these studies, generation four (G4) or generation three (G3) diaminobutane core poly (propylene imine) dendrimers (DAB-Am_n, i.e.G4;DAB-Am_{32} and G3; DAB-Am_{16}) were used as scaffolds for the nanoparticle preparation. The sizes of the nanoparticles were controlled by manipulating the concentration ratio between the dendrimer and the metal ion. In this study, experiments were performed with a few different transition metals, Cu, Ni and Fe, and our main emphasis was given to the nanoparticle systems containing Copper and Nickel/Copper. All the metal oxide nanoparticle samples were prepared to have 5% metal oxide (w/w) on the selected solid support substrate. During our experiments, Cu(II) ions were complexed with G4-DAB-Am_n in methanol and the synthesis was carried out by varying the concentration ratio of dendrimer (DAB-Am_{32}) to Cu(II) ions to have a series of samples according with the following formula:

$DAB\text{-}Am_{32} - Cu(II)_n$ where ***n* = 0.5, 1.0, 2.0, 4.0, 8.0, 16.0.**

These complexes were impregnated on selected substrates, and the solvent was evaporated after 30-60 minutes (allowing enough time to form nanoparticles on support surfaces with occasional mixing).The dendrimer templates were removed by calcination of the supported sample in a tube furnace under oxidative conditions at 450^{o}C for 3 hours. X-ray absorption spectroscopy, both XANES and EXAFS, were performed to accrue structural and oxidation information on the nanoparticles. Microscopy studies, HR-TEM and SEM, were performed to identify the nanoparticle sizes and composition.

Both microscopy and spectroscopi studies found the, smallest nanoparticle sizes were observed for the nanoparticles that were prepared at the quarter doped condition (n = 4) and the largest sizes at the severely under doped condition (n =0.5). Also, we observed a decreasing trend in the particle size for the nanoparticles prepared at the fully doped (n=16) condition to the quarter doped (n=4) condition. X-ray absorption spectroscopic data (both XANES and EXAFS) at Cu-K edge revealed copper species present in the nanoparticles have oxygen as the nearest neighbor (central copper atom is bonded to an oxygen atom) and possess Cu^{+2} oxidation state. It is also revealed that the structure of fumed silica supported CuO nanoparticles should be a distorted octahedral structure, since x-ray absorption spectra do not have a shoulder which is responsible for tetrahedral geometry and the spectra do show the pre-edge feature for the 1s$\rightarrow$ 3d forbidden transition for octahedral symmetry. EXAFS data show a lack of long range order in the smaller nanoparticles (prepared at fully doped to quarter doped condition), which indicates the presence of flatter and amorphous nanoparticles on fumed alumina support surface.

Another set of experiments were performed to study the effect of support substrate on particle formation. Here, experiments were performed for copper on alumina using the same procedures that were employed for copper on silica. The XANES region of the X-ray absorption

spectra showed a shift of absorption edge towards higher energy along with the appearance of a pre-edge peak due to the forbidden 1s→ 3d transition and the disappearance of the shoulder due to the 1s→4p transition suggested that copper species present in the dendrimerically prepared alumina supported copper sample have a Cu+2 oxidation state and copper may present in a distorted octahedral geometry.

The presence of first shell peak corresponding to oxygen in the radial distribution functions for all the spectra suggested that Cu+2 ions present in the samples are coordinated to oxygen atom. Also, the absence of long range order for samples prepared at any of the doping conditions indicate copper species may not have formed CuO nanoparticles on the fumed alumina support surfaces. This observation was supported by TEM and SEM studies. TEM images did not show the presence of any nanoparticles on the alumina support surface. However, SEM EDS studies indicated although CuO did not show formation of nanoparticles on alumina support, copper does exist in all the samples. Therefore, all these observations and literature findings indicated that copper species present in the support alumina substrate may exist in an axially distorted open octahedral environment where Cu^{+2} ions are coordinated to oxygen or as CuO sites attached to positively charged fumed alumina.

During the next set of experiments our intention was to form Ni-Cu hybrid material supported on fumed silica as a fly ash surrogate and to understand the variation of X-ray absorption spectra with respect to the individual silica supported nanoparticles. This was an extension of previous collaborative work with McCarley et al. and Dellinger et al. that demonstrated the ability of Ni(II) and Cu(II) to form well defined nanoparticles with diaminobutane core poly (propylene imine) dendrimer (DAB-Am_n where; n= 4,8,16,32,64) [1,2] .

Here, fumed silica supported mixed metal oxide nanoparticles were prepared in the presence of both these metal ions using dendrimeric preparation techniques.

The synthesis was carried out by complexing generation three, G-3, DAB-Am_n (DAB-Am_{16}) dendrimer with both Cu^{+2} and Ni^{+2} in different NH_2: (metal ions) molar ratios as described in the experimental section. The dendrimer-metal complexes supported on fumed silica had 5% metal oxide present on the support substrate. The samples were calcinated in the tube furnace at 450^oC for three hours under controlled air flow.

TEM and SEM data confirmed the formation of nanoparticles on the support surface and the presence of the metals in the selected areas of the sample. X-ray absorption spectroscopic data for the mixed metal oxide nanoclusters at the respective K-edges suggested that the nanoclusters consisted of oxides of both metals. k-space EXAFS data shows fairly similar spectra for nanoparticles prepared at all the different metal ion combinations compared to their individual metal oxide nanoparticle counterparts at the respective K-edges. Further TEM studies with energy dispersive spectroscopy (EDS) have shown that the individual nanoparticles contain both Cu and Ni metals. Therefore, according to both spectroscopic and microscopy data, the most viable explanation for the formation of mixed metal oxide nanoparticles is metals may be present as nanoparticles of their oxides, CuO and NiO, clustered inside larger nanoclusters (i.e as core shell structures). Nanoparticles synthesized with higher concentrations of Ni compared to Cu (i.e. Ni3Cu1 and Ni10Cu1) have shown slightly different radial distribution functions compared to other combinations at the Cu K-edge. We suspected this observation may be due to the alloying of metal species or high noise present in the data for higher Ni concentrated samples at the Cu K-edge. XANES spectra for the mixed metal oxide nanoparticles for all the different combinations showed an edge shift towards higher energy at the Cu K-edge compared to the

cupric oxide standards, while at the Ni K-edge nanoparticle samples showed a spectral shift towards lower energy. This indicates during the formation of mixed metal oxide (or bimetallic) nanoparticles Copper becomes more positive and Nickel becomes more negative in nature inside the nanoclusters.

The final project was carried out by exposing/reacting the dendrimerically prepared nanoparticles with possible dioxin/furan (PCDD/F) precursors to understand the contribution of nanoparticles in the formation of dioxin/furan via surface mediated reactions. Here, we had a few different approaches to execute this set of experiments. First, size selected nanoparticles (nanoparticles prepared at the fully doped condition) were exposed to different precursors such as 1,2 dichlorobenzene, phenol and 2-chlorophenol to study the precursor. The second set of experiments were performed to study the size effect of the nanoparticles in the formation of PCDD/F by selecting 2-chlorophenol as the possible precursor. The third experiment was performed by selecting nanoparticles prepared at fully doped conditions and exposing them to 2-chlorophenol at different temperatures. The reaction of different size nanoparticles with 2-chlorophenol or size selected nanoparticles with different PCDD/F precursors studied at 250 ^{o}C did not show any significant difference in the XANES region of the x-ray absorption spectra compared to unexposed nanoparticle samples. However, during the temperature dependent studies, nanoparticles (prepared at fully doped conditions) exposed to 2-chlorophenol at 375 ^{o}C showed significant differences in the edge region of the XANES spectra compared to their unexposed counterparts.We observed a shift of the absorption edge for CuO nanoparticles toward lower energy suggesting that Cu^{+2} in the nanoparticles have been partially reduced, but not to Cu^{+1},as described in the previously proposed mechanisms. These observations open new

avenues for the contribution of CuO nanoparticles in the formation of PCDD/F via surface mediated reactions as described in chapter six.

7.2 Outlook

In recent years, most of our attention was drawn towards the synthesis of transition metal oxide nanoparticles as laboratory surrogates for combustion-generated particles (i.e. fly ash) and studying their contribution in pollutant formation (PCDD/F). During these studies we have been extensively working with transition metal oxides of Cu, Ni and Fe and investigating how they form nanoparticles on fumed silica support surfaces. However, ZnO is another useful candidate, it is been widely used as an additive in many different products such as plastics, ceramics, glass, cement, lubricants, paints, ointments, adhesives, sealants, pigments, sunscreens, textiles, foods (source of Zn nutrient), batteries, ferrites, fire retardants, and first aid tapes and so on[3-5]. In these industries, ZnO is used as a bulk material or as nanoparticles, and it can be found in the environment in many different forms[4,6].

The properties of ZnO nanoparticles and their increased use have raised concerns about their possible harmful effects on human health and the environment [4,7,8]. Most studies on ZnO nanoparticles and their effects have been reported in aqueous systems, but they can induce significant changes in soil enzyme activities (bio-indicators of soil quality and health) by dissolving in the soil [7]. Also, a few other reported studies on ZnO nanoparticles suggest it can be used as a reusable catalyst or as an active catalyst in organic synthesis[9-11].

Since ZnO is a more active substance than previously studied transition metal oxides, the contribution of ZnO in environmental processes may be fairly significant. Therefore, it is important to study ZnO particle formation on different support surfaces and the contribution of the supported ZnO particles in pollutant formation (via surface mediated reactions).

7.3 References

(1) Lomnicki, S. M.; Wu, H.; Osborne, S. N.; Pruett, J. M.; McCarley, R. L.; Poliakoff, E.; Dellinger, B. *Materials Science and Engineering: B* **2010**, *175*, 136.

(2) Mitran, E.; Dellinger, B.; McCarley, R. L. *Chem Mater* **2010**, *22*, 6555.

(3) Wu, B.; Wang, Y.; Lee, Y.-H.; Horst, A.; Wang, Z.; Chen, D.-R.; Sureshkumar, R.; Tang, Y. J. *Environmental Science & Technology* **2010**, *44*, 1484.

(4) Zheng, X.; Wu, R.; Chen, Y. *Environmental Science & Technology* **2011**, *45*, 2826.

(5) Hernández Battez, A.; González, R.; Viesca, J. L.; Fernández, J. E.; Díaz Fernández, J. M.; Machado, A.; Chou, R.; Riba, J. *Wear* **2008**, *265*, 422.

(6) Gottschalk, F.; Sonderer, T.; Scholz, R. W.; Nowack, B. *Environmental Science & Technology* **2009**, *43*, 9216.

(7) Du, W.; Sun, Y.; Ji, R.; Zhu, J.; Wu, J.; Guo, H. *Journal of Environmental Monitoring* **2011**, *13*, 822.

(8) Huang, Z.; Zheng, X.; Yan, D.; Yin, G.; Liao, X.; Kang, Y.; Yao, Y.; Huang, D.; Hao, B. *Langmuir* **2008**, *24*, 4140.

(9) Dhakshinamoorthy, A.; Visuvamithiran, P.; Tharmaraj, V.; Pitchumani, K. *Catalysis Communications* **2011**, *16*, 15.

(10) Kassaee, M. Z.; Movahedi, F.; Masrouri, H. *ChemInform* **2009**, *40*, no.

(11) Roopan, S.; Nawaz Khan, F. *Chemical Papers* **2010**, *64*, 812.

Vita

Udaya Indike Rodrigo was born in Matara, Sri Lanka. After successfully completing the General Certificate of Education Advanced Level examination (GCE A/L), he was selected to pursue a Bachelor of Science, at the University of Peradeniya, Sri Lanka. He graduated from the University of Peradeniya, in 1999, where he received a Special Degree in Chemistry with Economics, Management and Basic Computing. Then, he completed his Masters of Philosophy Degree (M. Phil.) in Analytical Chemistry at the Post Graduate Institute of Science (PGIS) at the University of Peradeniya in 2004, under the supervision of Professor H.M. Namal Priyantha. Next in 2006, he earned his second master's degree in Chemistry at Bowling Green State University, under the supervision of Professor Michael A. J. Rodgers. During the fall of 2006, he enrolled at Louisiana State University (LSU) to pursue a Doctor of Philosophy degree in Chemistry, under the supervision of Professor Erwin D. Poliakoff.